



National Library  
of Canada

Bibliothèque nationale  
du Canada

Canadian Theses Service

Service des thèses canadiennes

Ottawa, Canada  
K1A 0N4

## NOTICE

The quality of this microform is heavily dependent upon the quality of the original thesis submitted for microfilming. Every effort has been made to ensure the highest quality of reproduction possible.

If pages are missing, contact the university which granted the degree.

Some pages may have indistinct print especially if the original pages were typed with a poor typewriter ribbon or if the university sent us an inferior photocopy.

Reproduction in full or in part of this microform is governed by the Canadian Copyright Act, R.S.C. 1970, c. C-30, and subsequent amendments.

## AVIS

La qualité de cette microforme dépend grandement de la qualité de la thèse soumise au microfilmage. Nous avons tout fait pour assurer une qualité supérieure de reproduction.

S'il manque des pages, veuillez communiquer avec l'université qui a conféré le grade.

La qualité d'impression de certaines pages peut laisser à désirer, surtout si les pages originales ont été dactylographiées à l'aide d'un ruban usé ou si l'université nous a fait parvenir une photocopie de qualité inférieure.

La reproduction, même partielle, de cette microforme est soumise à la Loi canadienne sur le droit d'auteur, SRC 1970, c. C-30, et ses amendements subséquents.

THE UNIVERSITY OF ALBERTA

SEISMIC REFLECTION IMAGING OVER A THERMALLY ENHANCED OIL  
RECOVERY SITE

by

CONSTANTINE TSINGAS

A THESIS

SUBMITTED TO THE FACULTY OF GRADUATE STUDIES AND RESEARCH  
IN PARTIAL FULFILLMENT OF THE REQUIREMENTS FOR THE DEGREE  
OF DOCTOR OF PHILOSOPHY

IN

GEOPHYSICS

DEPARTMENT OF PHYSICS

EDMONTON, ALBERTA

Spring 1990



National Library  
of Canada

Bibliothèque nationale  
du Canada

Canadian Theses Service

Service des thèses canadiennes

Ottawa, Canada  
K1A 0N4

## NOTICE

The quality of this microform is heavily dependent upon the quality of the original thesis submitted for microfilming. Every effort has been made to ensure the highest quality of reproduction possible.

If pages are missing, contact the university which granted the degree.

Some pages may have indistinct print especially if the original pages were typed with a poor typewriter ribbon or if the university sent us an inferior photocopy.

Reproduction in full or in part of this microform is governed by the Canadian Copyright Act, R.S.C. 1970, c. C-30, and subsequent amendments.

## AVIS

La qualité de cette microforme dépend grandement de la qualité de la thèse soumise au microfilmage. Nous avons tout fait pour assurer une qualité supérieure de reproduction.

S'il manque des pages, veuillez communiquer avec l'université qui a conféré le grade.

La qualité d'impression de certaines pages peut laisser à désirer, surtout si les pages originales ont été dactylographiées à l'aide d'un ruban usé ou si l'université nous a fait parvenir une photocopie de qualité inférieure.

La reproduction, même partielle, de cette microforme est soumise à la Loi canadienne sur le droit d'auteur, SRC 1970, c. C-30, et ses amendements subséquents.

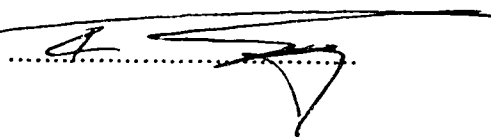
ISBN 0-315-60387-9

THE UNIVERSITY OF ALBERTA  
**RELEASE FORM**

NAME OF AUTHOR     Constantine Tsingas  
TITLE OF THESIS     Seismic Reflection Imaging over a Thermally Enhanced  
                             Oil Recovery Site.

DEGREE FOR WHICH THESIS WAS PRESENTED     Doctor of Philosophy  
YEAR THIS DEGREE GRANTED                         Spring 1990

Permission is hereby granted to THE UNIVERSITY OF ALBERTA LIBRARY to reproduce single copies of this thesis and to lend or sell such copies for private, scholarly or scientific research purposes only. The author reserves other publication rights, and neither the thesis nor extensive extracts from it may be printed or otherwise reproduced without the author's written permission.

(SIGNED) 

PERMANENT ADDRESS:

10 Ippokrinis str,  
Zographou, Athens,  
GREECE. 15773

DATED *20/12/*, 1989

THE UNIVERSITY OF ALBERTA  
FACULTY OF GRADUATE STUDIES AND RESEARCH

The undersigned certify that they have read, and recommend to the Faculty of Graduate Studies and Research, for acceptance, a thesis entitled SEISMIC REFLECTION IMAGING OVER A THERMALLY ENHANCED OIL RECOVERY SITE submitted by CONSTANTINE TSINGAS in partial fulfillment of the requirements for the degree of DOCTOR OF PHILOSOPHY in GEOPHYSICS.

*E. R. Kant*

Supervisor

*St. H. ...*

*Ph. ...*

*M. E. ...*

*A. J. ...*

*W. ...*

External Examiner

Date *Dec 15 / 89*

*Dedicated*

To the fond memory of my father Christos Tsingas.

## Abstract

In recent years it has become increasingly important to develop a capability for monitoring Enhanced Oil Recovery (EOR) processes as they are occurring within the reservoir. A knowledge of the developing processes in real time allows the possibility of controlling and/or modifying the processes involved. During thermal EOR operations, such as steam stimulation or steamflooding, the reservoir formations undergo a number of thermally and mechanically induced physical alterations. These changes cause various petrophysical parameters to produce amplitude anomalies on seismic reflected energy. The amplitude anomalies occur as bright spots, zones of attenuated energy and as interference phenomena. They may be due to large changes in reflection coefficients due to the presence of gas or hot steam and/or steam condensate.

The elastic equations may need to be modified due to enhanced anisotropy and the change in velocity which creates "lenses" which focus or defocus acoustic or elastic waves and produce interference phenomena on stacked sections.

Synthetic seismograms were computed for P-SV and SH wave propagation in transversely isotropic media adapted for the vector CDC - 205 supercomputer. The algorithms are based on the fourth order accurate MacCormack type splitting scheme. Examples indicate that anisotropy plays an important role in modeling the kinematic and the dynamic properties of the wave propagation and should be taken into account when necessary.

A new type of migration before stack has been developed which is relatively cost effective and successful in imaging diffracted elastic waves. It is a simple and yet robust seismic common shot gather depth migration operating in the frequency - space ( $\omega$ - $x$ ) domain. This permits one to carry out migration before stacking and yields an image in depth which has higher resolution than a normal Common Midpoint (CMP) section before

or after migration. Another advantage of this migration algorithm is that it can incorporate the thin lens term allowing us to image steam zones which occur as thin lenses during thermal EOR processes. The extrapolation step is performed employing the 45° parabolic approximation to the scalar wave equation. The common shot gather migration has a requirement the computation of the arrival time of the direct wave from the source to all depth points. This is accomplished by a fourth order Runge Kutta integration method of the eikonal equation. This method is suitable for areas with both lateral and vertical velocity variations. Aside from some model examples, a field data set over a heavy oil steam injection site is used to illustrate the procedure and define the lateral extent of the steam invaded zone.

A seismic experiment consisting of three reflection lines was carried out by Esso Resources in February of 1984 over a steam injection research site near Cold Lake, Alberta. Analysis of the field data showed that large variations in reflected scattered energy occurred as a function of angle of incidence in areas affected by the steam zone. An Amplitude - versus - Angle (AVA) analysis, over the steam injection location showed encouraging results and established that seismic reflection methods, when well designed and carefully processed, can be used to map the invaded steam zones in steam stimulation EOR operations. The results are imaged on a new type of display called **ARPA** (Amplitude Ratio for Partial Angle), which illustrates reflections zones with low-high Poisson's ratio or equivalent high/low gas saturation with a CMP stack section plotted as the background.



## ACKNOWLEDGEMENTS

I would like to thank my supervisor, Dr E. R. Kanasewich for invaluable sustained guidance and encouragement throughout this programme.

I wish to express my appreciation to the Alberta Oil Sands Technology and Research Authority, Natural Sciences and Engineering Research Council of Canada for providing the financial support during my Ph.D. studies. In particular I would like to express my sincere appreciation to AOSTRA for awarding me with a two year scholarship. Esso Resources Canada Limited for their permission to have access to the seismic reflection data. The scientific assistance of Dr. S. Bharatha and Dr. H. Cooper from Esso Resources is greatly appreciated.

I would like to thank Mr. C. McCloughan since on many occasions his experience with computer software matters was of benefit to me. I also want to thank my colleagues Dr Suhas Phadke and Dr Antonio Vafidis for exchanging ideas.

I am grateful to my wife Salli Yule-Tsingas for her support and encouragement and to my parents who made it all possible.

## TABLE OF CONTENTS

CHAPTER	PAGE
<b>1. INTRODUCTION</b>	<b>1</b>
1.1 Introduction	1
1.2 Monitoring Enhanced Oil Recovery processes	2
1.3 Outline of the Thesis	4
<b>2. GEOLOGICAL SETTING</b>	<b>5</b>
2.1 Introduction	5
2.2 Geology of the Cold Lake area	7
2.3 Origin and structure of the oil sands	9
2.4 Reservoir Description	10
2.5 Steam stimulation recovery of the Cold Lake bitumen	11
<b>3. ELASTIC WAVE PROPAGATION IN TRANSVERSELY ISOTROPIC MEDIA</b>	<b>13</b>
3.1 Introduction	13
3.2 Synthetic seismograms in anisotropic media	14
3.3 P-SV wave propagation in transversely isotropic media	16
3.4 SH wave propagation in transversely isotropic media	20
3.5 The MacCormack type scheme for the solution of the hyperbolic system of equations	22
3.6 Numerical examples	26
3.7 Conclusions	35
<b>4. SHOT GATHER MIGRATION IN <math>\omega</math>-x DOMAIN</b>	<b>36</b>
4.1 Introduction	36
4.2 Migration techniques	36

4.3 Extrapolation and Imaging	38
4.4 Single shot depth migration	40
4.5 Theory of the $\omega$ -x migration	42
4.6 The $\omega$ -x migration and stacking algorithm	48
4.7 Comparison of the dispersion relations between the wave equation and the parabolic wave equation	50
4.8 Computation of the direct travel time arrivals	51
4.9 Muting of the migrated shot gathers	56
4.10 Examples	57
4.11 Conclusions	64
<b>5 . ANALYSIS OF SEISMIC REFLECTION DATA OVER A STEAM INJECTION SITE</b>	66
5.1 Introduction	66
5.2 Processing of the seismic reflection lines	67
5.3 Zero offset modeling with the Exploding Reflector Model (ERM) including attenuation	80
5.4 Results incorporating a constant Q	81
5.5 Pre-stack omega-x depth migration	84
5.6 Conclusions	94
<b>6. AMPLITUDE VERSUS ANGLE ANALYSIS FOR EOR PROCESSES</b>	95
6.1 Introduction	95
6.2 A review on attenuation and velocity dispersion in fluid saturated rocks	96
6.3 Petrophysical changes during EOR processes	100
6.4 Amplitude versus angle variation due to	

steam injection	105
6.5 Formulation of the Amplitude versus angle analysis	108
6.6 Imaging Amplitude versus angle seismic reflection data	111
6.7 Conclusions	123
<b>7. CONCLUSIONS</b>	124
<b>BIBLIOGRAPHY</b>	128
<b>APPENDIX A</b>	139
<b>APPENDIX B</b>	146
<b>APPENDIX C</b>	156
<b>APPENDIX D</b>	160
<b>APPENDIX E</b>	161

## List of Tables

Table	Page
6.1 Compressional and shear wave velocities, bulk densities, and Poisson's ratios for various $S_w$ , $S_{st}$ , $S_{bit}$	106

## List of Figures

Figure	Page
2.1 Heavy oil deposits of western Canadian basin	6
2.2 Generalized geological crossection showing the Upper Mannville group (UM) and the Lower Mannville group (LM)in the Cold Lake are. The data are obtained from well logs that are in the public domain. (Location of line AA' is shown in Figure 2.1)	8
3.1 Schematic representation of the MacCormack type splitting finite difference algorithm.	25
3.2 (a) Isotropic shale- isotropic sandstone interface employed for the P-P reflection coefficients calculation. (b) Transversely isotropic shale and isotropic sandstone.	27
3.3 (a) Geometry used for the generation of the P-SV synthetic seismograms shown in Figure 3.3b and 3.3c. (b) Vertical component of the particle velocity for the isotropic shale- isotropic sandstone interface. (c) Same as Figure 3.3b but with anisotropic shale.	29
3.4 (a) Comparison between exact and numerical (predicted by the F.D. algorithm) for the P-P reflection coefficients for the isotropic case. (b) Same as Fig. 3.4a but with anisotropic shale. (c) P-SV converted analytical reflection coefficients for the models shown in Fig. 3.4b and 3.4c, respectively.	30
3.5 Shallow Cold Lake, Alberta, depth model employed for the generation of the P-SV and SH synthetic seismograms including a steam zone. An arbitrary shape of the steam zone was chosen to	

	indicate the flexibility of the F.D. algorithm.	32
3.6	(a) SH synthetic seismograms for the isotropic case	
	(b) SH synthetic seismograms for the elliptical anisotropic case	33
3.7	(a) P-SV synthetic seismograms for the vertical component of particle velocity. (b) Same as Figure 3.7a except that now interfaces #3 and #4 and #4 and #5 exhibiting a transverse isotropy of 15% and 20% higher in the horizontal direction.	34
4.1.	Flow - chart for the $\omega$ - x shot gather depth migration.	49
4.2.	Comparison of the dispersion relations of the exact scalar wave equation to the differential parabolic approximation.	52
4.3.	Comparison of the dispersion relations between the exact scalar wave equation to the finite difference approximation of the parabolic equation.	53
4.4.	Same as Fig. 4.3, but in terms of wave propagation angle.	54
4.5	(a) Time impulse located at 100 ms. (b) Impulse response of the shot gather $\omega$ - x depth migration algorithm.	58
4.6	Syncline depth model. (S=source location, G= receiver location)	59
4.7	SH synthetic split spread shot gather for the syncline model.	60
4.8	Depth migrated shot gather of the syncline model.	61
4.9	Multilayer depth model with a thin lens. Also the unperturbed ray paths are shown.	62
4.10	P-SV (vertical particle velocity) synthetic split spread shot gather due to the multilayer model shown in Fig. 4.9.	63
4.11	Migrated shot gather of the synthetic section shown in Figure 4.10.	65
5.1	Acquisition geometry of Esso's 1984 seismic experiment at	

	Cold Lake. (The locations of the steam injection and the Horizontal well are also shown).	68
5.2	Schematic representation of a Common Midpoint (CMP) gather	69
5.3	Esso's common midpoint stack section for line 80. (Arrow indicates the steam injection level)	70
5.4	Esso's common midpoint stack section for line 81. (Arrow indicates the steam injection level)	71
5.5	Esso's common midpoint stack section for line 82. (Arrow indicates the steam injection level)	72
5.6	Amplitude decay function calculated for different traces within various shot gathers.	74
5.7	Common Midpoint stack section for line 80. (Relative amplitude processed, arrow indicates the steam injection level)	76
5.8	Common Midpoint stack section for line 81. (Relative amplitude processed, arrow indicates the steam injection level)	77
5.9	Common Midpoint stack section for line 82. (Relative amplitude processed, arrow indicates the steam injection level)	78
5.10	Power spectrum for CMP #1032, line 82.	79
5.11	Depth model used for the zero offset modeling ( $Q = 8$ in the steam $Q = 30$ in the background)	85
5.12	Zero offset synthetic section employing the depth model shown in Fig. 5.11 ( $Q = 8$ in the steam $Q = 30$ in the background)	86
5.13	Common midpoint stack section for line 82 (same as Fig. 5.9 but with different horizontal and vertical scales)	87
5.14	Shot gather # 1025 for line 82. (First break muting, surface statics, geometrical spreading and trace balancing have been applied)	89



5.15	Velocity - depth model employed during the post - stack and pre - stack migrations.	90
5.16	After stack depth migrated section for line 82 (arrow indicates the steam injection level).	91
5.17	Migrated shot gather #1025 of line 82 after spatial muting	92
5.18	Migrated $\omega$ - x stacked ( <b>MOXS</b> ) section for line 82 employing the pre - stack $\omega$ - x migration algorithm described in the text. (arrow indicates the steam injection level).	93
6.1	(a) P - P reflection coefficients for the shale - porous oil sand interface. (see text for details). (b) Normalized P - P reflection coefficients shown in Figure 6.1(a).	107
6.2	Time - offset windows computed for different angles of incidence namely, $5^0$ - $10^0$ , $10^0$ - $15^0$ , $15^0$ - $20^0$ .	110
6.3	(a) Angle stack for the range of $5^0$ - $10^0$ , for line 82. (b) Angle stack for the range of $10^0$ - $15^0$ , for line 82. (c) Angle stack for the range of $15^0$ - $20^0$ , for line 82. (arrow indicates the steam injection level)	112
6.4	(a) Sum of reflected amplitudes for the (425 - 475) ms time window, for line 82. (b) Sum of reflected amplitudes for the (475 - 525) ms time window. (The steam injection level is indicated) (c) Sum of reflected amplitudes for the (525 - 575) ms time window.	113
6.5	Amplitude Ratio for Partial Angles ( <b>ARPA</b> ) plot for line 80 with Esso's processed CMP stack section shown as the background (Locations C and D, indicate potential gas saturated regions). (arrow indicates the steam injection level)	115
6.6	Amplitude Ratio for Partial Angles ( <b>ARPA</b> ) plot for line 81 with	

	Esso's processed CMP stack section shown as the background (Location B indicates a potential gas saturated region) (arrow indicates the steam injection level).	116
6.7	Amplitude Ratio for Partial Angles ( <b>ARPA</b> ) plot for line 82 with Esso's processed CMP stack section shown as the background (Location A indicates a potential gas saturated region). (arrow indicates the steam injection level)	117
6.8	Amplitude Ratio for Partial Angles ( <b>ARPA</b> ) plot for line 80 with relative amplitude processed CMP stack section shown as the background (Locations C and D, indicate potential gas saturated regions, arrow indicates the steam injection level).	118
6.9	Amplitude Ratio for Partial Angles ( <b>ARPA</b> ) plot for line 81 with relative amplitude processed CMP stack section shown as the background (Location B indicates a potential gas saturated region). (arrow indicates the steam injection level)	119
6.10	Amplitude Ratio for Partial Angles ( <b>ARPA</b> ) plot for line 82 with relative amplitude processed CMP stack section shown as the background (Location A indicates a potential gas saturated region). (arrow indicates the steam injection level)	120
6.11	Plan view of the area under investigation illustrating the lateral boundaries of the steam invaded zone (Part of the seismic lines and the surface location of steam injection well are also shown).	122
E.1	Steam zone growth for three and five years of steam injection periods	164

# CHAPTER 1

## INTRODUCTION

### 1.1 Introduction

This thesis explores methods by which one may interpret seismic reflection data for the anisotropic properties of the layers and seeks to find new ways of displaying the elastic wave information to image small heterogeneous zones with high resolution, and to display Poisson's ratio as an interpretative tool in obtaining fluid content.

Steam injection into heavy oil and tar sands formations has recently become an integral part of thermal oil recovery operations (Farouq Ali, 1982). Remarkable recovery problems can be encountered in these tar sands accumulations as the oil in place has very high viscosity and is practically immobile within the geologic formations of occurrence. Fortunately, the viscosity of oil sands dramatically decreases by 4 orders in magnitude at temperatures of 220<sup>0</sup> C as compared to 12<sup>0</sup> C which are encountered under normal reservoir conditions, and one can resort to thermal oil recovery techniques.

The capability for monitoring enhanced oil recovery (EOR) processes *in situ* has become increasingly important. A knowledge of the developing processes in real time allows the possibility of controlling and/or modifying the processes involved. In particular, one would like to determine the size, position and details on the shape or preferred direction of growth of the steam zone. Information about the distribution of fluids inside the zone is also highly desirable. Diagnosis of the above features could lead to improved heavy oil extraction techniques and more efficient field operations.

Seismic methods involving the transmission, reflection, refraction or diffraction of elastic waves in 3D reflection methods, vertical seismic profiling (VSP) and hole to hole logging appear to be promising as remote sensing methods with nearly the appropriate

apparent wavelength for effective resolution of the features.

## **1.2 Monitoring Enhanced oil Recovery processes**

A number of seismic and non seismic techniques which allow mapping of Enhanced Oil Recovery (EOR) processes are described extensively by Wayland and Leighton (1985). Non seismic techniques available involve the use of electromagnetic waves, pressure tests and tracer injections. Wayland and Lee (1986), presented a review on some existing seismic techniques that might be useful for mapping EOR processes. Recently, several publications have appeared regarding the seismic sounding techniques such as conventional 2-D seismic reflection methods (Britton et al, 1983), 3-D seismic surveys, (Greaves and Fulp, 1987; Pullin et al, 1987), borehole seismic tomography (Macrides 1987; Macrides and Kanasewich, 1987, Macrides et al, 1988, Justice et al 1989) and microseismicity (Nyland and Dusseault, 1983) which have shown promising results in monitoring EOR processes.

During these operations the reservoir formations undergo induced petrophysical alterations. Such alterations can affect the reservoir conditions substantially, i.e., can cause preferred crack orientation, consequently, transverse or azimuthal anisotropy. New finite difference algorithms were developed in this dissertation to model P-SV and SH seismic wave propagation in transversely isotropic inhomogeneous media.

The amplitude distortion during Common Midpoint (CMP) stacking is removed with better resolution of small anomalies by a new prestack depth migration operation proposed here. According to this technique, acoustic wave amplitudes are mapped to the true subsurface location and consequently they produce a more reliable zero offset depth

section compare to the sections obtained with an after stack depth migration. Each individual field shot record is migrated followed by a common receiver stack operation. The stacking of the wavefield at the reflecting zones for the migrated energy is carried out to improve the signal to noise ratio.

The steam injected into the reservoir displaces the heavy oil from the pores of the medium and consequently causes an increase in compressibility of the formation, hence the compressional seismic velocity is decreased. Since only volumetric changes occur, shear seismic wave velocities do not change as much. Laboratory experiments have also shown that a decrease in acoustic velocity as large as 30% can be caused by heating a sample saturated with heavy oil to 120<sup>0</sup> C under reservoir conditions (Wang and Nur, 1988). Since these effects are anticipated to occur also *in-situ*, we can use remote seismic methods to continuously monitor reservoirs throughout the thermally enhanced oil recovery process. One can then map the flooded zones in steam stimulation enhanced oil recovery operations. This velocity decrease and the variable fluid saturation imply that both a time delay and an amplitude brightening of seismic reflections from subsurface zones invaded by the steam zone ought to be observable on seismic sections.

A seismic reflection experiment consisting of three lines over a steam injection site near Cold Lake, Alberta, was carried out by Esso Resources during the month of February 1984. The field records of these lines were available to us for subsequent processing. The data underwent careful processing such as correcting for near surface distortions caused by glacial drift and an effective scheme for preserving the original seismic reflection amplitudes. An amplitude versus angle analysis revealed zones with high or low Poisson's ratio and from these graphs a new method of imaging was developed to display the lateral extent of the heated zone caused by the steam injection operation.

### 1.3 Outline of the Thesis

The thesis consists of seven chapters and five appendices.

Chapter 1 contains a short review of the contents of this thesis.

In Chapter 2 a summary of the origin, formation, geological setting and reservoir description of the Cold Lake oil sands is given. A short note on steam injection as a thermally Enhanced Oil Recovery process is outlined.

Chapter 3 describes the formulation of the P-SV and SH seismic wave propagation in transversely isotropic inhomogeneous media. A new algorithm for the Cyber 205 supercomputer was developed to obtain line source synthetic seismograms. Some examples are also illustrated for various models.

Chapter 4 outlines a new shot gather depth migration algorithm which can be employed to image seismic reflection data. Synthetic examples are considered.

In Chapter 5, the field seismic experiment carried out by Esso Research is outlined. A synthetic zero offset section employing various Q values is computed and compared with a real Common Midpoint Stack (CMP) section. A pre-stack versus an after-stack migration is compared.

In Chapter 6 a discussion of the petrophysical properties which are disturbed by EOR processes is given. Also, seismic attenuation mechanisms and velocity dispersion are reviewed. Finally, an amplitude versus angle analysis (AVA) for EOR operations is also presented. The AVA results are illustrated in a new imaging method called Amplitude-Ratio for Partial Angle (ARPA) plot, which depicts the reflected amplitude-ratio along the seismic lines with the seismic common midpoint stack sections plotted as the background.

Chapter 7 contains the conclusions, discusses the original contribution in the thesis and makes suggestions for future work.

## CHAPTER 2

### GEOLOGICAL SETTING

#### 2.1 Introduction

Immense volumes of viscous heavy oil (about 900 billion bbl oil or  $143 \times 10^9 \text{ m}^3$ ) are present in reservoir rocks underlying the southern interior plains of Western Canada (ERCB, 1979). Figure 2.1 depicts the major heavy oil accumulation regions of the lower Cretaceous heavy oil deposits that occur in the western Canadian basin. The heavy oil deposits occur along a discontinuous northwest/southeast trend across northeastern Alberta from Peace River in the west to Cold Lake along the Alberta Saskatchewan boundary, in the east (Figure 2.1). Between these are the major deposits at Athabasca, Wabasca and some lesser accumulations. The trend continues into the Lloydminster area of Saskatchewan where conventional and enhanced recovery processes produce a viscous  $16^\circ$  ( $965 \text{ kg/m}^3$ ) to  $24^\circ$  API ( $910 \text{ kg/m}^3$ ) gravity oil.

The Cold Lake deposit is located 300 km northeast of Edmonton and covers over  $6500 \text{ km}^2$ . It is the second largest oil sands deposit in Canada and contains more than  $20 \times 10^9 \text{ m}^3$  (125 billion barrels) of heavy oil in place. This heavy oil or bitumen is a low gravity high viscosity fluid which under reservoir conditions is immobile. The terms *heavy oil* or *bitumen* imply a viscous crude hydrocarbon material not recoverable in its natural state by conventional production methods. The minimum depth to the first oil sand at Cold Lake is 300 m and this dictates that production must be by some *in situ* process. These are very costly and as such must be well planned and designed. Reservoir description plays a key role in the selection of the location for a scheme in the planning of a specific recovery process, and in the analysis and prediction of production performance. *In situ* recovery processes basically consists of increasing the mobility of the oil and

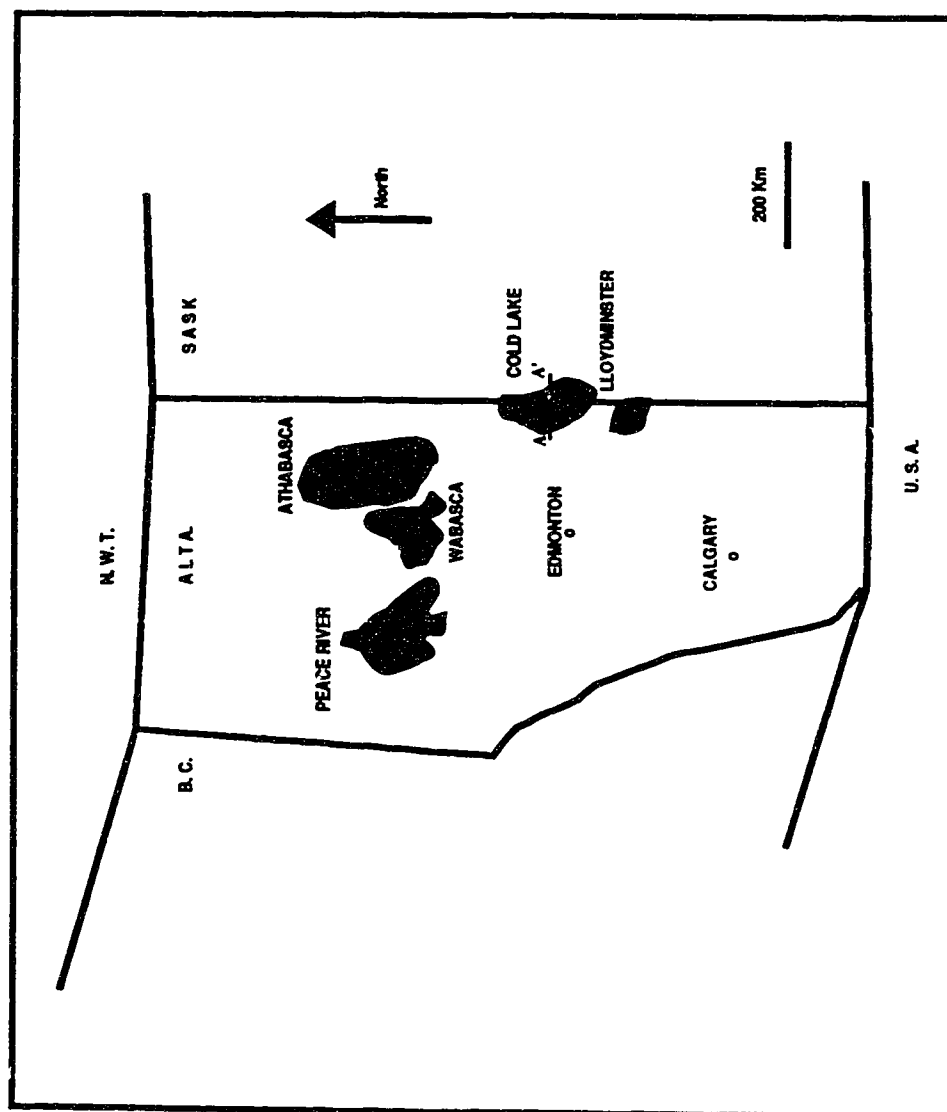


Figure 2.1 Heavy oil deposits of western Canadian basin.



then driving the fluids to a production well.

## **2.2 Geology of the Cold Lake area.**

The heavy oil is contained in various sands of the Upper and Lower Mannville Group of Lower Cretaceous age (Harrison et al, 1979). Lower Mannville sediments are mainly non-marine sands, silstones and shales and grade upward into interbedded marine shales, sands and silstones of the Upper Mannville (Figure 2.2). The heavy oil is commonly associated with gas and water. At Athabasca by far the largest oil reserves occur in Lower Mannville sands of the McMurray Formation. At Cold Lake the Upper Mannville reservoirs contain oil in the Clearwater and Grand Rapids Formations and in their equivalents, including the Wabasca member and Blueskey Formation in the respective Wabasca-Athabasca area and at Peace River. Cold Lake is unique in comparison with the other heavy oil areas in that oil is contained in all four formations of the Mannville group.

At Cold Lake the Mannville group was deposited near the eastern edge of the Western Canadian sedimentary basin on a Paleozoic erosional surface as a nearshore - deltaic to offshore transition sand - shale complex. It is overlain by marine shales of the Colorado Group. These Mannville sands are noncemented and vary considerably in thickness, areal extent and reservoir quality. The Paleozoic unconformity occurs at a depth of around 600m and the top of the Precambrian crystalline basement which is at a depth of 1020m. Both these horizons are prominent seismic reflection markers.

At Cold Lake the Mannville averages 210 m in thickness. The lower Mannville consists of the McMurray Formation up to 60 m thick and characterized by a continuous basal sand section and an upper zone of thinner sand intersected with shales. The basal McMurray sands are mainly water bearing, however the upper thin sands may contain minor amounts of bitumen when adequately structured. The Upper Mannville Group

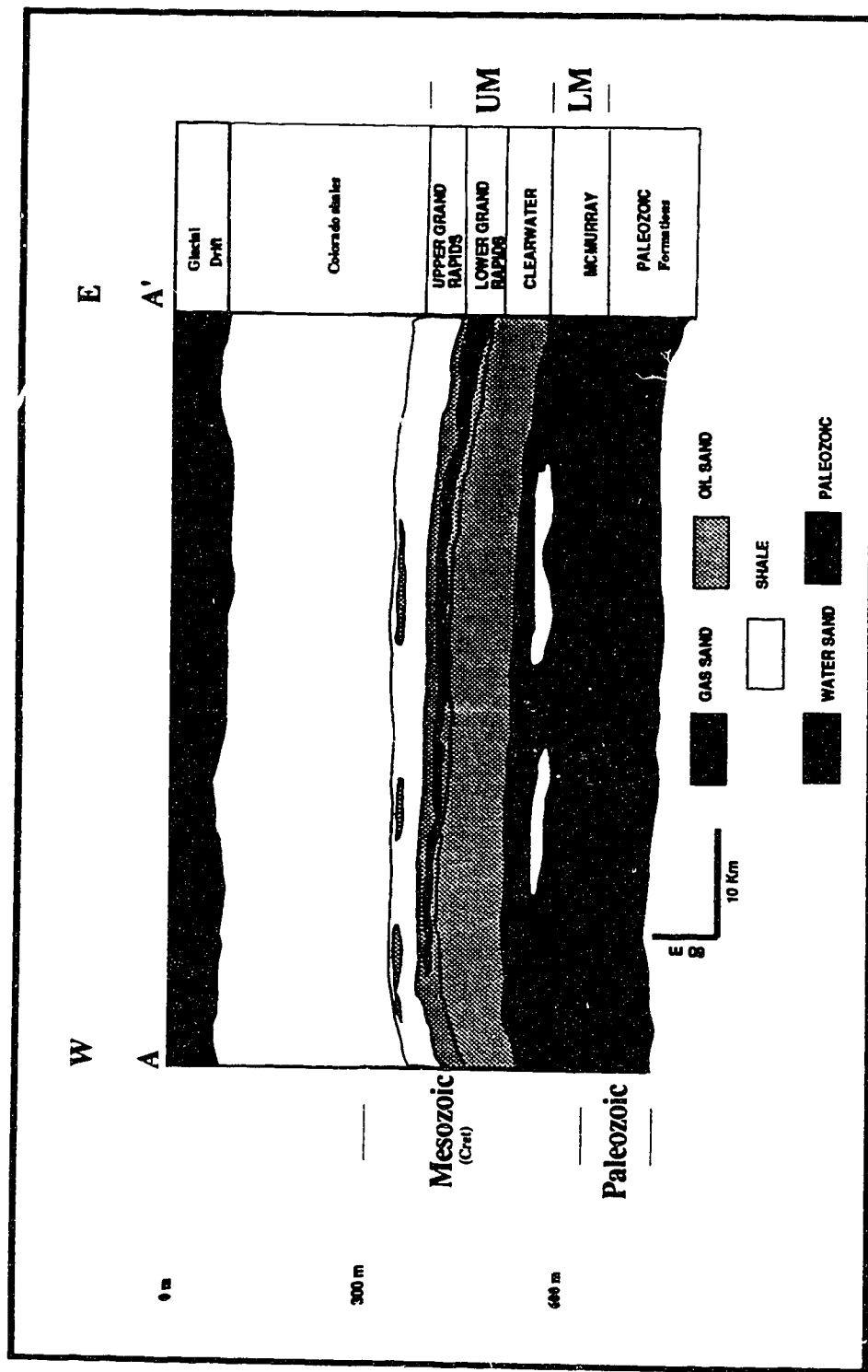


Figure 2.2 Generalized geological cross-section showing the setting of the Upper Mannville Group (UM) and the Lower Mannville Group (LM) in the Cold Lake area. The data are obtained from well logs that are in the public domain. (Location of line AA' is shown in Figure 2.1)

consists of the Clearwater Formation and the Lower and Upper Grand Rapids Formations. The Clearwater, which contains highly saturated sands having an aggregate thickness of about 50m, is the most prolific reservoir. It occurs at depths of 425 - 450 m and accounts for approximately one - half of the total bitumen in place at Cold Lake. When adequately structured the Clearwater can be entirely oil bearing, free of any underlying water. This reservoir has been the target of most pilot and production operations at Cold Lake to date.

The Lower Grand Rapids is up to 50m thick and primarily consists of thin sands interbedded with shales. Oil accumulation is more variable than in the Clearwater and is generally associated with water bearing sands. The Upper Grand Rapids is also 50m thick and primarily consists of thin sands interbedded with shales. Oil accumulation is extremely variable and locally the uppermost sand may contain gas. Depth to these oil sands is usually about 300 m.

### **2.3 Origin and structure of the oil sands**

The origin of the oil sands has long been a subject of speculation among geologists. Bailey et al (1973), suggested that tar accumulations were created by water washing and bacterial degradation of medium gravity crude oils. Water washing removes the more water soluble light hydrocarbons and normal paraffins, resulting in an increase in density and sulfur content which is tied to the more bacteria-resistant heavy and complex cyclic organic compounds.

Oil sands may be considered as a four - phase system: a dense interlocked skeleton of predominantly quartz sand grains, with pore spaces occupied by bitumen, water, gas and minor amounts of clay. Typical Alberta oil sand porosity is 32% with tar saturation 81% and water saturation 19%. The grain density is  $2700 \text{ kg/m}^3$  and the bulk density is  $2100 \text{ kg/m}^3$  (Harris and Sobkowicz, 1977; Dusseault, 1977). The viscosity of the Cold

Lake bitumen is about 100,000 cp, under reservoir conditions ( $12^0$ ). This drops to less than 10 cp at a temperature of  $220^0$  C (Flock and Lee, 1977).

## **2.4 Reservoir description**

The Clearwater is the best reservoir unit at Cold Lake with high oil saturations and thick, relatively homogeneous sections. The entire Clearwater section is oil-bearing and free of underlying water when favorably structured. This unit contains more than 50% of the Cold Lake area bitumen and the areas where no underlying water is present are of current interest. Oil accumulations in the Grand Rapids and McMurray units occur in relatively thin sands and generally are associated with underlying water and occasionally gas. The reservoirs which occur in the Clearwater formation, are the most important reservoirs at Cold Lake (Kendall, 1977). During Clearwater time, there was a very favorable environment for the formation of thick well developed reservoirs. There was a good sand supply with deposition in a deltaic complex of beach and offshore bars. Fluctuations in sea level resulted in thick reservoir sections with repetitious sequences. The sands were clean, well sorted and fine to medium grained. The clean sections of the reservoirs have excellent horizontal continuity. The vertical continuity is occasionally interrupted by discontinuous shale barriers and tight cemented siltstones. These barriers result from clay lamellae that are deposited in cyclic sequences in deltaic deposits (shallow marine) which are common to the Grand Rapids and Clearwater formations (Outtrim and Evans, 1977). Porosities average 30% to 35%, permeabilities are good and oil saturation averages 9% by weight. Fluid distributions are structurally controlled. On high trends, the oil leg can attain a thickness of 45m, with no underlying water. Although there is no underlying water section on the crest of fractures, there may be an aquifer present on the flanks.

In summary, these type of reservoirs are thick, relatively pure sands with good lateral continuity, high oil saturation and in some places underlain by water.

## 2.5 Steam stimulation recovery of the Cold Lake bitumen.

The surface mineable reserves are covered by less than about 40m of overburden and are all located within the Athabasca deposit. The remaining bitumen, which has more than 150m of overburden, must be recovered by *in situ* methods.

The Cold Lake in place reserves are contained in four geological zones ranging in depth from 300 to 500m. Bitumen at Cold Lake has a viscosity of 100,000 cp at a reservoir temperature of 12<sup>0</sup> C. Under these conditions the fluid is immobile and the reservoir impermeable. The principle method of recovery evaluated by Esso Resources is steam stimulation sometimes referred as "Huff and Puff", (Farouq Ali, 1974). According to this method steam is injected into a well at the highest possible rate (in order to minimize heat losses) for several weeks. The injected steam heats the rock and the fluids around the wellbore. Vertical inhomogeneities such as shale barriers, cause only partial vertical sweep while maintaining a radial advance of the fluids in the zone that is contacted. After injecting the desired volume of steam, the well may be shut in for about two weeks. This is called the *soak* period. Finally production takes place from the same wellbore.

Steamflooding or continuous steam injection involves a multiple well pattern consisting of a central steam injector and several corner producers. Steamflooding is recommended when reservoir pressure is low and steam injectivity is high, pointing to high permeability, small formations. The principal advantage of a steamflood is the large areal sweep efficiency which is unattainable in steam stimulation.

At Esso Resources Leming Pilot high temperature steam around 315<sup>0</sup> C, at a pressure 10-11MPa is injected into wells at rates up to 240 m<sup>3</sup>/d for 40 to 90 days. The

wells are then produced back at total fluid rates of approximately 90m<sup>3</sup>/d. Continued cyclic operation in this manner for 9 to 12 cycles is predicted to result in 20% recovery (Shepherd, 1979).

In the present study the steam was injected at a depth of approximately 450m in the Clearwater formation near Cold Lake, Alberta. It is a mature steam zone since steam injection started in 1979, and continued since then with on and off injection periods. The steamflood process substantially increases *in situ* temperature, causes changes in gas - fluid saturation, density, velocity and Poisson's ratio of the porous rock. Zones with altered physical properties were detected by anomalous seismic amplitude responses due to the fact that an increase in gas - fluid saturation in the reservoir formation would produce measurable changes in seismic reflection amplitude.

## **CHAPTER 3**

### **ELASTIC WAVE PROPAGATION IN TRANSVERSELY ISOTROPIC MEDIA.**

#### **3.1 Introduction**

For the last two decades, interest in the propagation of seismic waves in anisotropic media was mostly theoretical. At present, however, the importance of the practical aspects is increasing considerably. Seismic velocity anisotropy is a widespread phenomenon in the Earth's crust. A large variety of mechanisms such as crystal alignments and grain alignments in the Earth's gravitational field, preferential alignment of cracks, stress induced effects, the interweaving of thin sedimentary beds, may give rise to anisotropy. Until recently, seismic data were interpreted by assuming isotropy and anisotropic effects were largely ignored. With the increasing resolution of seismic observations and with the use of multicomponent detectors there is a growing awareness that the assumption of isotropy is often violated. The anisotropy of a medium is often closely connected with complex inhomogeneities in the medium. Thus methods which allow the modeling of seismic wave propagation in complex laterally and vertically varying structures, containing combinations of isotropic and anisotropic layers, are highly desirable. Two finite difference algorithms are presented in this chapter for P-SV and SH wave propagation in transversely isotropic inhomogeneous media. Solving the equivalent first order hyperbolic system of equations, instead of the second order wave equation, one avoids computation of the spatial derivatives of the medium's anisotropic elastic parameters.

### 3.2 Synthetic seismograms in anisotropic media.

There are fundamental differences between wave propagation in isotropic and anisotropic media, (Crampin, 1977, 1981). In most applications of elasticity theory to problems in petroleum geophysics, the medium is assumed to be isotropic. On the other hand most crustal rocks are found experimentally to be anisotropic (Thomsen, 1986; Levin, 1980; Winterstein, 1986). Anisotropy can complicate elastic wave propagation considerably. With the recognition that wave propagation through rock with aligned cracks can be simulated by propagation through homogeneous or inhomogeneous anisotropic rock and that polarization anomalies are very sensitive diagnostics of anisotropy (Pamford and Crampin, 1977, Crampin, 1984, Thomsen, 1988), new horizons open to the study of the *in situ* stress field and new parameters can be evaluated for Earth materials.

In this work we consider only an hexagonal symmetry system where the symmetry axis is normal to the free surface. This is called *transverse isotropy*. In transversely isotropic media only the wavefront of SH waves is always an oblate ellipsoid (Helbig, 1983). An exhaustive study of the consequences of elliptical anisotropy for the concepts and techniques in recent exploration seismics was published by Levin (1978).

Postma (1955) has presented results dealing with travel time methods in anisotropic media. Kinematic properties alone however, are no help if one wants to distinguish between isotropy and anisotropy and one must examine the amplitude data. Hence, dynamic properties must be considered, producing a need for synthetic seismograms. Daley and Hron (1979), presented a method employing ART (Asymptotic Ray Theory) for SH waves in layered transversely isotropic media. Martynov and Mikhailenko (1984), in a method based on a combination of partial separation of variables and finite difference method, computed synthetic seismograms for anisotropic inhomogeneous media for the half space and sphere. White (1982), has computed synthetic seismograms by integrating



over analytical expressions, which are not available for complicated models. Booth and Crampin (1983a, b) have extended the reflectivity technique for calculating synthetic seismograms from point or line sources in plane layered models to include layers with general anisotropy. Petrashen and Kashtan (1984) and Cerveny and Firbas (1984), used ray methods to compute synthetic seismograms for inhomogeneous anisotropic media. Fryer and Frazer (1984) calculated synthetic seismograms for stratified anisotropic media using a slightly modified version of the reflectivity method introduced by Kennett (1983). Hron et al (1986), computed the kinematic and dynamic properties of seismic body waves in elliptical anisotropic media employing the zero order approximation of the Asymptotic Ray Theory (ART). Recently, Gajewski and Psencik (1987), presented a very elegant method based on ART to compute synthetic seismograms in 3-D laterally inhomogeneous anisotropic media.

The advent of the new generation of supercomputers motivated our work towards simulation of wave propagation with higher accuracy in two dimensional transversely isotropic inhomogeneous media (Tsingas, et al, 1989). Most of the programs in existence are written for conventional computers and they do not take advantage of vector computation. It is also very hard to fully vectorize an already existing program without changing the algorithm while the benefits from the automatic vectorization are very limited. We follow the semantic vectorization approach where the numerical parts of the program are written so that they are fully vectorized. The larger virtual memory of supercomputers results in finer grids which minimize quite dramatically the dispersion effects even for the most popular second order schemes.

The very basic equations of motion as well as the stress-strain relations have been implemented instead of the actual wave equation in order to avoid numerical derivatives for the medium's parameters. One of the key factors in forward modeling is the implementation of the source. Since we are working with the two dimensional problem an axial symmetry

is implied and it is more natural to utilize a line source. The method of Alterman and Karal (1968), was also adopted for the source implementation, (Vafidis,1988).

Examples of the P-SV and SH wave propagation in transversely isotropic perfectly elastic inhomogeneous media are illustrated in this chapter. These examples, illustrate the flexibility of the Finite Difference (F.D.) algorithm to compute synthetic seismograms in complex media as well as the complications that anisotropy introduces in the Earth's seismic response.

### **3.3 P - SV wave propagation in transversely isotropic media**

A medium having hexagonal symmetry possesses two dimensional isotropy. A material of this kind, which is called transversely isotropic, has elastic parameters which are the same in two directions but different in the third.

The behavior of seismic wave propagation in isotropic and transversely isotropic media is very similar. In both cases waves such as P-SV and Rayleigh modes decouple from SH and Love wave motions in plane layered structures. The P and SV motions in transversely isotropic media are necessarily mixed if the angle of incidence of the wavefronts to the plane of isotropy is other than 0 or 90 degrees. Therefore pure P or SV waves cannot propagate through a transversely isotropic material, except, at normal or grazing incidence to the axis. SH motions, however, do have an independent existence.

We follow an elementary approach on the derivation of the stress strain relations and equations of motion for seismic elastic waves propagating through a transversely isotropic perfectly elastic medium (Love, 1927; Grant and West, 1965). To simplify matters let us consider that the direction of propagation be such that the wave normal lies parallel to the plane  $y=0$ . Moreover, assuming that the symmetry axis is in the vertical ( $z$ ) direction we may write the following stress-strain relations in a matrix form:

$$\begin{bmatrix} \sigma_{xx} \\ \sigma_{zz} \\ \sigma_{xz} \end{bmatrix} = \begin{bmatrix} \lambda_{\parallel} + 2\mu_{\parallel} & \lambda_{\perp} & 0 \\ \lambda_{\perp} & \lambda_{\perp} + 2\mu_{\perp} & 0 \\ 0 & 0 & 2\nu \end{bmatrix} \begin{bmatrix} e_{xx} \\ e_{zz} \\ e_{xz} \end{bmatrix} \quad (3.1)$$

where  $\sigma$  and  $e$  denote the stress and strain components respectively and the subscripts indicate respective stress-strain orientations.

and where,

$$\lambda_{\parallel}, \mu_{\parallel}, \lambda_{\perp}, \mu_{\perp} \text{ and } \nu$$

are the five Lamé constants and the subscripts  $\perp$  and  $\parallel$  indicate the perpendicular and parallel to the plane of isotropy. In terms of the five independent components of the elastic modulus matrix we have that:

$$C_{11} = \lambda_{\parallel} + 2\mu_{\parallel}, C_{33} = \lambda_{\perp} + 2\mu_{\perp}, C_{13} = \lambda_{\perp}, C_{44} = \mu_{\parallel}, \text{ and } C_{66} = \nu.$$

Using the relations between strain and particle displacement namely:

$$e_{xx} = u_{,x} \quad e_{zz} = w_{,z} \quad \text{and} \quad e_{xz} = 1/2 (w_{,x} + u_{,z})$$

we have:

$$\begin{bmatrix} \sigma_{xx} \\ \sigma_{zz} \\ \sigma_{xz} \end{bmatrix} = \begin{bmatrix} \lambda_{\parallel} + 2\mu_{\parallel} & \lambda_{\perp} & 0 \\ \lambda_{\perp} & \lambda_{\perp} + 2\mu_{\perp} & 0 \\ 0 & 0 & 2\nu \end{bmatrix} \begin{bmatrix} u_{,x} \\ w_{,z} \\ 1/2(w_{,x} + u_{,z}) \end{bmatrix} \quad \text{where } w_{,x} \text{ and } u_{,z} \quad (3.2)$$

denote derivatives with respect to  $x$  and  $z$  directions of the  $u$  and  $w$  which are the particle displacement vector components in the direction of propagation  $x$  and  $z$ , respectively.

If we consider only those motions which are independent of the y direction, following Grant and West (1965), the equations of motion in x and z can be written for the horizontal component:

$$\begin{aligned}\rho u_{,tt} &= \partial_x (\lambda_{\parallel} + 2\mu_{\parallel}) u_{,x} + \partial_z (\nu u_{,z}) + \partial_z (\lambda_{\perp} + \nu) w_{,x} \\ \text{or} \\ \rho u_{,tt} &= \partial_x \sigma_{xx} + \partial_z \sigma_{xz}\end{aligned}\tag{3.3}$$

and for the vertical component:

$$\begin{aligned}\rho w_{,tt} &= \partial_x (\lambda_{\perp} + \nu) u_{,z} + \partial_x (\nu w_{,x}) + \partial_z (\lambda_{\perp} + 2\mu_{\perp}) w_{,z} \\ \text{or} \\ \rho w_{,tt} &= \partial_x \sigma_{xz} + \partial_z \sigma_{zz}\end{aligned}\tag{3.4}$$

Instead of approximating the second order hyperbolic wave equations one can form an equivalent first order system (Virieux, 1984, 1986, Bayliss et al, 1986, Vafidis, 1988) as follows:

1. Substituting the particle displacements u and w in the l.h.s. of equations (3.3, 3.4) with the equivalent particle velocities  $\partial u / \partial t$  and  $\partial w / \partial t$ , and divide by the density ,  
and
2. from the stress strain relations (3.1) take the derivative with respect to time, we get the following first order hyperbolic system of equations which can be written in a matrix form as follows:

$$\partial_t \begin{bmatrix} \dot{u} \\ \dot{w} \\ \sigma_{xx} \\ \sigma_{zz} \\ \sigma_{xz} \end{bmatrix} = \begin{bmatrix} 0 & 0 & 1/\rho & 0 & 0 \\ 0 & 0 & 0 & 0 & 1/\rho \\ \lambda_{\parallel} + 2\mu_{\parallel} & 0 & 0 & 0 & 0 \\ \lambda_{\perp} & 0 & 0 & 0 & 0 \\ 0 & \nu & 0 & 0 & 0 \end{bmatrix} \partial_x \begin{bmatrix} \dot{u} \\ \dot{w} \\ \sigma_{xx} \\ \sigma_{zz} \\ \sigma_{zx} \end{bmatrix} + \begin{bmatrix} 0 & 0 & 0 & 0 & 1/\rho \\ 0 & 0 & 0 & 1/\rho & 0 \\ 0 & \lambda_{\perp} & 0 & 0 & 0 \\ 0 & \lambda_{\perp} + 2\mu_{\perp} & 0 & 0 & 0 \\ \nu & 0 & 0 & 0 & 0 \end{bmatrix} \partial_z \begin{bmatrix} \dot{u} \\ \dot{w} \\ \sigma_{xx} \\ \sigma_{zz} \\ \sigma_{xz} \end{bmatrix}$$

or in a compact form

(3.5)

$$\partial_t \mathbf{U} = \mathbf{A} \partial_x \mathbf{U} + \mathbf{B} \partial_z \mathbf{U}$$

The system of equations (3.5) can also be written in the following form :

$$\begin{bmatrix} \rho & 0 & 0 & 0 & 0 \\ 0 & \rho & 0 & 0 & 0 \\ 0 & 0 & \frac{C}{CD-F^2} & \frac{-F}{CD-F^2} & 0 \\ 0 & 0 & \frac{-F}{CD-F^2} & \frac{D}{CD-F^2} & 0 \\ 0 & 0 & 0 & 0 & 1/\nu \end{bmatrix} \frac{\partial}{\partial t} \begin{bmatrix} \dot{u} \\ \dot{w} \\ \sigma_{xx} \\ \sigma_{zz} \\ \sigma_{xz} \end{bmatrix} =$$

$$\begin{bmatrix} 0 & 0 & 1 & 0 & 0 \\ 0 & 0 & 0 & 0 & 1 \\ 1 & 0 & 0 & 0 & 0 \\ 0 & 0 & 0 & 0 & 0 \\ 0 & 1 & 0 & 0 & 0 \end{bmatrix} \frac{\partial}{\partial x} \begin{bmatrix} \dot{u} \\ \dot{w} \\ \sigma_{xx} \\ \sigma_{zz} \\ \sigma_{xz} \end{bmatrix} + \begin{bmatrix} 0 & 0 & 0 & 0 & 1 \\ 0 & 0 & 0 & 1 & 0 \\ 0 & 0 & 0 & 0 & 0 \\ 0 & 1 & 0 & 0 & 0 \\ 1 & 0 & 0 & 0 & 0 \end{bmatrix} \frac{\partial}{\partial z} \begin{bmatrix} \dot{u} \\ \dot{w} \\ \sigma_{xx} \\ \sigma_{zz} \\ \sigma_{xz} \end{bmatrix}$$

where  $C = \lambda_{\perp} + 2 \mu_{\perp}$ ,  $D = \lambda_{\parallel} + 2 \mu_{\parallel}$  and  $F = \lambda_{\perp\parallel}$ .

or

$$\mathbf{E}_0 \partial_t \mathbf{U} = \mathbf{A}_0 \partial_x \mathbf{U} + \mathbf{B}_0 \partial_z \mathbf{U} \quad (3.5a)$$

where  $\mathbf{E}_0$ ,  $\mathbf{A}_0$  and  $\mathbf{B}_0$  are real and symmetric matrices, and thus the system given by equation (3.5) is a hyperbolic system as was shown for the isotropic case (Vafidis, 1988). The explicit finite difference equations employed to compute the solutions of the first order hyperbolic system given by (3.5) are depicted in Appendix A1.

### 3.4 SH wave propagation in transversely isotropic media

SH wave propagation in transversely isotropic media exhibits a form of anisotropy which is called *elliptical anisotropy*. The basic equation for two dimensional SH-wave propagation in a heterogeneous elliptically anisotropic medium is:

$$\rho v_{,tt} = \partial_x (\mu_{\parallel} v_{,x}) + \partial_z (\nu v_{,z}) \quad (3.6)$$

indicating that there is no coupling between the SH and the P-SV motions. In the equation (3.6)  $v$  is the particle displacement,  $\mu_{\parallel}$  and  $\nu$  are the parallel and vertical shear moduli to the plane of isotropy,  $\rho$  is the density and  $\partial$  denotes partial derivative. Body forces have

been neglected. In the horizontal (x) direction, SH waves will propagate with the velocity  $(\mu_{||}/\rho)$ . In the vertical (z) direction, they will move with a speed  $(v / \rho)$ . If the wave travels obliquely, its velocity will lie between these two values.

Instead of approximating the second order hyperbolic wave equation one can utilize an equivalent first order hyperbolic system (Virieux, 1984, 1986, Bayliss et al, 1986, Valiadis, 1988). This can be derived from the equation of motion

$$\dot{v}_{,t} = \rho^{-1} \left[ \partial_x \sigma_{xy} + \partial_z \sigma_{zy} \right] \quad (3.7)$$

and the stress-strain relations after taking derivatives with respect to time

$$\partial_t \sigma_{xy} = \mu_{||} (\partial_x \dot{v})$$

and

$$\partial_t \sigma_{zy} = v (\partial_z \dot{v}) \quad (3.8)$$

where the dot denotes time derivative and  $\sigma_{xy}(x, z, t)$  and  $\sigma_{zy}(x, z, t)$  are the stress components. In this formulation the computations to approximate the space derivatives of  $\mu_{||}(x,z)$  and  $v(x, z)$  are avoided.

In matrix form we get

$$\partial_t \begin{bmatrix} \dot{v} \\ \sigma_{xy} \\ \sigma_{zy} \end{bmatrix} = \begin{bmatrix} 0 & \rho^{-1} & 0 \\ \mu_{||} & 0 & 0 \\ 0 & 0 & 0 \end{bmatrix} \partial_x \begin{bmatrix} \dot{v} \\ \sigma_{xy} \\ \sigma_{zy} \end{bmatrix} + \begin{bmatrix} 0 & 0 & \rho^{-1} \\ 0 & 0 & 0 \\ v & 0 & 0 \end{bmatrix} \partial_z \begin{bmatrix} \dot{v} \\ \sigma_{xy} \\ \sigma_{zy} \end{bmatrix} \quad (3.9)$$

or again in a similar form like equation (3.5) :

$$\partial_t \mathbf{U} = \mathbf{A} \partial_x \mathbf{U} + \mathbf{B} \partial_z \mathbf{U}$$

(3.10)

The system given by equation (3.10) can be written as follows:

$$\begin{bmatrix} \rho & 0 & 0 \\ 0 & \frac{1}{\mu_{\parallel}} & 0 \\ 0 & 0 & \frac{1}{\nu} \end{bmatrix} \frac{\partial}{\partial t} \begin{bmatrix} \dot{v} \\ \sigma_{xy} \\ \sigma_{zy} \end{bmatrix} =$$

$$\begin{bmatrix} 0 & 1 & 0 \\ 1 & 0 & 0 \\ 0 & 0 & 0 \end{bmatrix} \frac{\partial}{\partial x} \begin{bmatrix} \dot{v} \\ \sigma_{xy} \\ \sigma_{zy} \end{bmatrix} + \begin{bmatrix} 0 & 0 & 1 \\ 0 & 0 & 0 \\ 1 & 0 & 0 \end{bmatrix} \frac{\partial}{\partial z} \begin{bmatrix} \dot{v} \\ \sigma_{xy} \\ \sigma_{zy} \end{bmatrix}$$

or

$$\mathbf{E}_0 \partial_t \mathbf{U} = \mathbf{A}_0 \partial_x \mathbf{U} + \mathbf{B}_0 \partial_z \mathbf{U} \quad (3.10a)$$

where  $\mathbf{E}_0$ ,  $\mathbf{A}_0$  and  $\mathbf{B}_0$  are real and symmetric matrices, and thus the system given by equation (3.9) is a hyperbolic system as was shown for the isotropic case (Vafidis, 1988). Appendix A2, depicts the explicit equations employed to compute the solutions of the equivalent first order hyperbolic system for the SH case given by (3.9).

### 3.5 The MacCormack type scheme for the solution of the hyperbolic system of equations.

A simple analysis for the solution of the first order system of hyperbolic equations, is outlined in this section. The reader can refer to Vafidis (1988) for a complete description of the P-SV and SH implementation for the isotropic case. The method is based on the



concept of dimensional splitting (Strang, 1968).

In this method the two dimensional equations (3.5 or 3.10) are updated for one timestep by first solving the equations in the x direction and then in the z direction. For the next timestep the order of x and z updates is reversed. In order to advance the solution from time level n to time level n+2, we use the formula:

$$U^{n+2} = F_x F_z F_z^\dagger F_x^\dagger U^n \quad (3.12)$$

where  $F_x, F_x^\dagger, F_z, F_z^\dagger$  are one dimensional difference operators.

By reversing the order, the resulting scheme is second order accurate in time.

Some of the advantages of the splitting methods is that stability properties are governed by the one dimensional (1D) scheme since we apply 1D approximations, and splitting schemes have smaller phase error than a wide class of unsplit schemes (Tukel, 1974).

For a simplified example consider a (2,4) version of the MacCormack scheme (Gottlieb and Tukel, 1976) which when applied to the one dimensional system:

$$\partial_t U(x,z,t) = A \partial_x U(x,z,t) \quad (3.13)$$

consists of the predictor:

$$U_{j,m}^{(1)} = U_{j,m}^n - \frac{p}{6} A_{j,m} (7 U_{j,m}^n - 8 U_{j+1,m}^n + U_{j+2,m}^n) \quad (3.14)$$

and the corrector

$$U_{j,m}^{n+1} = \frac{1}{2}(U_{j,m}^{(1)} + U_{j,m}^n) + \frac{p}{12} A_{j,m} (7 U_{j,m}^{(1)} - 8 U_{j-1,m}^{(1)} + U_{j-2,m}^{(1)})$$

(3.15)

where the superscript (1) denotes an intermediate step. The equations (3.14) and (3.15) are used in alternate time steps with:

$$U_{j,m}^{(1)} = U_{j,m}^n + \frac{p}{6} A_{j,m} (7 U_{j,m}^n - 8 U_{j+1,m}^n + U_{j+2,m}^n)$$

(3.16)

and

$$U_{j,m}^{n+1} = \frac{1}{2}(U_{j,m}^{(1)} + U_{j,m}^n) - \frac{p}{12} A_{j,m} (7 U_{j,m}^{(1)} - 8 U_{j-1,m}^{(1)} + U_{j-2,m}^{(1)})$$

(3.17)

where,  $p=\Delta t/\Delta x$ ,  $\Delta t$  is the time step in sec and  $\Delta x$  is the grid size in m. A schematic representation of the above formulation is depicted in Figure 3.1.

The predictor and the corrector equations for the vertical and horizontal particle velocities and the respective stress components for the P-SV and SH cases are depicted in the Appendices A1 and A2, respectively. Thus the splitting technique described by equations (3.14 - 3.17) can be performed in the following steps:

- (1) the vector of particle velocity and stress components is calculated at time step  $n+1/2$  taking into account wave propagation in the x-direction only (similarly for the stress components),
- (2) the same vector is evaluated at time step  $n+1$  taking into account wave propagation in

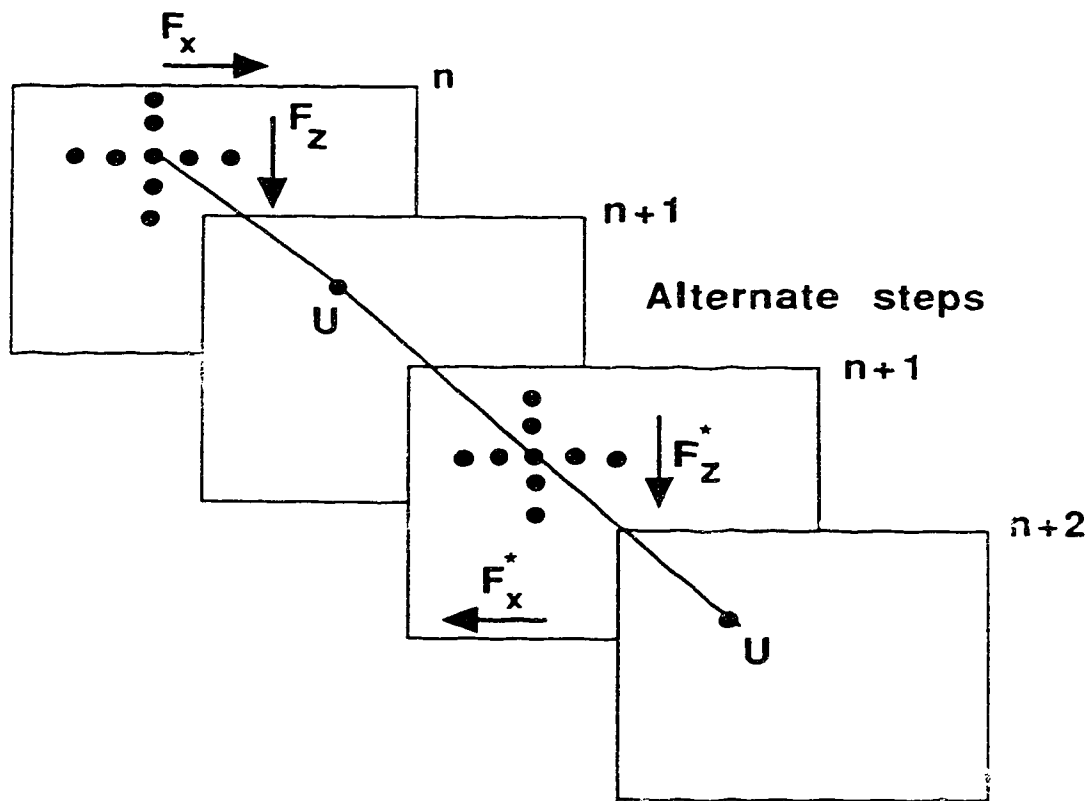


Figure 3.1 Schematic representation of the MacCormack type splitting finite difference algorithm.

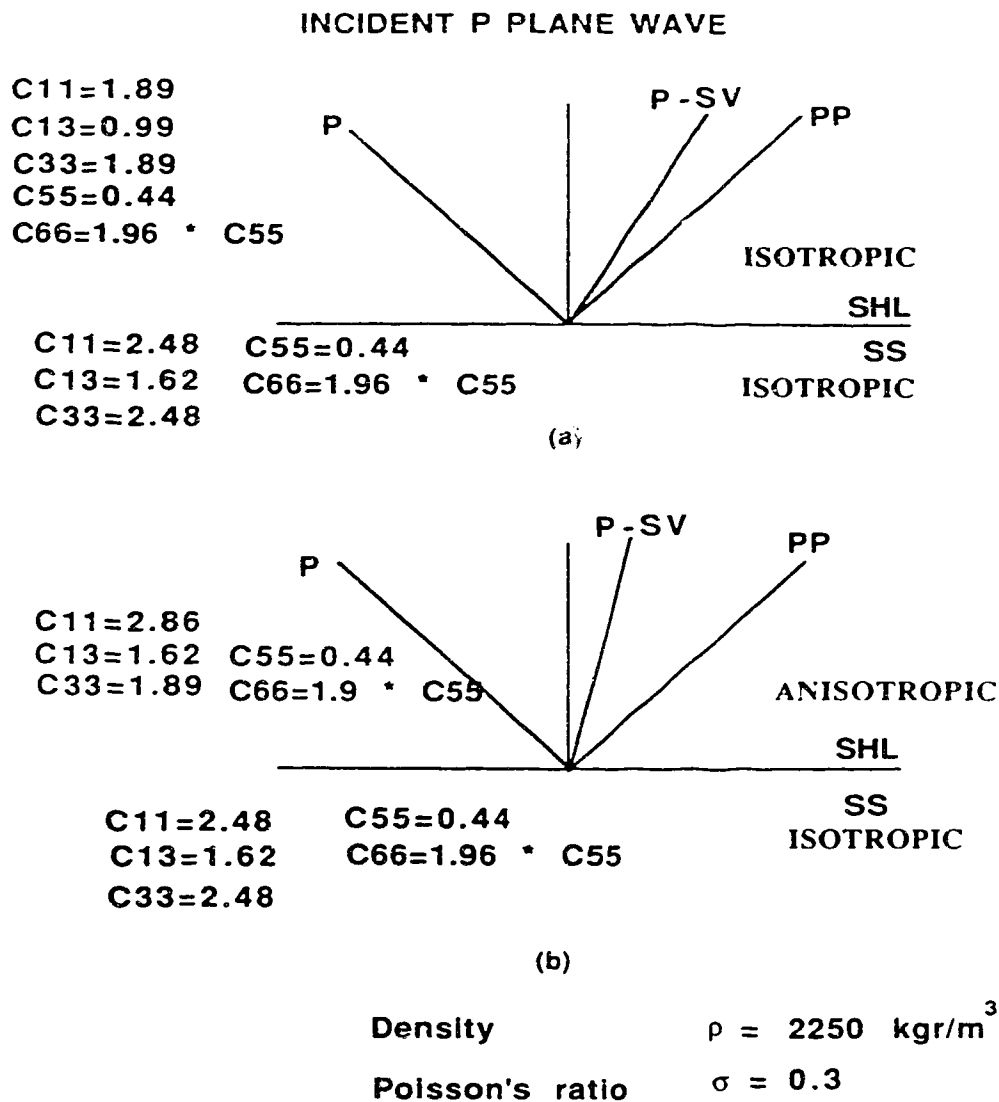
- the z-direction only (similarly for the stress components),
- (3) alternate expressions (see Appendix A) are applied for the particle velocity at time  $n+3/2$  for wave propagation in the z-direction (similarly for the stress components) ;
- (4) the vector of velocity and stress components is calculated at time  $n+2$  from alternate equations to the ones applied in step (1).

This F.D. algorithm is fourth order accurate in space and second order in time while its stability is governed by  $pv_{\max} < 2/3$  where  $v_{\max}$  is the maximum P-wave velocity in m/sec. To avoid grid dispersion we only need  $\Delta x < \lambda_{\min}/6$  where  $\lambda_{\min}$  is the minimum wavelength present in the computed seismograms. Vafidis (1988), analysed the stability, convergence and dispersion effects of the finite difference algorithms in the isotropic case. The criteria are the same for this case since the analysis was based on a local constant phase velocity. As in all finite difference computations, one has to be careful choosing the mesh grid size and the time step for the anisotropic case to reduce dispersion artifacts and solution instabilities.

### 3.6 Numerical examples

P and SH wave line sources were employed for the generation of the P-SV and SH synthetic seismograms, shown in this section respectively. The method of Alterman and Karal (1968), as implemented by Vafidis (1988), was adopted for the source implementation. Since no top, bottom and side boundary conditions have been implemented for this F. D. algorithm special care was taken to avoid artificial reflections by specifying the source location and receiver array accordingly.

Wright (1987), demonstrated the effect of anisotropy on the P-P reflectivity utilizing a shale-sandstone interface. The isotropic model is depicted in Figure 3.2a together with the assigned elastic coefficients. Figure 3.2b, depicts the same interface assuming that



\* All the elastic coefficients must be multiplied by  $10^{10} \text{ N/m}^2$

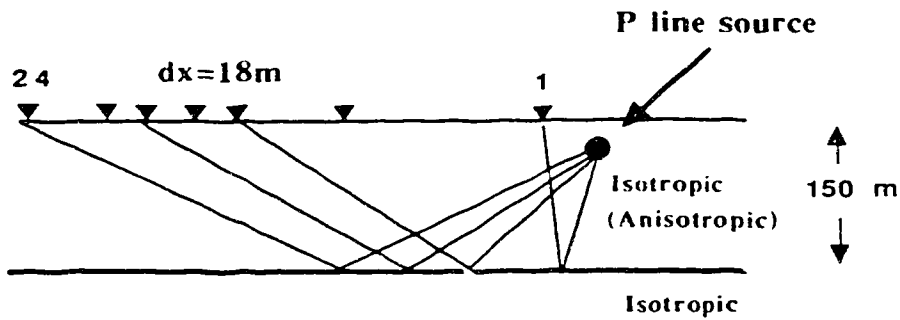
Figure 3.2 (a) Isotropic shale - isotropic sandstone interface employed for the P-P reflection coefficients calculation.

(b) Transversely isotropic shale and isotropic sandstone.

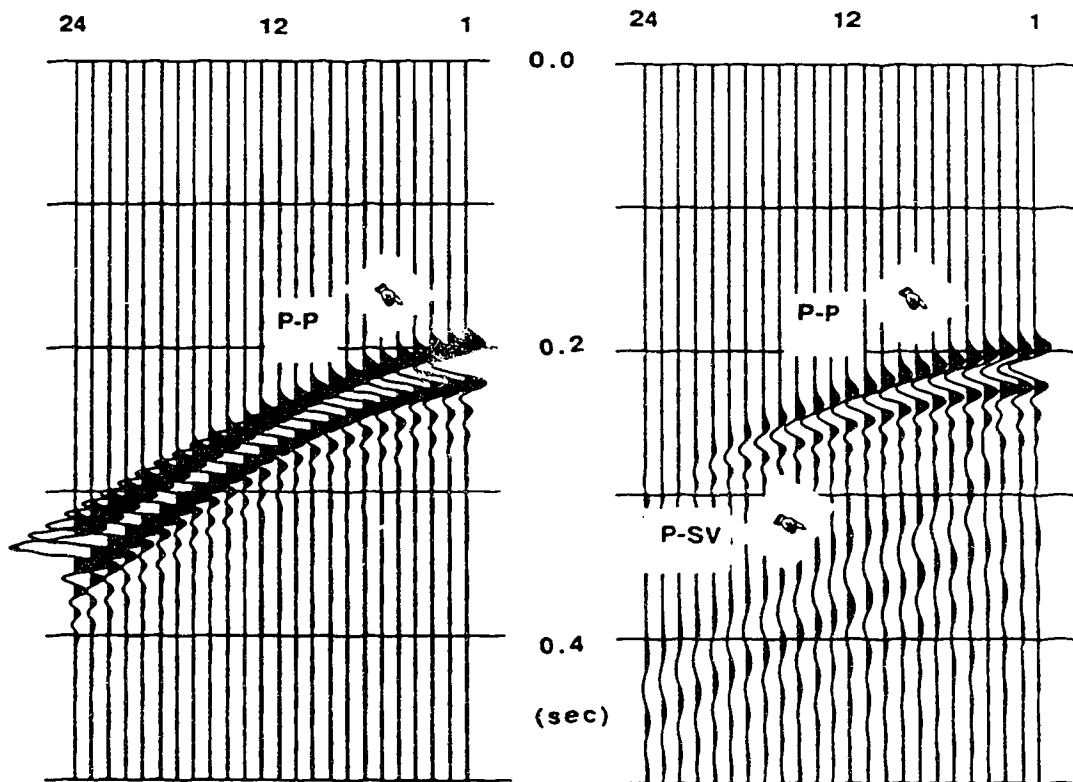
the shale is anisotropic according to the elastic coefficients shown.

Figure 3.3a, illustrates the geometry employed to generate P-SV synthetic seismograms shown in Figure 3.3b and Figure 3.3c, from which the P-P reflection coefficients were derived for the two cases. The P wave line source employed (Figure 3.3a), having a dominant frequency of 30Hz. The grid size was 6m and the time step 0.5ms. Figure 3.3b, simulates an off-end shot gather employing the isotropic shale - sand interface depicted in Figure 3.3a, consisting of 24 traces with a trace spacing of 18m and with the near offset at 18m. Only the vertical component of the particle velocity is shown. Figure 3.3c, depicts the vertical component of the the particle velocity for the same source receiver configuration and assuming an anisotropic shale - sand interface according to the elastic coefficients shown in Figure 3.2b.

As was demonstrated by Wright (1987), the reflected P-P amplitude increases with offset for the isotropic case, whereas for the anisotropic case the reflected P-P amplitude decreases. The F. D. algorithm predicts reflection amplitudes within acceptable errors in comparison with known analytical solutions for transversely isotropic media. Figure 3.4a, shows the exact solutions for the P-P reflection coefficient computed by employing the Daley and Hron (1977) analytical formulas together with the reflection coefficients predicted by the F.D. algorithm for the isotropic case. Figure 3.4b, illustrates the comparison between the analytical and predicted from the F.D algorithm for the anisotropic case. In both Figures 3.4a and 3.4b, the agreement between the predicted by the F.D algorithm and the analytically calculated P-P reflection coefficients is very good. Another effect due to the anisotropy introduced in the upper layer, is the different moveout observed on the reflected signal between the two shot gathers. Observing Figure 3.3c, strong P-SV conversions are present. Figure 3.4c, illustrates the exact P-SV reflection coefficients (Daley and Hron, 1977), for isotropic and anisotropic cases for various angles of incidence. For the anisotropic case the P-SV converted reflection amplitudes are much



(a)



(b)

(c)

Figure 3.3 (a) Geometry used for the generation of the P-SV synthetic seismograms shown in Figure 3.3a and 3.3b.

(b) Vertical component of the particle velocity for the isotropic shale-isotropic sandstone interface.

(c) Same as Figure 3.3b but with anisotropic shale.

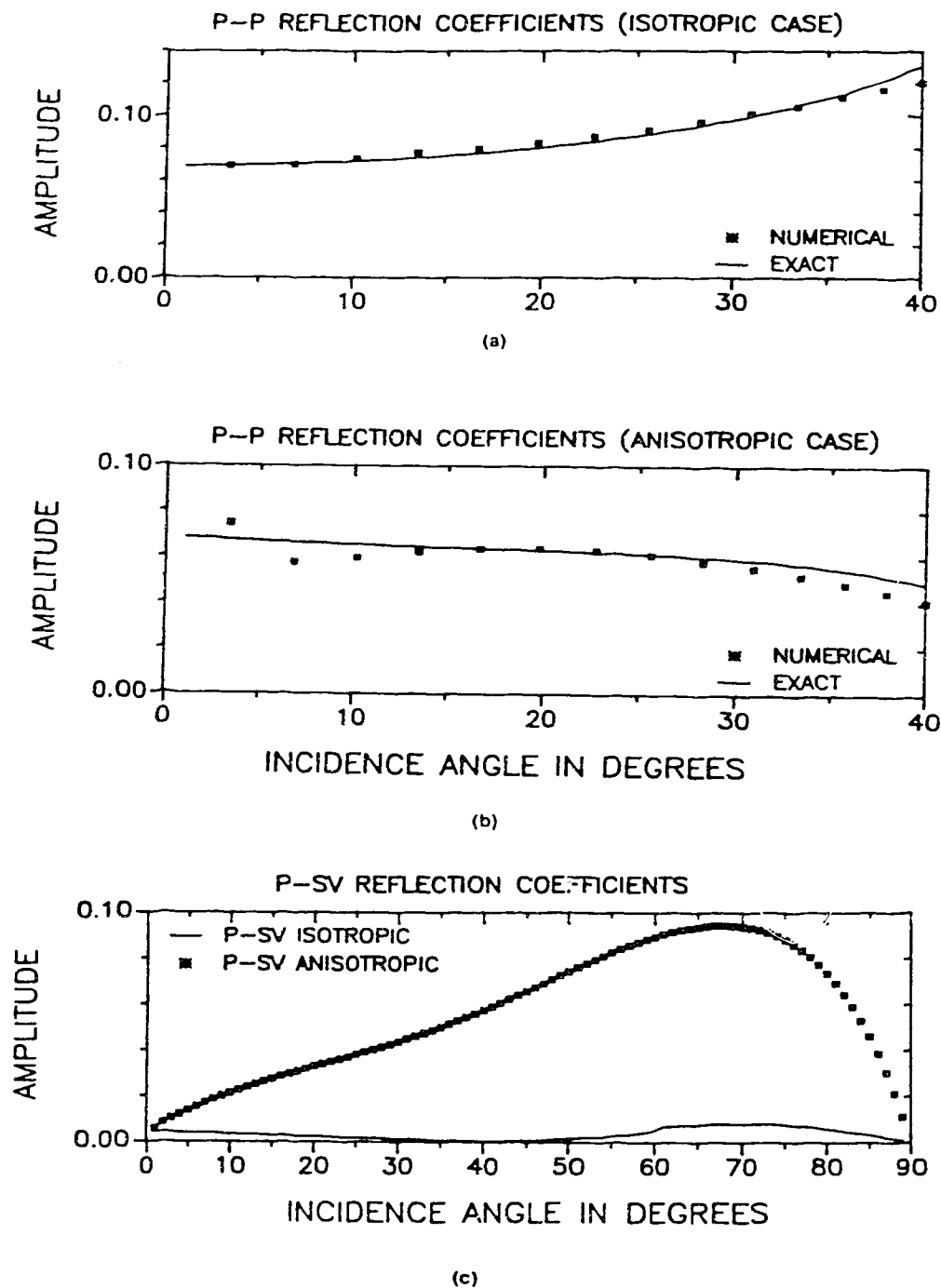


Figure 3.4 (a) Comparison between exact and numerical (predicted by the F.D. algorithm) for the P-P reflection coefficients for the isotropic case.  
 (b) Same as Fig.3.4a but with anisotropic shale.  
 (c) P-SV converted analytical reflection coefficients for the models shown in Figures 3.3b and 3.3c, respectively.



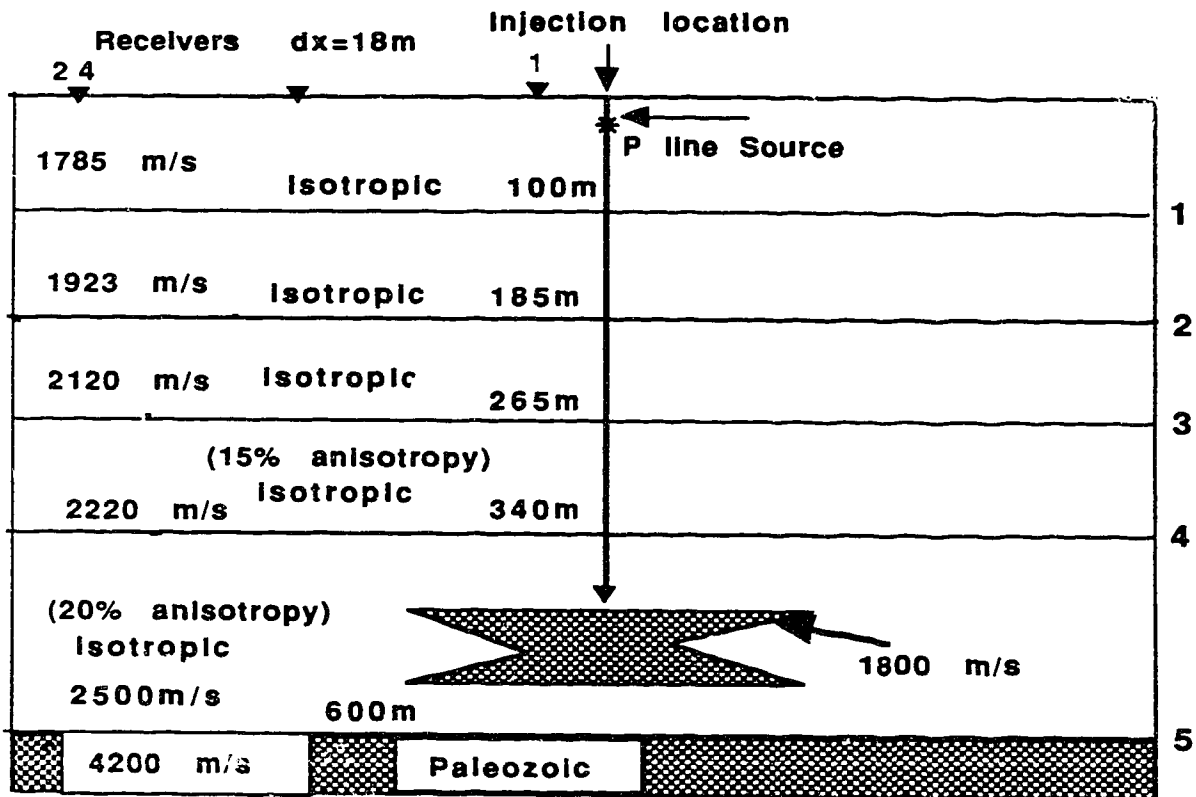
stronger compared to the isotropic case. The same conclusions can be derived by observing Figures 3.3b and 3.3c generated from the F.D algorithm.

To demonstrate the complications that can be introduced when considering anisotropy in the P-SV and SH wave propagation in heterogeneous media the following example is considered. This synthetic case illustrates the flexibility of the F.D. methods in generating synthetic seismograms for models for which analytical solutions are not known.

Figure 3.5, depicts a typical Cold Lake, Alberta depth model. Depths and velocities were assigned according to sonic logs. The inhomogeneity in the layer between interfaces #4 and #5 represents a steam zone due to the steam injected during an Enhanced Oil Recovery (EOR) process. This inhomogeneity remains isotropic throughout the example shown. Poisson's ratio for the various formations was equal to 0.3, while the Poisson's ratio in the steam zone was set to 0.4, indicating a substantial water saturation. An equivalent of 15% and 20% transverse isotropy is introduced to layers bounded by interfaces #3 and #4 and #4 and #5, respectively.

For the SH case shear velocities were assigned from the compressional velocities assuming a Poisson's ratio of 0.3. Layers #4 and #5 exhibit 15% and 20% horizontal anisotropy, respectively. The dominant frequency of the SH line source used was 20Hz the grid spacing was 6m and the time step was 1msec to avoid dispersion and stability effects. An off-end shot gather consisting of 24 traces with 18m trace spacing was generated employing the SH finite difference algorithm. Figures 3.6a and 3.6b illustrate the synthetic seismograms for the isotropic and elliptical anisotropy cases respectively. Comparing Figure 3.6a to 3.6b differences in amplitudes and phases can be observed beyond the 11<sup>th</sup> trace and at 0.7 sec. The high amplitude at the far traces and at 0.8 sec is due to the fact that critical reflections from interface #3 occur.

P-SV synthetic seismograms were generated. In particular, Figures 3.7a and 3.7b illustrate the vertical component of the particle velocity for isotropic and anisotropic cases,



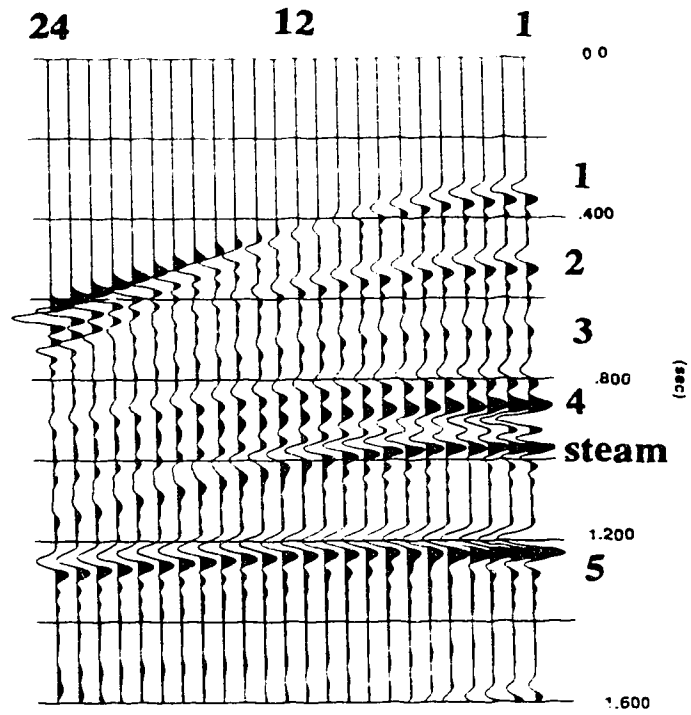
### P-SV Surface Experiment

Density of the area  $\rho = 2100 \text{ Kg/m}^3$

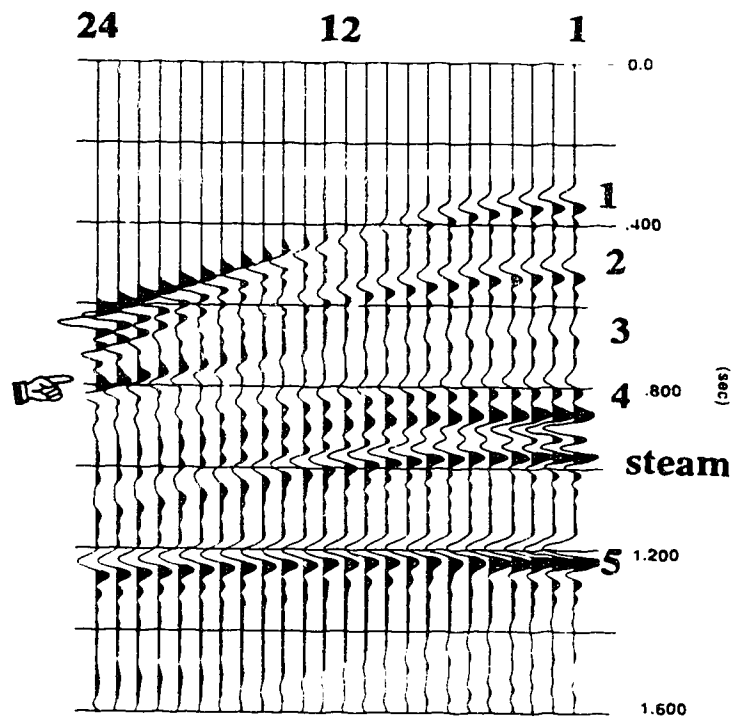
Poisson's ratio of the area  $\sigma = 0.3$

Poisson's ratio in the steam  $\sigma = 0.4$

Figure 3.5 Shallow Cold Lake, Alberta, depth model employed for the generation of the P - SV and SH synthetic seismograms including a steam zone. An arbitrary shape of the steam zone was chosen to indicate the flexibility of the F.D. algorithm.



(a)



(b)

Figure 3.6 (a) SH synthetic seismograms for the isotropic case.

(b) SH synthetic seismograms for the elliptical anisotropic case.

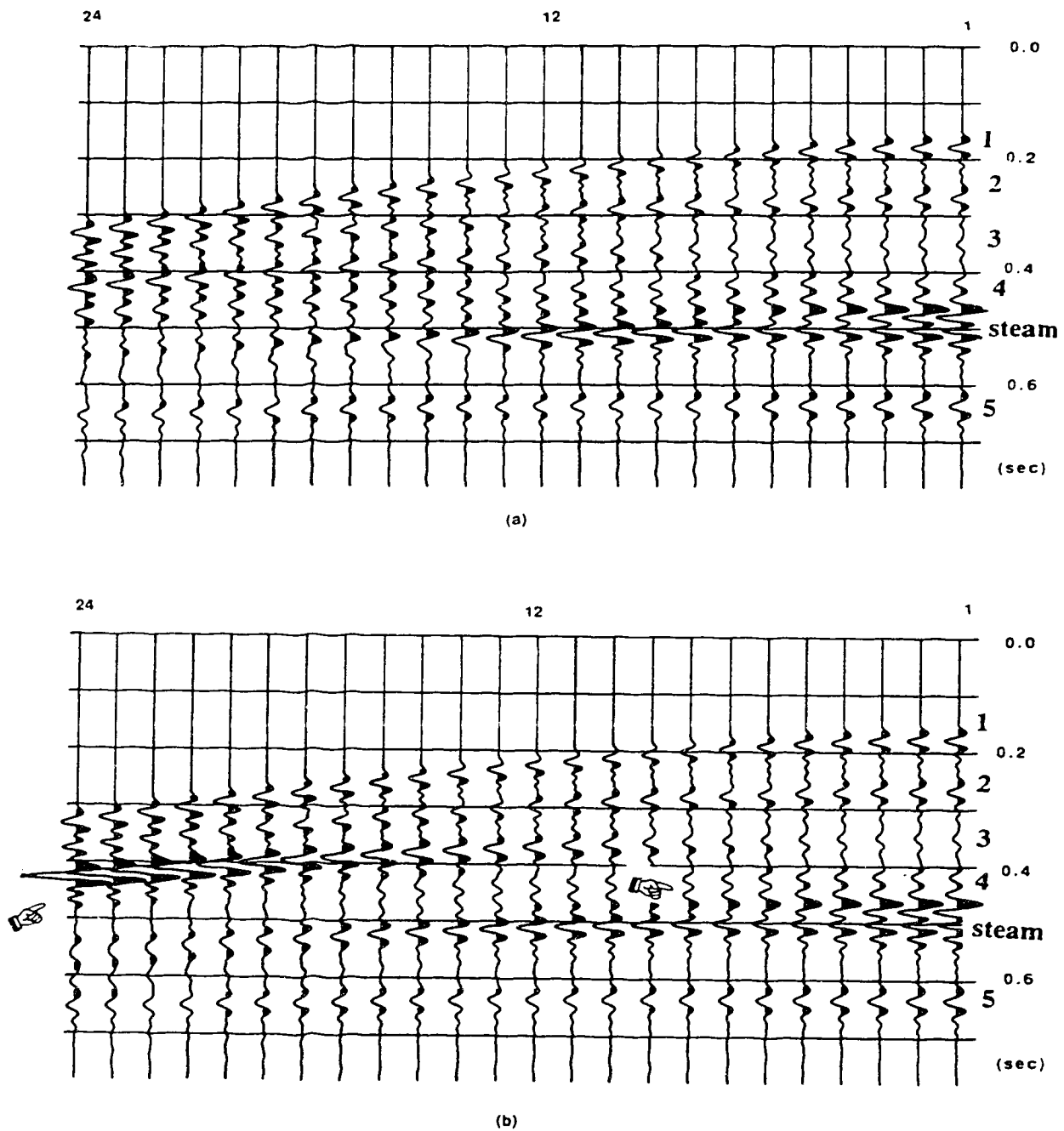


Figure 3.7 (a) P-SV synthetic seismograms for the vertical component of the particle velocity. (b) Same as Figure 3.7a except that now interfaces #3 and #4 and #4 and #5 exhibiting a transverse isotropy of 15% and 20% higher in the horizontal direction.

respectively. A P wave line source was employed having a dominant frequency of 25Hz. The grid spacing was 6m and the time step 0.5ms. Comparing Figure 3.7a with Figure 3.7b, an increase in amplitude at 0.4 sec and between 11<sup>th</sup> and 24<sup>th</sup> trace is due to postcritical reflections from interface #3. Figure 3.7b also depicts, a decrease in amplitude between 0.45 sec and 0.5 sec and between 2<sup>d</sup> and 10<sup>th</sup> trace is due to the directional velocity changes in the layer bounded by interfaces #4 and #5.

For the P-SV case, the execution time for a 240 x 240 grid size model on a CDC Cyber 205 supercomputer, was 5 minutes for a total of 1600 time steps, whereas for the SH case it was 3 minutes.

### 3.7 Conclusions

A fast and accurate finite difference algorithm for modeling the P-SV and SH wave propagation in transversely isotropic inhomogeneous media is developed. The necessity of the algorithm is clearly indicated by observing the differences caused in the dynamics and kinematics of the elastic wave propagation in such media. Since the correct full waveform representation is essential in the non-linear full waveform inversion, we believe that the present algorithm shows enormous potential for the estimation of the anisotropic parameters of inhomogeneous media.

## **CHAPTER 4**

### **SHOT GATHER MIGRATION IN $\omega$ - $x$ DOMAIN**

#### **4.1 Introduction.**

Reflection seismology seeks to determine the structure of the Earth from seismic records obtained at the surface. The seismic signal recorded by a receiver (geophone), is a superposition of seismic waves originating from all possible directions in the subterrain. Thus, much of the recorded energy is not from reflectors directly below the receiver but from horizons far away from the point of recording. The term migration refers to the redistribution of the observed wave amplitudes to their true spatial subsurface reflecting positions. Apart from the correct imaging it is a technique which increases the spatial resolution. Seismic migration is the type of processing which images the recorded echoes to their correct spatial positions based on wave theoretical considerations. More precisely, the purpose of migration is to reconstruct a reflectivity map of the Earth from the seismic data recorded at the surface.

Migration is an inverse process in which the recorded events are propagated back to the corresponding reflector locations. In the process of seismic data acquisition, the upward travelling waves are recorded at the surface. In the migration process these recorded waves are used either as initial conditions or boundary conditions for a wavefield governed by the wave equation.

#### **4.2 Migration Techniques**

There are many ways to migrate seismic data. The numerical techniques employed can generally be placed in three broad categories, namely, summation or integral methods,

difference equations or differential methods and transform methods. Since the introduction of the finite difference techniques by Claerbout (1970,1976), techniques such as the Kirchhoff summation approach (French,1975; Schneider, 1978) and f-k migration (Stolt, 1978; Gazdag, 1978) have shown encouraging results. Berkhout (1982,1984) introduced migration as a spatial convolution process in the space-frequency domain. Recently much attention is being paid to migration schemes employing the full elastic wave equation, (Wapenaar et al,1987), and to the relationship between migration and non linear elastic inversion of the seismic reflection (Tarantola, 1986; Mora, 1987).

Stacking of recordings from many source-receiver combinations is essential to improve the signal to noise ratio of the weak subsurface echoes. Corrections to the different travel times before stacking are usually carried out on the assumption of planar zero dipping reflecting beds. The stacking of 24 to 60 records not only improves the signal to noise quality but reduces the immense amount of data that must be handled by a computer array processor. The final stacked product displays a section in which the source and receiver are spatially identical for reflecting surfaces with little dip.

Post stack migration attempts to correct a stacked section for the effect of dip. Since the original field records were made with source receivers not in identical positions the obtained stack sections with dipping or discontinuous reflectors are distorted. Since migration of stacked sections is about 2 orders of magnitude (2 D cases) less expensive than current pre-stack migration methods it is the only type that is used routinely in most exploration surveys. All migration methods have the additional problem that it is necessary to have the wave velocities as a function of spatial coordinates before they can be applied accurately. Since the velocity is not known *a priori* some iteration is necessary to remove migration artifacts such as overlapping or crossing reflectors, *bow-tie* patterns, etc.

Migration of the complete unstacked data set is less common than after stack migration, but it is theoretically more correct. Prestack migration algorithms generally fall

into three categories.

1. Partial prestack migration which can be any number of schemes to remove the effects of reflector dip from the unstacked data, (Yilmaz and Claerbout, 1980; Hale, 1984).
2. Full double downward continuation prestack migration, sometimes called shot-geophone migration because both source and receiver coordinates are downward continued (Schultz and Sherwood, 1980; Weglein, 1982).
3. Common shot gather or profile migration in which the receiver coordinates are extrapolated downward and correlated with the calculated downgoing wave from a single source. At every point of interest in the Earth, correlate the calculated upgoing and downgoing waves. Where the correlation is finite a reflector exists with reflectivity proportional to the correlation (Berkhout, 1982; Wapenaar et al, 1987). The migration of a single profile will not, in practice, give a complete subsurface picture. Only points illuminated by the source and seen by the limited number of receivers will show up in a single profile migration. However, by migrating many shot gathers, a complete image of the subsurface is obtainable. The acoustic approximation in seismic migration is allowed when the effects of the wave conversion are neglected.

### **4.3 Extrapolation and Imaging.**

There are two distinct parts to migration, namely, extrapolation and imaging. Extrapolation means a reconstruction from surface data of the wavefield at depth. Imaging must be based on some principle which allows us to obtain the local reflection strength from the extrapolated data. To obtain an image of subsurface reflectors from seismic data, an imaging principal has to be invoked. This principal is just a prescription for constructing a picture of the subsurface from the data. Several imaging principles have been put forward and will be discussed in the following paragraph. Generally, they have been common sense



ideas leading to different types of migration.

A common midpoint (CMP) section may be regarded as data obtained from coincident source and receivers. In this zero offset model, the energy travel path from source to reflector is identical to that from reflector to receiver. The assumption is that all sources activated simultaneously, but each receiver records signals originating from the same source - receiver point. Such zero offset data do not correspond to any wavefield resulting from a simple experiment. As a result it is helpful to create a hypothetical physical experiment to provide an intuitive picture of zero offset migration. Such an experiment is known as the Exploding Reflector Model, (Lowenthal et al,1976).

According to the ERM the energy sources are not at the surface, but they are distributed along the reflecting surfaces. In other words, the reflectors are represented by buried sources, which are "exploded" at the same time  $t=0$ . Therefore one needs to be concerned only with upward traveling waves. Since the record section involves two-way travel time, it needs to be converted to one-way travel time. In practice the time scale of CMP sections is kept unchanged. Instead the velocity of the wave propagation is scaled down by a factor of two.

A different imaging principle is based on the idea that *a reflector exists at points in the Earth where an upgoing wave is time coincident with the first arrival of a downgoing wave*. This leads naturally to an algorithm which extrapolates both up and downgoing wavefields to points of intersection, to obtain a reflection coefficient by correlation. Data taken at the Earth's surface is considered an upgoing wave, which can be extrapolated down into the Earth and backwards in time. Sources are considered to generate downgoing waves, which can also be extrapolated down into Earth but forward in time. Comparison with the extrapolated upgoing wave of the first arrival of the extrapolated downgoing wave yields a reflection coefficient. This concept leads naturally to pre-stack migration or common shot gather (CSG) migration which is capable of forming a subsurface image

from a single shot experiment.

#### **4.4 Single shot depth migration**

The term single shot depth migration used here indicates that the input for seismic imaging is the reflected energy from a source at a unique location into closely spaced receivers at 24 to over 100 surface locations. Migration of these common shot gathers is an alternative to the common depth point (CDP) processing and can give correct imaging and better dip preservation and amplitude information. In fact if the reflector is curved, CDP migration leads to an incorrect conclusion regarding the reflection coefficient amplitudes, (Temme, 1984). Due to the fact that a common shot gather is collected from a single experiment, the subsequent data processing can be implemented with fewer restrictions and approximations. The need for an accurate migration that will avoid the CDP processing stacking artifacts is recognized and has induced several authors to suggest methods for prestack migration and common shot migration (Jain and Wren, 1980; Schultz and Sherwood, 1980; Yilmaz and Claerbout, 1980; Temme, 1984; Wapenaar et al, 1987; Reshef and Kosloff, 1986; Chang and McMechan, 1986; Muller and Temme, 1987; Berkhout, 1987). An extensive review on the prestack migration techniques is given in Stolt and Benson (1986).

In seismic sounding the measurements of a physical experiment consists of one common shot gather. The data of a single shot record is fully described by the wave equation for seismic waves. In seismic wave theory the subsurface is considered as a linear time - invariant system. This means that any broad band type experiment may be seen as the superposition of many fully independent, monochromatic experiments. Consequently, the seismic data is decomposed into a series of monochromatic shot records. Each simple monochromatic shot record is described by the wave equation and can be modeled or migrated independently from any other one. Obviously, this is a more manageable and

efficient space to operate and is susceptible to a parallel processing computer environment. Also, in the frequency - space domain the imaging step for the shot gather migration is accomplished by a simple time exponential shifting term.

The present method employs the 45<sup>0</sup> parabolic approximation to the scalar wave equation in the  $\omega$ - $x$  domain for the extrapolation of the upgoing wavefield (Claerbout, 1976, 1985). Instead of using the amplitude values at time equal to zero, as in poststack migration, the depth section now consists of amplitudes at the time of arrival of the direct wave from the source to any point in the subsurface. The direct arrival time is calculated through solutions of the eikonal equation employing a fourth order Runge - Kutta integration method (Tsingas and Kanasevich, 1989).

Migration can be accomplished employing the full scalar wave equation (Kosloff and Baysal, 1983; Reshef and Kosloff, 1986). For strong lateral velocity variations and steep dips the two-way scalar wave equation is superior to the parabolic or paraxial wave equation. The scalar wave equation is a partial differential equation of second order in depth ( $z$ ), and hence has two solutions, which correspond to upgoing and downgoing propagating waves. Thus, the scalar wave equation will generate unwanted internal multiple reflections for strong velocity variations. In building a migration algorithm we do not want to have energy moving around that does not contribute to the focused image. The scalar wave equation with variable coefficients will generate such energy. This unwanted energy is especially troublesome if it is coherent and migrates to a time when primaries are weak.

Also, the fact that the scalar wave equation is of second order in depth ( $z$ ), means that we need two boundary conditions for extrapolation. It seems natural that these boundary conditions will be pressure  $P$  at  $z=0$ , and the first derivative of pressure i.e.  $\partial P/\partial z$  at  $z=0$ . But  $\partial P/\partial z$  is not recorded and it is unknown. However, Kosloff and Baysal (1983), showed a way to calculate this factor from the recorded data assuming a constant

near surface velocity. For the  $\omega$  -  $x$  migration employed here we shall make use of the 45° parabolic wave equation since most seismic sections over the heavy oil environments have dips of only few degrees.

The examples used here are based on synthetic cases for simple structures. Exact synthetic seismograms are calculated using a finite difference solution of the elastodynamic wave equation described in Chapter 3, assuming isotropic media.

#### 4.5 Theory of the $\omega$ - $x$ migration

Start with a field  $P(x,z,t)$  which represents pressure and which obeys the wave equation for constant density:

$$\frac{\partial^2}{\partial x^2} P(x,z,t) + \frac{\partial^2}{\partial z^2} P(x,z,t) = \frac{1}{v^2(x,z)} \frac{\partial^2}{\partial t^2} P(x,z,t) \quad (4.1)$$

where,  $x$  and  $z$  are the spatial and depth coordinates and  $v(x,z)$  is the acoustic velocity of the medium. Taking the Fourier transform of both the spatial and temporal coordinates one obtains the well known dispersion relation for the scalar wave equation, assuming that  $v(x,z)$  is the local constant velocity of the medium:

$$k_x^2 + k_z^2 = \frac{\omega^2}{v^2(x,z)} \quad (4.2)$$

where,  $k_x$  and  $k_z$  are the horizontal and vertical wavenumbers, respectively and  $\omega$  is the angular frequency.

A solution for  $k_z$  is:

$$k_z = \pm \frac{\omega}{v} \sqrt{1 - \frac{v^2(x,z) k_x^2}{\omega^2}} \quad (4.3)$$

Choice of the sign in front of the square root gives us the upcoming or downgoing waves. The direction of the wave depends on the relationship of  $z$  and  $t$  that is required to keep the phase constant in the expression  $\exp(-i\omega t + ik_z z)$ . If  $\omega$  were always positive, then  $+k_z$  would always refer to a downgoing wave and  $-k_z$  to an upcoming wave. Thus keeping the minus sign we select upcoming waves.

For the inverse transform of the  $z$  axis, we need to recognize that the  $ik_z$  corresponds to  $\partial/\partial z$  (where  $i = \sqrt{-1}$ ) and  $k_x^2$  corresponds to  $-\partial^2/\partial x^2$ . Then by applying the operator given by equation (4.3) to the temporal Fourier transformed  $P'(x,z,\omega)$  of the upcoming wavefield  $P(x,z,t)$ , and multiplying throughout by  $i$  we have:

$$\frac{\partial P'}{\partial z} = -i \frac{\omega}{v} \sqrt{1 - \frac{v^2(x,z) k_x^2}{\omega^2}} P' \quad (4.4)$$

Bringing (4.4) into the spatial domain is not simply a matter of substituting a second  $x$  derivative with  $k_x^2$ . The problem is the efficient and accurate evaluation of the square root of a differential operator. The square root is approximated by continued fractions expansion (Claerbout, 1985) according to:

$$R_{n+1} = 1 - \frac{f^2}{1+R_n}$$

with  $f = v(x,z) k_x/\omega$ , and  $R_0 = 1$ , where  $n$  indicates the order of expansion.

Then collecting up to second order ( $n=2$ ) truncation of the continued fraction expansion,

equation (4.4) becoms:

$$\frac{\partial P'}{\partial z} = -i \left( \frac{\omega}{v(x,z)} - \frac{k_x^2}{2 \frac{\omega}{v(x,z)} - \frac{v(x,z) k_x^2}{2 \omega}} \right) P' \quad (4.5)$$

Claerbout (1976;1985) showed that employing a retarded coordinate transformation one removes the effect of vertical translation thereby making the wave appear to be stationary.

The time retarded coordinates are a system which is fixed in space relative to the ordinary Cartesian coordinate system. The retarded coordinate system is related through the local velocity,  $v(z)$  at each source location to the Cartesian system by the set of equations, (Claerbout, 1985):

$$\begin{aligned} t' &= t'(x,z,t) = t + \int_0^z dz/v(z) \\ x' &= x'(x,z,t) = x \\ z' &= z'(x,z,t) = z \end{aligned} \quad (4.6)$$

The pressure wavefield can be written in terms of a stationary wave  $Q(x,z,\omega)$  in the frequency domain as:

$$P'(x,z,\omega) = Q(x,z,\omega) e^{-i\omega \int_0^z \frac{dz}{v(z)}} \quad (4.7a)$$

or

$$Q(x,z,\omega) = P'(x,z,\omega) e^{i\omega \int_0^z \frac{dz}{v(z)}} \quad (4.7b)$$

The retarded wavefield  $Q$  has the practical advantage over  $P'$  because, being more slowly variable with the  $z$  coordinate, it may be sampled less densely thereby conserving computational effort. Differentiating (4.7a) with respect to  $z$  gives:

$$\frac{\partial P'(x,z,\omega)}{\partial z} = \left[ \left( \frac{\partial}{\partial z} - \frac{i\omega}{v(z)} \right) Q(x,z,\omega) \right] e^{i\omega \int_0^z \frac{dz}{v(z)}} \quad (4.8)$$

Substitute (4.7a) and (4.8) into (4.5) we get the time shifted upcoming wavefield:

$$\frac{\partial Q(x,z,\omega)}{\partial z} = i \frac{k_x^2}{2 \frac{\omega}{v(x,z)} - \frac{v(x,z)}{2 \omega}} Q(x,z,\omega) - i \omega \left( \frac{1}{v(x,z)} - \frac{1}{v(z)} \right) Q(x,z,\omega) \quad (4.9)$$

The first term on the right hand side represents the *diffraction term* and the second term in the right hand side represents the *thin lens* term. In the above derivation we assume that  $v(x,z)$  is a local constant medium velocity and  $v(z)$  depends on depth below the source, only. For a smoothly and gradually varying medium, no serious limitations are imposed on the above assumption. This equation may be rearranged and substituting for:

$$-k_x^2 = \partial^2 / \partial x^2, \text{ and } m(x,z) = \omega / v(x,z),$$

the diffraction term is given by:

$$- 2 i m(x,z) \frac{\partial Q(x,z,\omega)}{\partial z} - \frac{i}{2 m(x,z)} \frac{\partial^3}{\partial x^2 \partial z} Q(x,z,\omega) + \frac{\partial^2}{\partial x^2} Q(x,z,\omega) = 0$$

(4.10)

The thin lens term may be incorporated as correction with the evaluation of (4.10) and is given by:

$$thin\ lens = - i \omega \left( \frac{1}{v(x,z)} - \frac{1}{v(z)} \right) Q(x,z,\omega)$$

(4.11)

Equation (4.10) is the well known 45<sup>0</sup> paraxial (or parabolic) approximation to the scalar wave equation. In addition equation (4.10) is a partial differential equation of first order in  $z$  and requires only one boundary condition at  $z=0$  for its solution. The coordinate  $x$  varies along the offsets on the surface of the shot gather which has to be migrated. The  $z$  variable ranges from the surface to the maximum desirable depth which we want to migrate. Thus side boundary conditions have to be employed to avoid artificial reflections which can influence the solutions. The paraxial absorbing boundary conditions were employed at the sides of the model according to Clayton and Engquist (1980), and their effectiveness is depicted in Appendix B4.

The present migration algorithm is based on the downward continuation of the upcoming waves employing an implicit Crank - Nicolson finite difference approximation of the parabolic equation (4.10). For long spatial wavelengths the two terms, namely, the thin lens and the diffraction term commute and as a result the depth migration algorithm is based on marching forward by a small depth step,  $\Delta z$ , alternately, solving the two equations given by (4.10) and (4.11). In other words to propagate one depth step, first apply the diffraction term on the wavefield  $Q$ . The thin lens term then is applied to the output from



the diffraction calculation (Yilmaz, 1987, Claerbout, 1985). Stability is assured because the stability of each separate extrapolation is known. The present finite difference algorithm is unconditionally stable as shown in the Appendix B. The discretization procedure for the downward extrapolation of the upcoming field is given in the Appendix B1, together with a formulation to solve the resultant triadiagonal system of equations (Appendix B2).

The main difference from the zero offset migration is the imaging condition and the fact that in the shot gather migration the true medium velocity should be used instead of the half value as in the zero offset migration. Assuming that a reflector exists whenever the direct wave from the source and the reflected are coincident, the depth section will consist of wave amplitudes at the given depth location at the time of the arrival of the direct wave. If  $P(x, z=0, t)$  represents the recorded common shot gather at the earth's surface, the final section will consist of  $M(x, z, t_d)$ , where  $t_d(x, z)$  is the arrival time of the direct wave from the source to the depth points  $(x, z)$  computed by an exact ray tracing algorithm (see Appendix C). A full description of the ray tracing algorithm is described in a later section. Since our calculations are done in the frequency domain, the final depth section employing the appropriate imaging condition is given by:

$$M(x, z, t_d) = \sum_{\omega} Q(x, z, \omega) e^{-i \omega t_d(x, z)} \quad (4.12)$$

where the summation is over the seismic frequency band. Consequently, the input for the common shot gather migration consists of the pressure wave field at the earth's surface  $P(x, z=0, t)$  the medium velocity  $v(x, z)$  and the direct travel time arrivals  $t_d(x, z)$ .

#### 4.6 The $\omega$ - $x$ migration and stacking algorithm.

A flow chart of the described algorithm is depicted in Figure 4.1. The necessary steps for the shot gather migration are as follows:

1. Having a reliable velocity model, we compute the direct travel time arrivals from each source location to any subsurface point within the illuminated area.
2. Then, we take the Fourier transform of the recorded surface field  $P(x, z=0, t)$  namely,  $P'(x, z=0, \omega)$ .

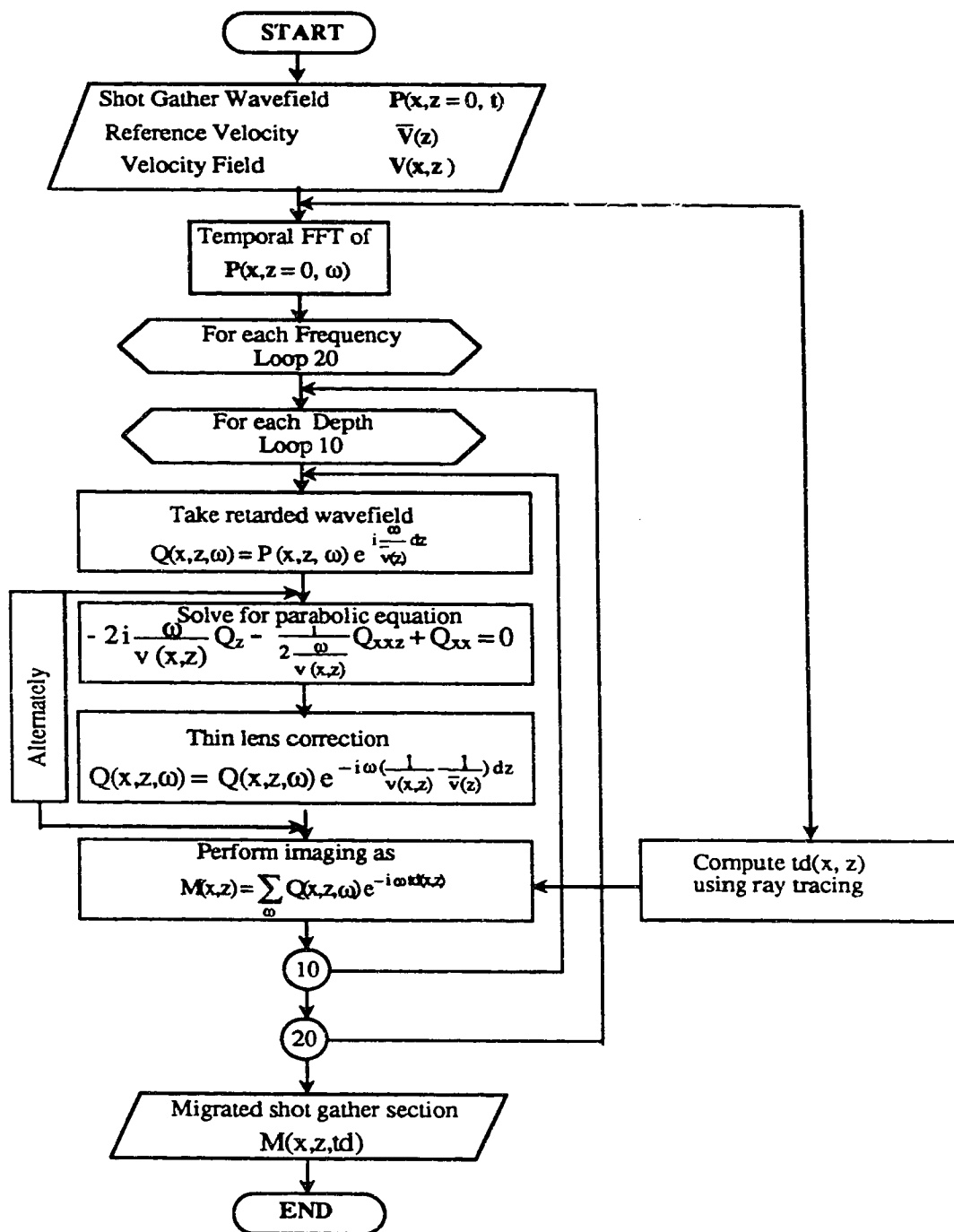
For each depth step, and for all frequencies:

3. We perform a time shift by taking equation (4.7b) and thus we evaluate the shifted wavefield  $Q(x, z, \omega)$ ,
4. For each depth step  $\Delta z$ :
  - a) We solve equation (4.10) using an implicit Crank-Nicolson finite difference algorithm (see Appendix B) for the retarded  $Q(z+\Delta z, x, \omega)$  wavefield,
  - b) Correct for the thin lens term (if one has lateral variable velocity) by solving analytically equation (4.11),
5. We perform the imaging condition for the  $Q$  wavefield by employing equation (4.12).

The final migrated section is computed by a common geophone stacking of the individual migrated shot gathers according to:

$$M_m(x_g, z) = \sum_{x_s} W(x, z) * M(x_s, x_g, z) \quad (4.13)$$

where  $x_g$  and  $x_s$  represent geophone and shot locations, respectively. The  $W(x, z)$  represents a spatial window which is applied before the stacking of the shot gathers and is based on the specific ray illumination from the source to each depth point in the subsurface.

Figure 4.1 Flow-chart of the  $\omega$  -  $x$  shot gather depth migration

#### 4.7 Comparison of the dispersion relations between the wave equation and the parabolic wave equation.

As was shown previously, the exact dispersion relation of the scalar wave equation for a downgoing wave is given by:

$$k_z = \sqrt{k^2 - k_x^2}$$

or in normalized form as:

$$\frac{k_z}{k} = \sqrt{1 - \frac{k_x^2}{k^2}}$$

(4.14)

where,

$k$  is the wavenumber and is equal to  $k = 2\pi / \lambda$  where  $\lambda$  represents a dominant wavelength,  $k_z$  is the vertical wavenumber and is equal to  $k_z = k \cos\theta$ ,  $k_x$  is the horizontal wavenumber  $k_x = k \sin\theta$  where  $\theta$  is the angle of the wavefront propagation measured from the vertical axis. For the 45<sup>0</sup> differential parabolic wave equation, the normalized dispersion relation is derived in Appendix C eq. (C3) and is equal to :

$$\frac{k_z}{k} = \frac{3k_x^2 - 4k^2}{k_x^2 - 4k^2}$$

(4.15)

In Appendix C, formula (C9) depicts the normalized dispersion relation for the finite difference approximation of the 45<sup>0</sup> approximation and is given by:

$$\frac{k_z}{k} = 1 + \frac{2}{k \Delta z} \tan^{-1} \left( \frac{2 \sin^2(k_x \Delta x / 2)}{\left[ \frac{1}{k \Delta z} + \frac{4 k \gamma \Delta x^2}{\Delta z} \right] * 2 \sin^2(k_x \Delta x / 2) - \frac{2 k \Delta x^2}{\Delta z}} \right) \quad (4.16)$$

where  $\Delta x$  and  $\Delta z$  represent the spatial sampling intervals for the horizontal and vertical axes respectively, and  $\gamma = 1/12$  from the Douglas formula (Appendix B eq. B2).

Figure 4.2, depicts a comparison of the exact dispersion relation (equation 4.14) with the dispersion relation derived for the differential 45<sup>0</sup> approximation (equation 4.15). We see the departure from the exact dispersion at  $k_x > 0.80$  and  $k_z < 0.60$ . In Figure 4.3, the exact dispersion relation is compared with the dispersion relation derived for the finite difference approximation (equation 4.16) with  $\Delta x / \lambda = 1/4$  and  $\Delta z / \lambda = 1/10$ . Clearly, for the same  $k_x$  and  $k_z$  values the algorithm starts to deviate substantially from the true wave equation.

Figure 4.4 compares the finite difference paraxial approximation to the wave equation with the full wave equation in terms of the wave propagation angle. Up to 45<sup>0</sup> - 50<sup>0</sup> the two dispersion relations are in agreement, whereas for propagation angles beyond 45<sup>0</sup> - 50<sup>0</sup> the solution starts to deteriorate. In particular Figure 4.4, depicts the accuracy of the algorithm for the same ratios of  $\Delta x / \lambda$  and  $\Delta z / \lambda$  as used in the prestack migration examples i.e.  $\Delta x / \lambda = 1/4$  and  $\Delta z / \lambda = 1/10$ . Waves propagating higher than 55<sup>0</sup> do not image properly.

#### 4.8 Computation of the direct travel time arrivals.

The calculation of the direct time arrivals is performed via a ray tracing procedure. A description of the first order ordinary system of equations of ray tracing in two

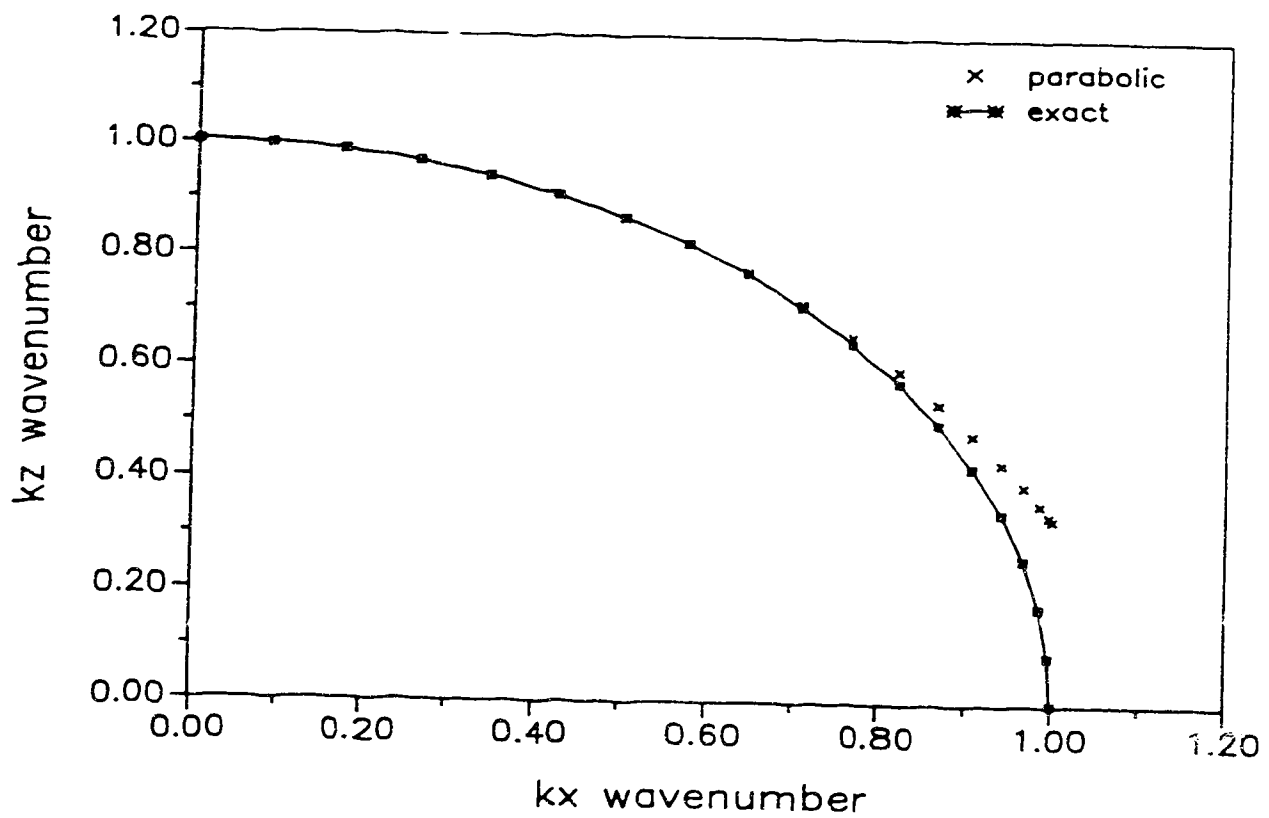


Figure 4.2. Comparison of the dispersion relations of the exact scalar wave equation to the differential parabolic approximation

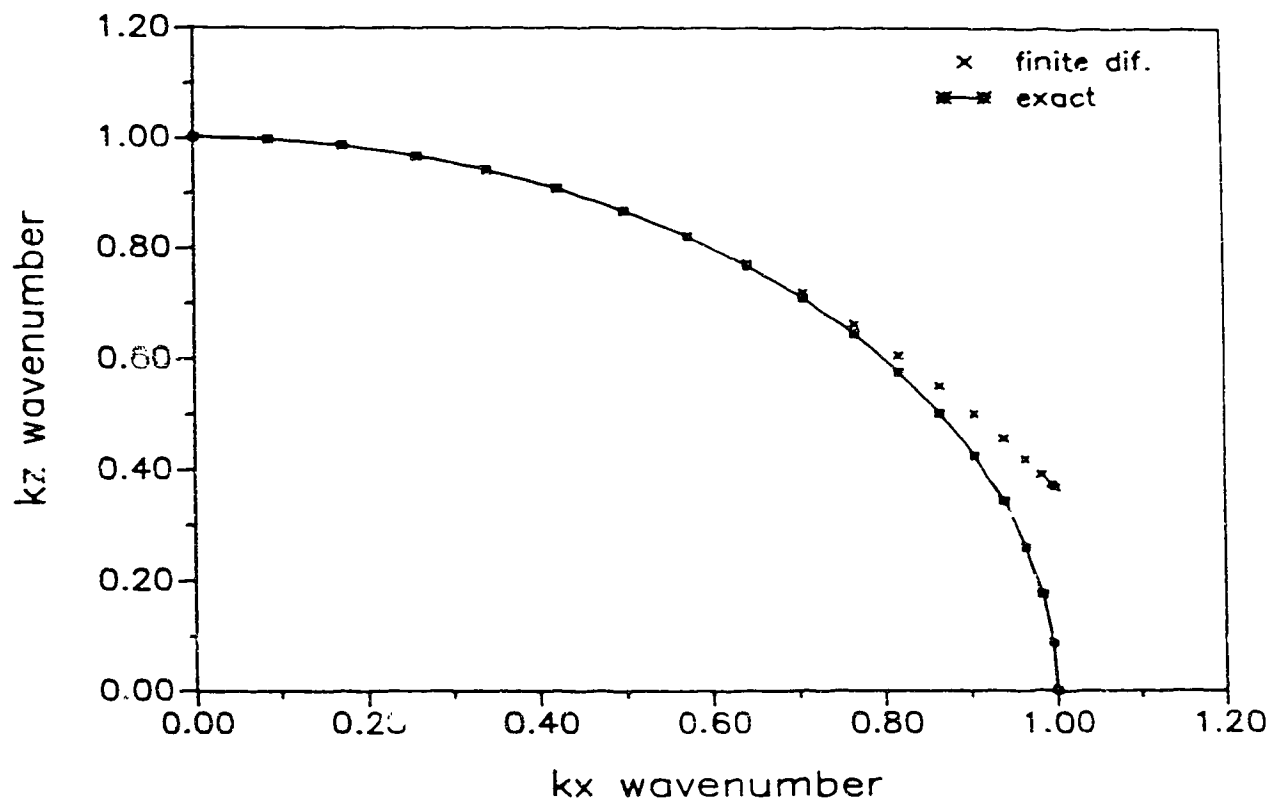


Figure 4.3 Comparison of the dispersion relations between the exact scalar wave equation to the finite difference approximation of the parabolic equation.

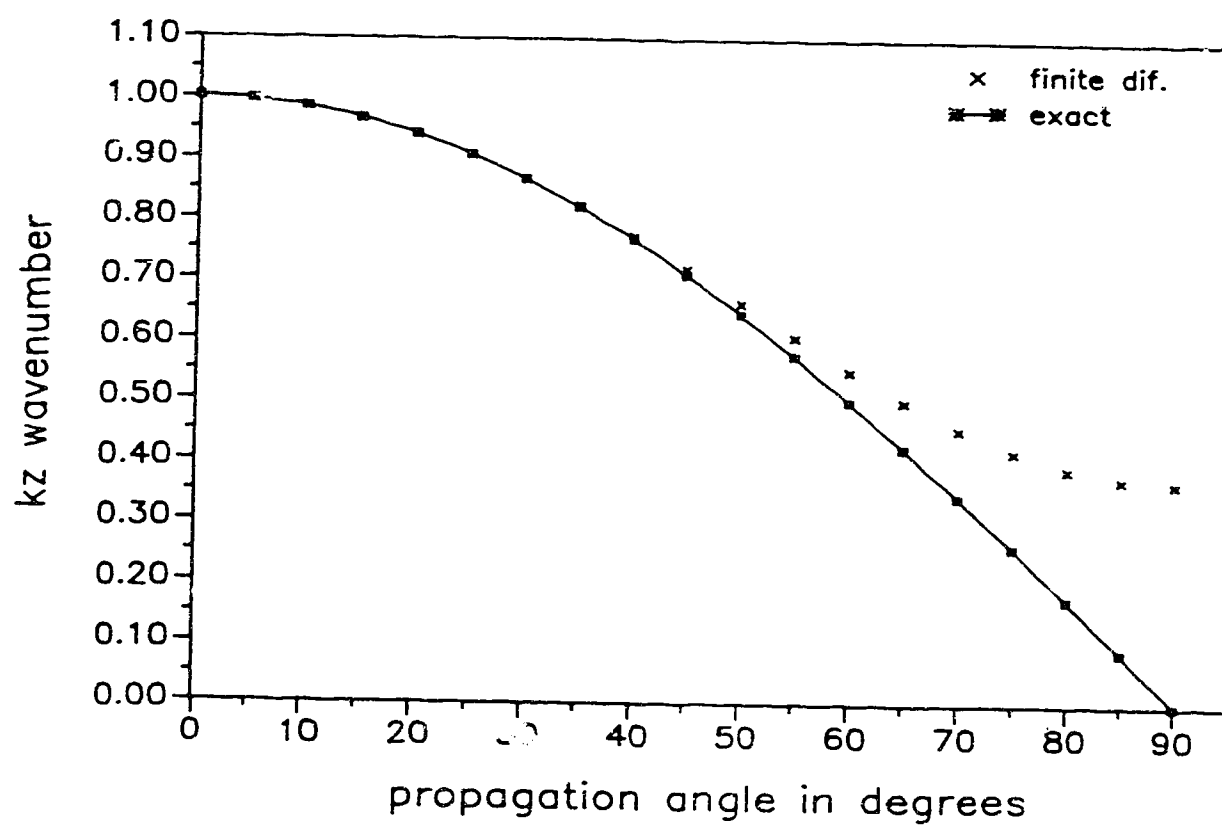


Figure 4.4 Same as Figure 4.3 but in terms of wave propagation angle.



dimensions is given in Cerveny and Ravindra (1971) and is depicted in Appendix D. The solution of the differential equations for rays in inhomogeneous media is best approximated by numerical methods.

In this algorithm the system of the three first order ordinary differential equations (see Appendix D) is solved employing the fourth order Runge-Kutta integration method (Johnston, 1982). When velocity varies laterally the present prestack migration algorithm requires that rays be traced from each source location to each depth point in the section. Based on Fermat's principle which states that, *the change in travel time with respect to the change of the ray path is zero*, the ray tracing algorithm can be described as follows.

The slowness (reciprocal of the velocity) is written as the sum of two functions, the first of which is large and depends on depth, while the other is small and varies both with depth and position along the line. Using the system given in Appendix D, the ray paths are calculated for the first slowness function and are used for the computation of the direct time arrivals for each subsurface point. For the same depth points, the previously computed ray paths are used to calculate traveltimes perturbations due to the laterally varying part of the slowness. The traveltimes perturbations are added to the previous calculated time arrivals for each depth point.

Wenzel (1988), and Carter and Frazer (1984), used the same approach for the computation of the migration curves needed to perform Kirchhoff migration for laterally varying media. Fawcette and Clayton (1984), employed this linearized approach for the tomographic reconstruction of velocity anomalies.

A flexible two dimensional ray tracing algorithm is developed to model the kinematic characteristics of the wave propagation in the unperturbed media for the computation of the direct time arrivals from a specified source to each point at the subsurface.

Once a two dimensional depth model is specified with depth horizons represented

by spline functions and velocities are assigned to each horizon, the algorithm starts tracing rays. Three initial conditions need to be given namely, the source coordinates  $x_0$  and  $z_0$  and the departure angle of the ray. The angle increment is also specified. When the ray finds an intersection point with an horizon, the normal to the interface is calculated by taking the gradient of the spline function and substituting the coordinates of the point into it. The angle of incidence is obtained from the dot product between the normal to the surface and the direction cosines of the ray, Shah (1973). Using Snell's law the transmitted angle can be calculated given the velocities of the adjacent layers. Given the transmitted angles the algorithm continues to ray trace until another interface is been reached. When a ray reaches the last specified interface the algorithm continues with a next new ray according to the ray increment. When a critical angle for a reflected wave is been observed the ray stops at that point and the algorithm starts tracing a new ray.

Next a two dimensional interpolation is performed to collect the direct time arrivals at the corresponding grid points to be used for the imaging operation performed during the shot gather migration according to equation (4.12).

#### **4.9 Muting of the migrated shot gathers.**

In migrating common shot gathers one has to be very careful regarding the subsurface coverage according to each shot location and the receiver geometry. Also, one has to check if the subsurface has a regional dip. Then, subsurface depth points illuminated by the shot can be evaluated by ray tracing and as a result an offset - depth muting window can be applied to the migrated shot gather before stacking. This way spurious reflections and migration artifacts caused by the limited subsurface coverage due to the shot - receiver locations will not contribute to the stack of each migrated shot gather.

#### 4.10 Examples

Figure 4.5b illustrates the finite difference operator of the present depth migration algorithm due to a time impulse depicted in Figure 4.5a. For a constant velocity medium and according to the imaging condition the f.d. operators response should form a semicircle in the x-z space with a radius of  $z = v * t$ , where v is the velocity of the medium and t is the one - way travel time. Since we are using the 45<sup>0</sup> parabolic wave equation the f.d operators start to deteriorate at about 50<sup>0</sup>.

To demonstrate the applicability of the present shot gather migration method a number of synthetic and real examples are considered in this section. Figure 4.6 depicts a syncline model with the appropriate interval velocities shown. Figure 4.7 illustrates the SH synthetic seismograms generated employing the depth model shown in Figure 4.6. The synthetic shot gather consists of 48 traces and it was computed employing a (2,4) SH finite difference algorithm. The trace spacing is 18m and a split spread geometry was used. An SH line source was employed having a dominant frequency of 25Hz. The finite difference time step was 1ms and the grid interval was set at 6m in order to satisfy stability criteria and dispersion effects, respectively. The direct arrivals have been removed. The direct travel time arrivals have been computed analytically. Figure 4.8 illustrates the migrated result of the shot gather. The image agrees very well with the original depth model (continuous line superimposed on the depth section) for the corresponding subsurface coverage.

The next depth model considered is shown in Figure 4.9 and consists of a number of flat layers and a low velocity thin lens within a layer. The unperturbed ray paths are also shown in the same diagram. Figure 4.10 illustrates the split spread shot gather computed by employing a (2,4) P-SV finite difference formulation. A P wave line source was employed having a dominant frequency of 25Hz. The grid spacing was 6m and the time step was set at 0.5 ms. The shot gather shown consists of 48 traces with 18m trace

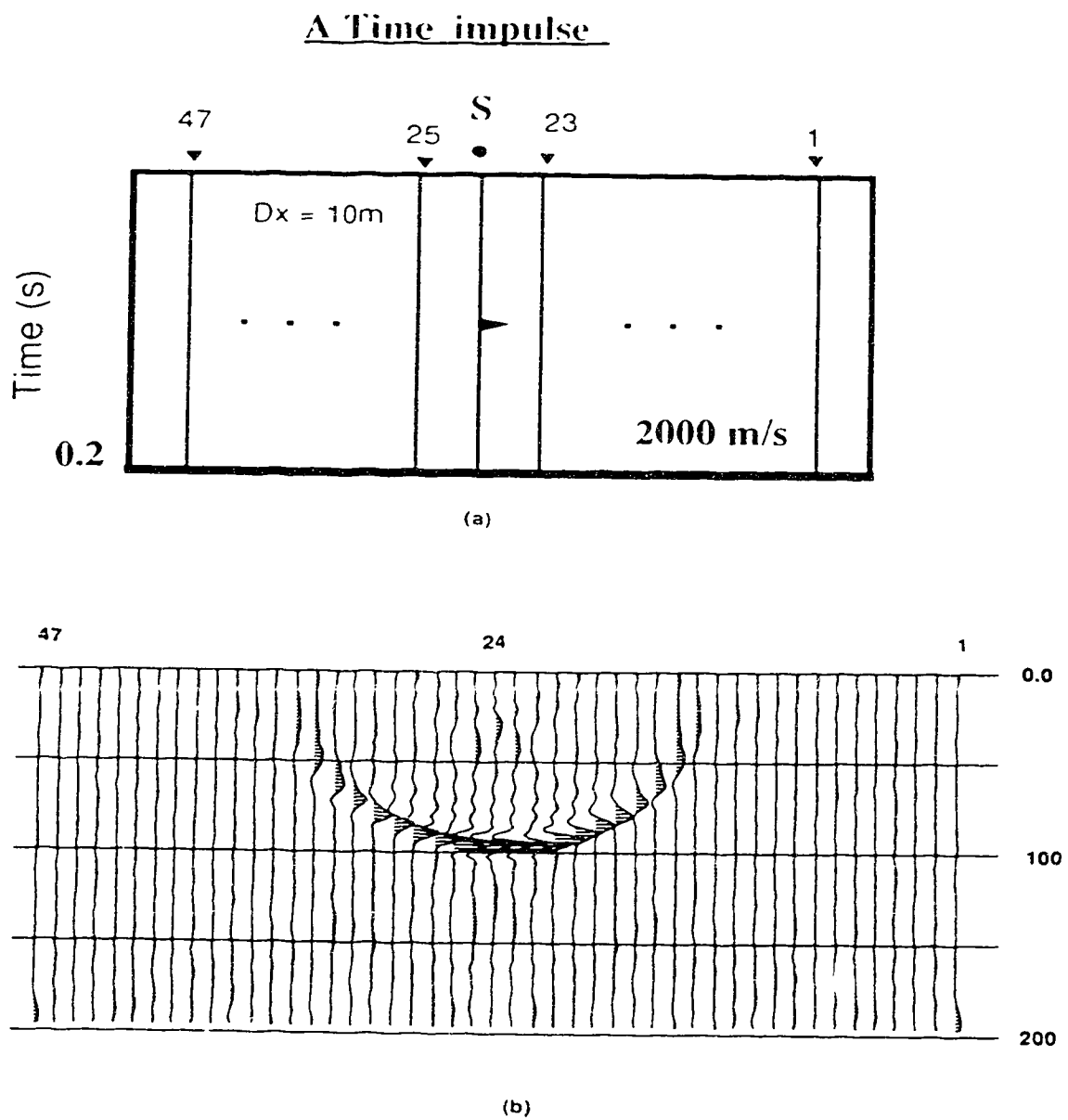


Figure 4.5 (a) Time impulse located at 100 ms.

(b) Impulse response of the shot gather  $\omega$  -  $x$  depth migration algorithm.

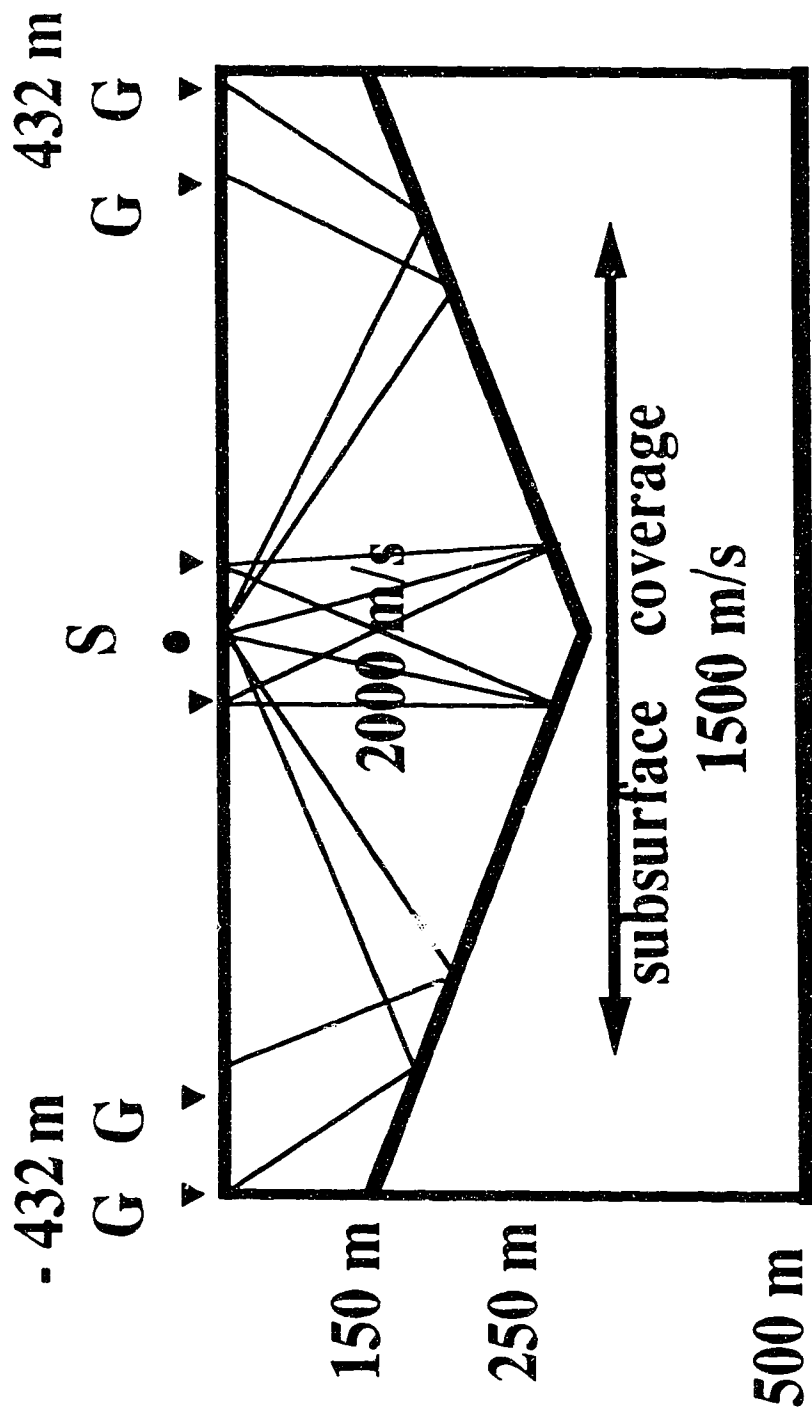


Figure 4.6 Syncline depth model ( **S**= source location, **G** = receiver location).

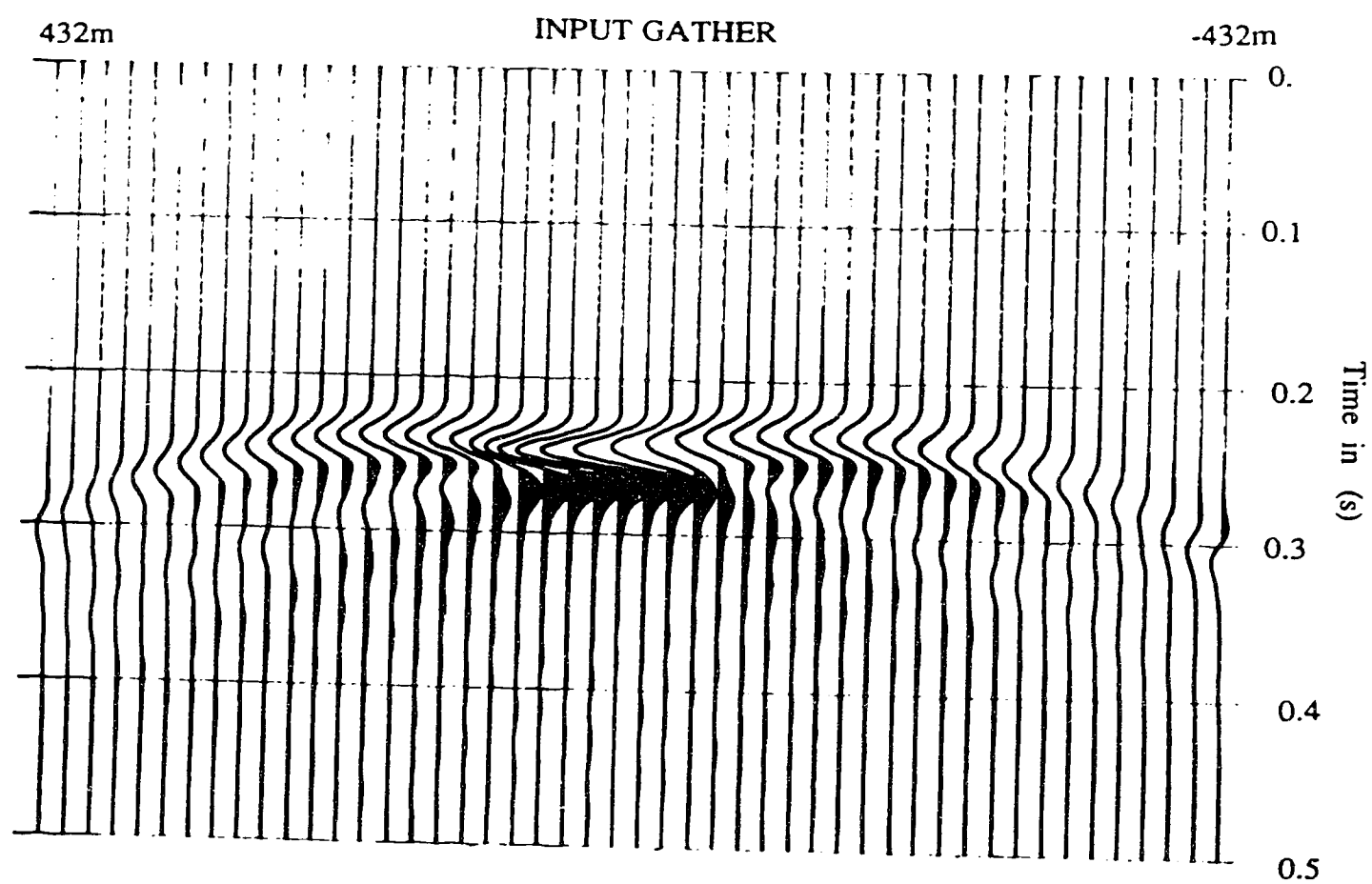


Figure 4.7 SH synthetic split spread shot gather for the syncline model.

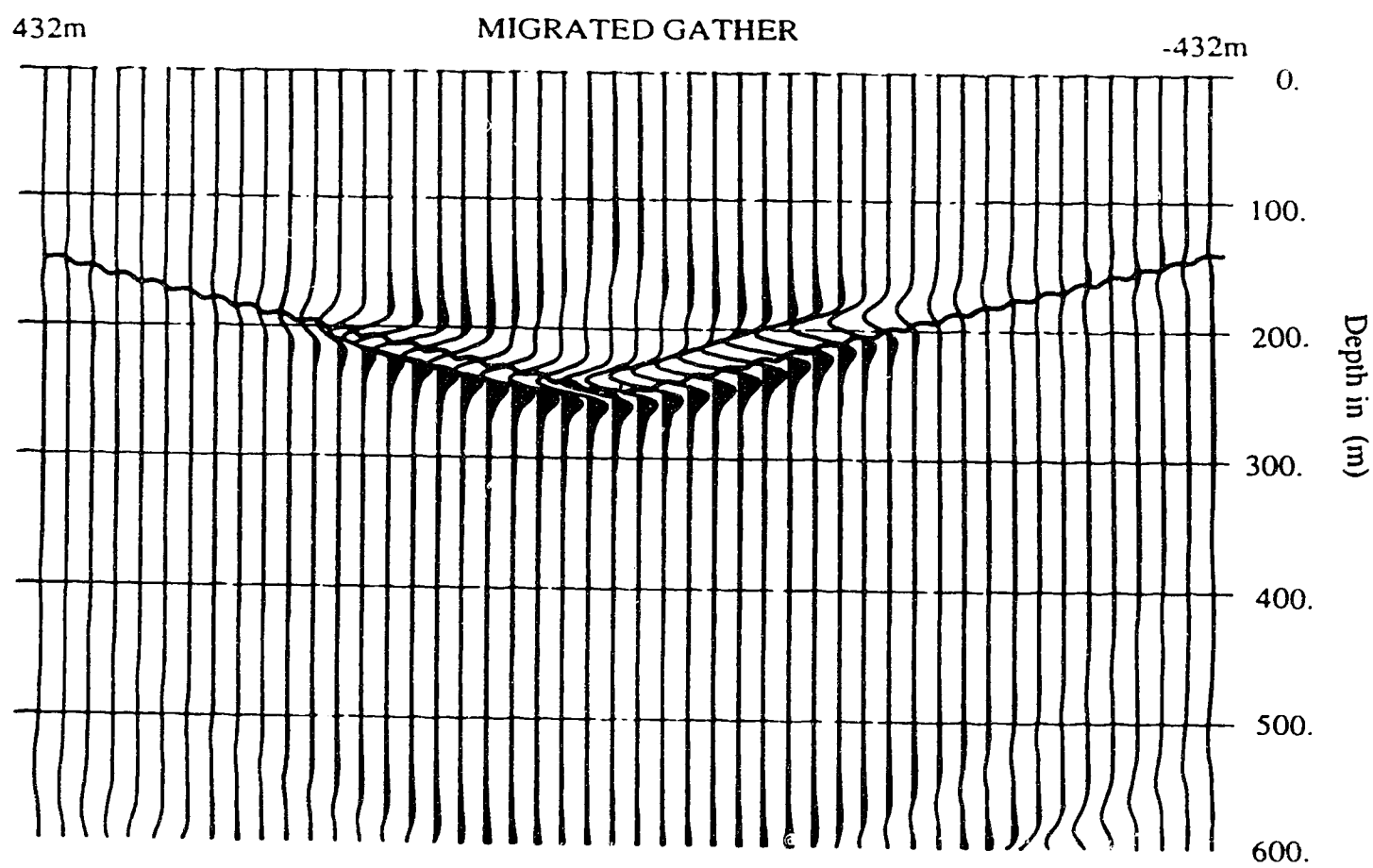


Figure 4.8

Depth migrated shot gather of the syncline model.

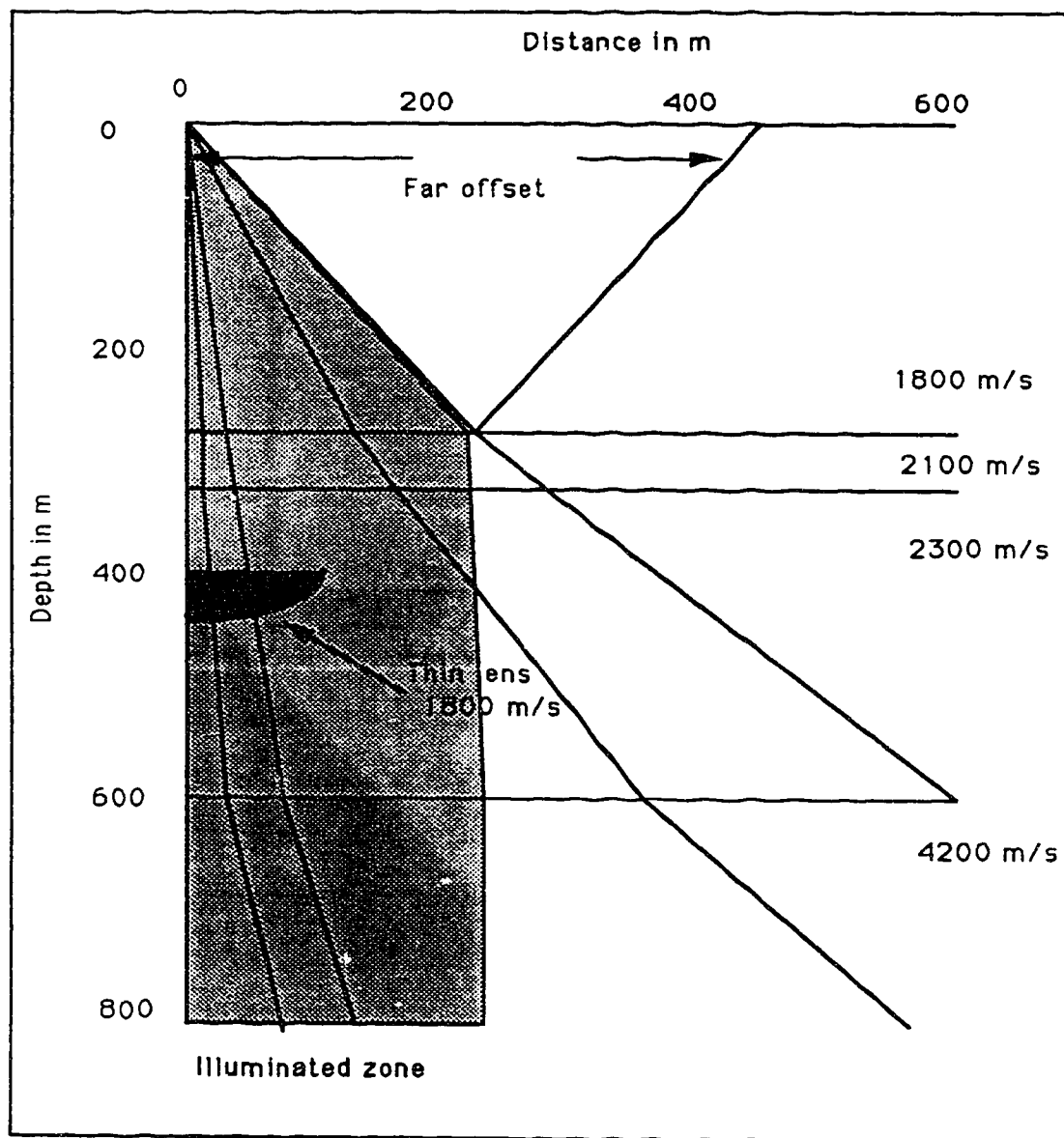


Figure 4.9 Multilayer depth model with a thin lens. Also the unperturbed ray paths are shown.



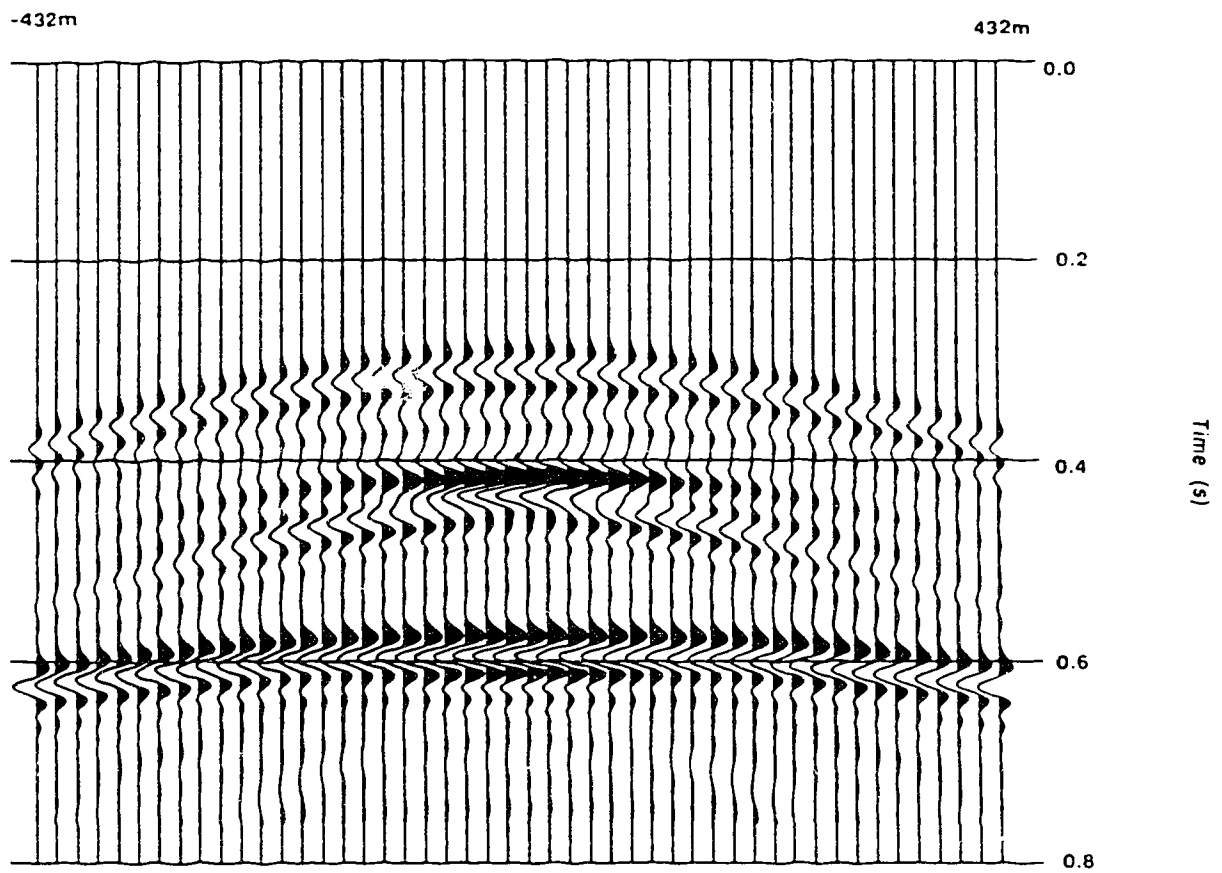


Figure 4.10 P-SV, vertical particle velocity, split spread shot gather for the multilayer model shown in Figure 4.9.

spacing. The time array was computed by a two dimensional spatial interpolation from the rays shown in Figure 4.9. Having the interpolated time array and the velocity field of the media the shot gather migration algorithm produced the section shown in Figure 4.11, employing a depth step of 4m. All the horizons were mapped at the correct spatial and depth locations and also the algorithm preserved the correct polarity as indicated in Figure 4.9 at approximately 400m.

#### **4.11 Conclusions**

A depth migration shot gather operating in the  $\omega$  -  $x$  domain was developed. The algorithm can be used for both vertical and lateral velocity varying media. A true common depth stacking after the migration of each shot gather yields a higher resolution image on the migrated depth section. Prestack migration in the shot gather domain resolves and preserves amplitude information better than the after stack migration. By performing the prestack migration in the frequency - spatial domain one can implement the present algorithm in parallel computational environments.

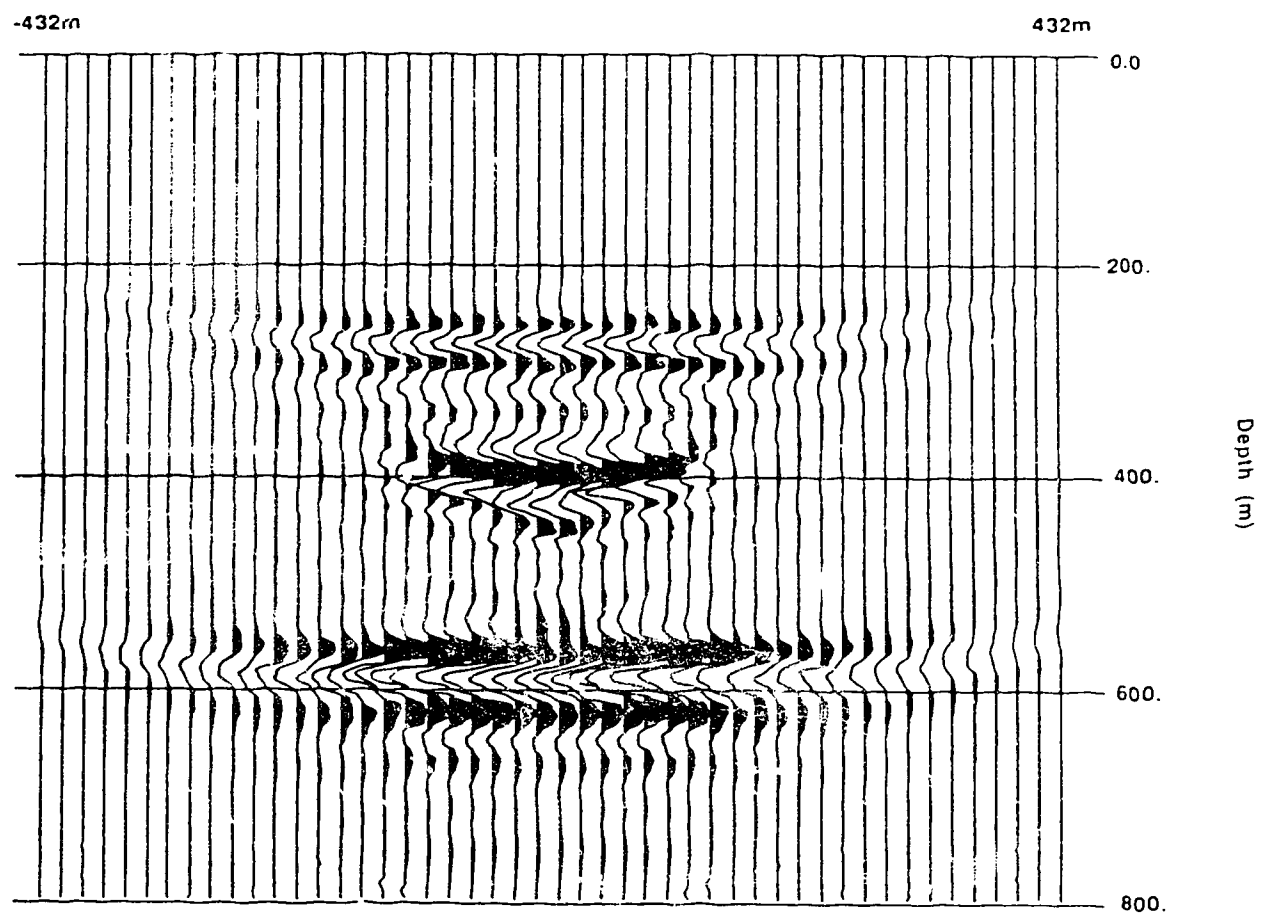


Figure 4.11 Migrated shot gather of the synthetic section shown in Figure 4.10.

## CHAPTER 5

### ANALYSIS OF SEISMIC REFLECTION DATA OVER A STEAM INJECTION SITE

#### 5.1 Introduction

In February of 1984, Esso carried out a seismic experiment over a steam injection site near Cold Lake, Alberta, in order to investigate the feasibility of mapping steam heated zones by seismic methods. The experiment consisted of three seismic lines of data centered near a steam injection well. Esso presented to the Seismology Laboratory at the University of Alberta three amplitude color coded stacked sections and copies of the field digital data. The following description summarizes the computer processes carried out in the Seismology Laboratory with innovative algorithms written by the author. After amplitude normalization to correct for various source size and receiver coupling to the ground, the data were stacked into three common midpoint (CMP) sections. A comparison of a synthetic zero offset section incorporating attenuation with Esso's and our own CMP stack sections for the area under investigation proved to be helpful in defining the discontinuous velocity changes in the area and the lateral extent of the zone affected by the steam injection operation. Post-stack  $\omega$  -  $x$  migration and an innovative pre-stack  $\omega$  -  $x$  migration followed by a normal stack were used to image the reflecting interfaces. The newly developed stacked  $\omega$  -  $x$  migration section had much better resolution than any of the current industry standard computer processing.

## 5.2 Processing of the seismic reflection lines.

Figure 5.1 depicts a plan view of the three surface seismic lines in the Esso experiment. Line 80 runs from NE to SW starting with station #1017 and ending at station #1103, covering a total distance of 1.5 km. Line 81 has a direction from E to W, starting from station # 1001 and terminating at station #1117, covering a total distance of 2.1 km. The third line 82 runs NW to SE, with station numbers ranging from #1001 to # 1061, covering a total distance of 1.1 km. All three lines intersect each other at station # 1044 on line 80, #1055 on line 81 and # 1036 on line 82. The actual steam injection surface location is situated on line 82 between stations #1032 and #1033.

Figure 5.2 illustrates the principal used to obtain a single six fold stack trace for a group of six sources and six receivers located on the surface. All the data are corrected for the hyperbolic travel time before stacking. The actual field data at Cold Lake was 24 fold (2400%) resulting in an improvement of  $\sqrt{24}$  in signal to noise ratio.

Figures 5.3 - 5.5 illustrate the CMP stack sections as processed and displayed by Esso Research, for lines 80, 81 and 82, respectively. The target reflecting horizon is situated at around 0.5 sec in all the three lines. Esso's processing sequence did not preserve the relative amplitude information for the seismic data. The field acquisition geometry was a split spread shot gather consisting of 48 receiver channels each, with 18m station separation. The energy source used was 0.3 kg of dynamite at an average depth of 9m. The shot interval was 36m resulting in a maximum stacking fold of 2400%. The nearest offset trace in a shot gather was at 18m and the farthest offset was at 432m.

The field data is recorded in a multiplex format consisting of 48 channels in each

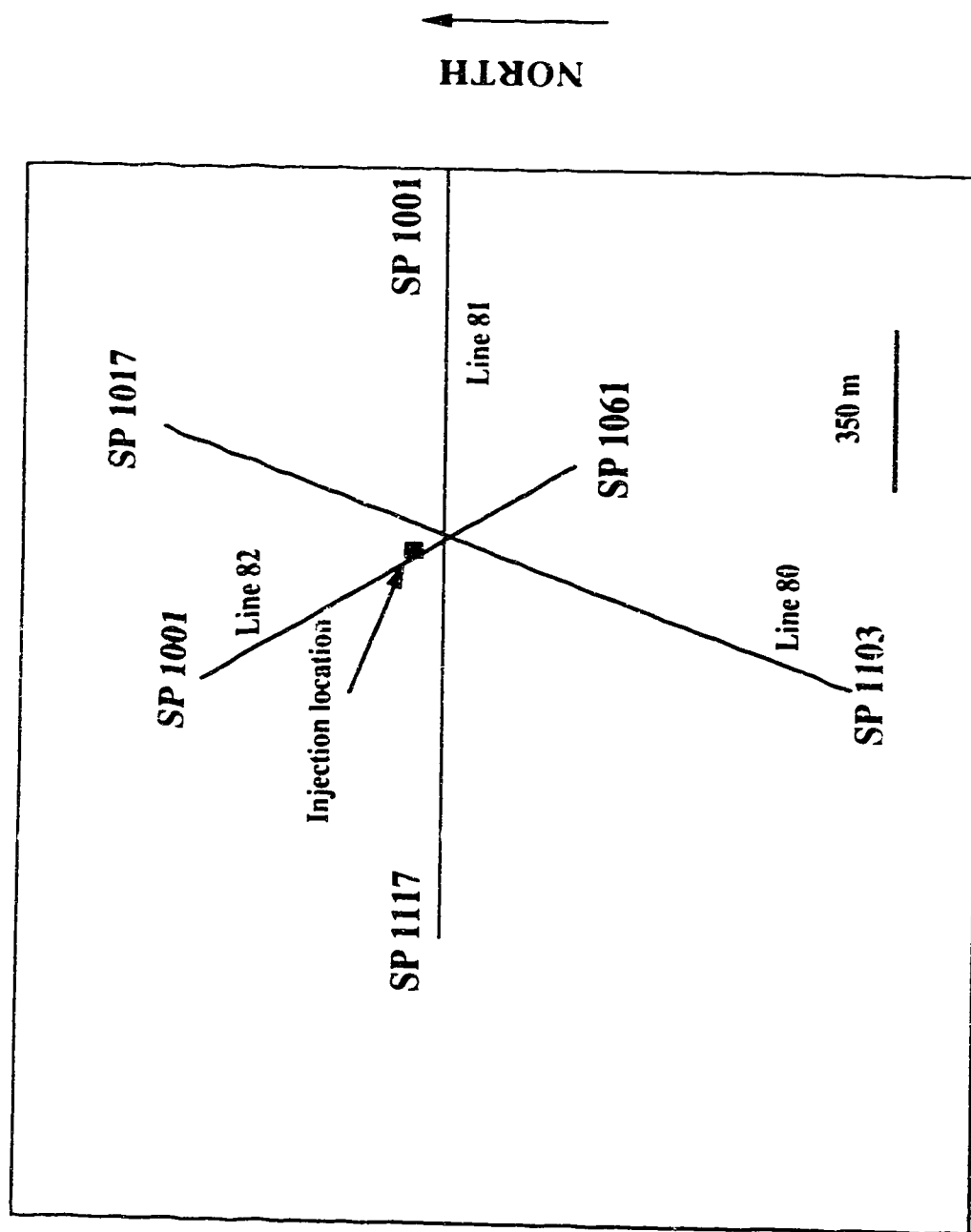


Figure 5.1 Acquisition geometry of Esso's 1984 seismic experiment at Cold Lake.  
(The locations of the stean injection well is also shown)

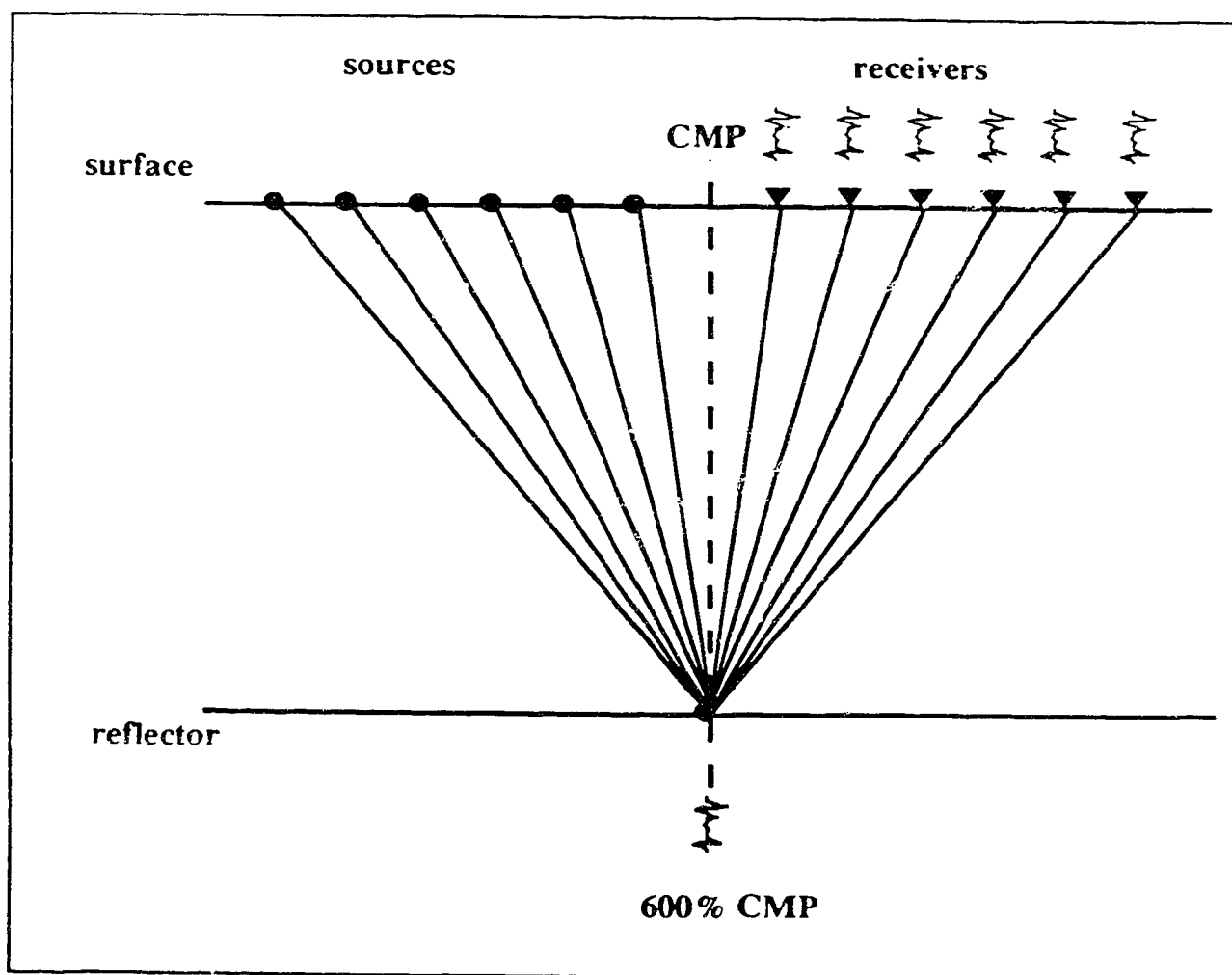


Figure 5.2 Schematic representation of a Common Midpoint (CMP) Gather.

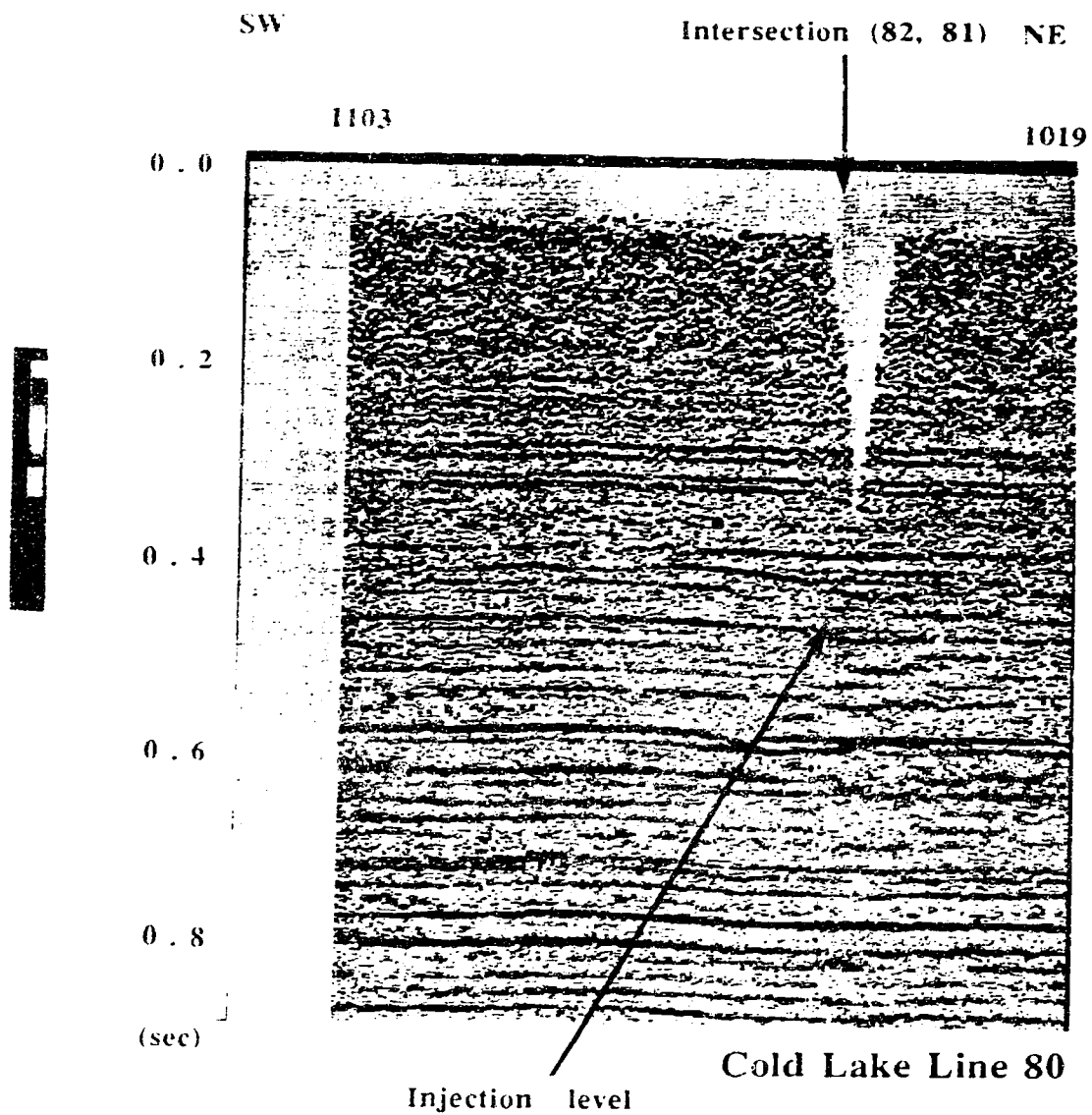


Figure 5.3 Esso's common midpoint stack section for line 80.  
(Arrow indicates the steam injection level)



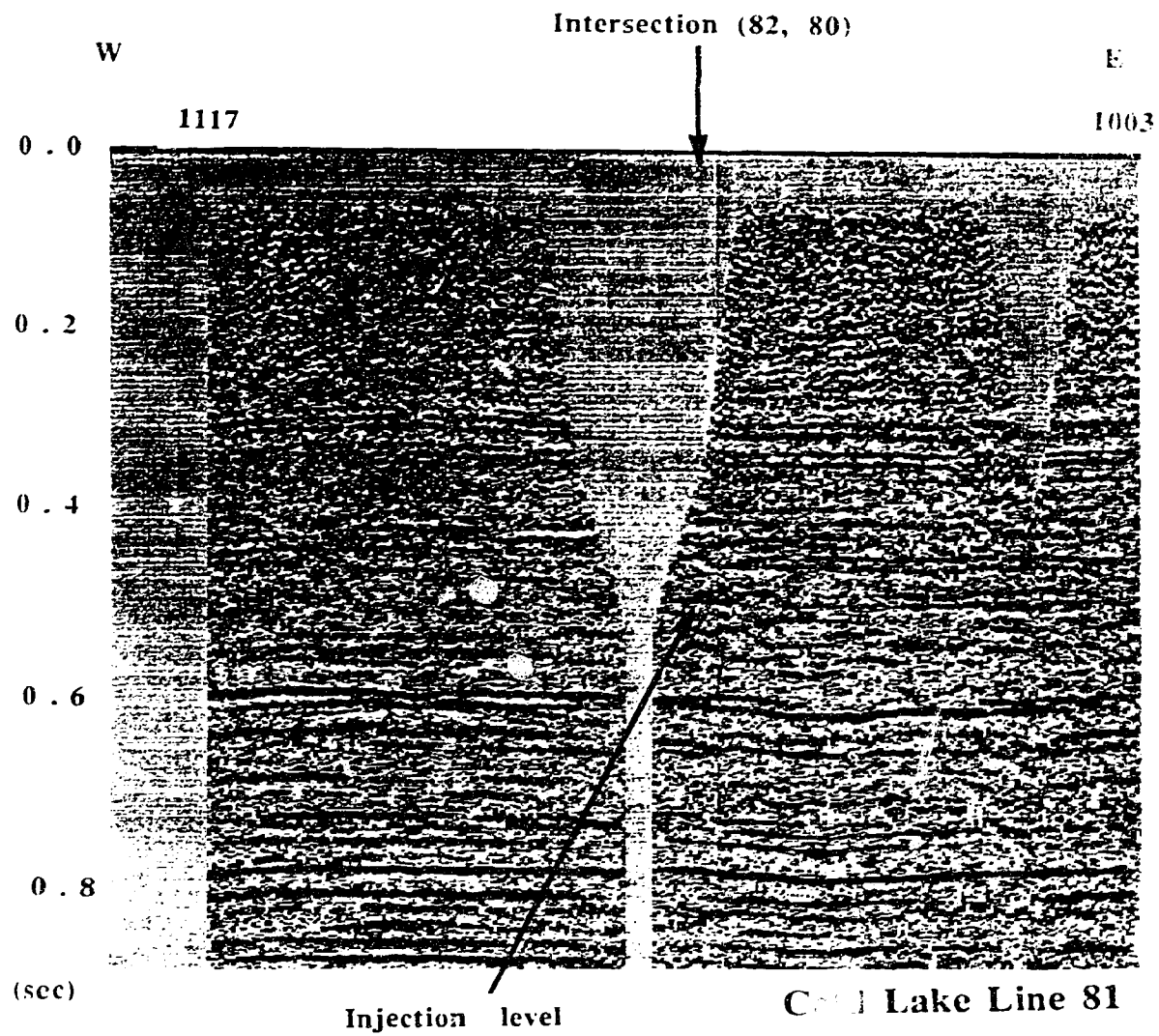


Figure 5.4 Esso's common midpoint stack section for line 81.  
(Arrow indicates the steam injection level)

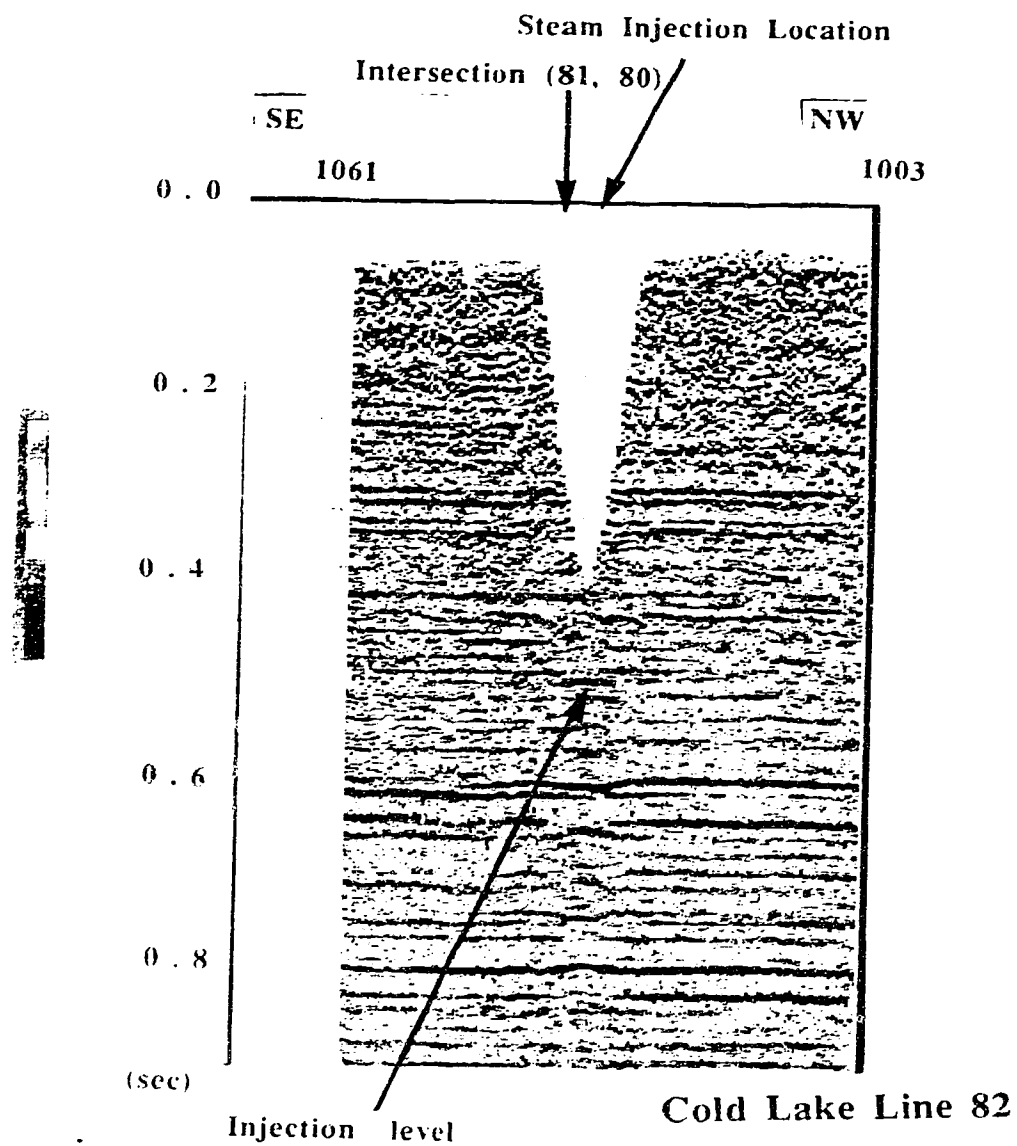


Figure 5.5 Esso's common midpoint stack section for line 82.  
 (Arrow indicates the steam injection level)

time step. The digital format includes 16 bits of amplitude information and 4 bits of amplitude gain information. The gain varies with each channel at each time step. At the University of Alberta the following steps are applied to the raw field data. Demultiplexing was carried out to separate the channels and the true amplitude was recovered. The processing steps applied under the idea that the less done to the data the better:

1. A linear mute applied to cancel the high amplitude horizontally travelling elastic waves (first breaks);
2. The application of the inverse of the exponential gain function, shown in Figure 5.6, calculated on the basis that the energy of the wavefront decreases as it travels at large distances. Hence, this very simple function attempts to compensate for large amplitude variations due to physical attenuation, spherical divergence, scattering at interfaces etc... Various shot gathers were selected and from these records the amplitude decay of different traces within various time windows were analysed. The inverse of an average exponential decay function was computed and applied to all shot records for all three lines.
3. Next, the receiver and shot surface consistent statics, provided by Esso were applied to all shots and receiver locations. These surface statics are necessary for the compensation of time shifts due to weathered low velocity surface layer. Esso also applied residual statics to enhance the continuity of reflecting horizons.
4. A global trace balancing was applied to all shot records and was computed as follows:  
From one shot gather a time window from 0.8 sec to 1.0 sec was selected and the mean of the amplitudes squared was computed for all 48 traces in the gather resulting in a global factor. The reason for the selection of the 0.8 to 1.0 sec time window is that within this interval the reflections are consistent and continuous and it is well below the targeted zone in the Clearwater Formation which occurs at 0.5 sec. One could also use a band of reflectors above the Clearwater but the reflection quality in the upper section is more variable. Then for each shot gather and each trace, the sum of amplitudes squared within

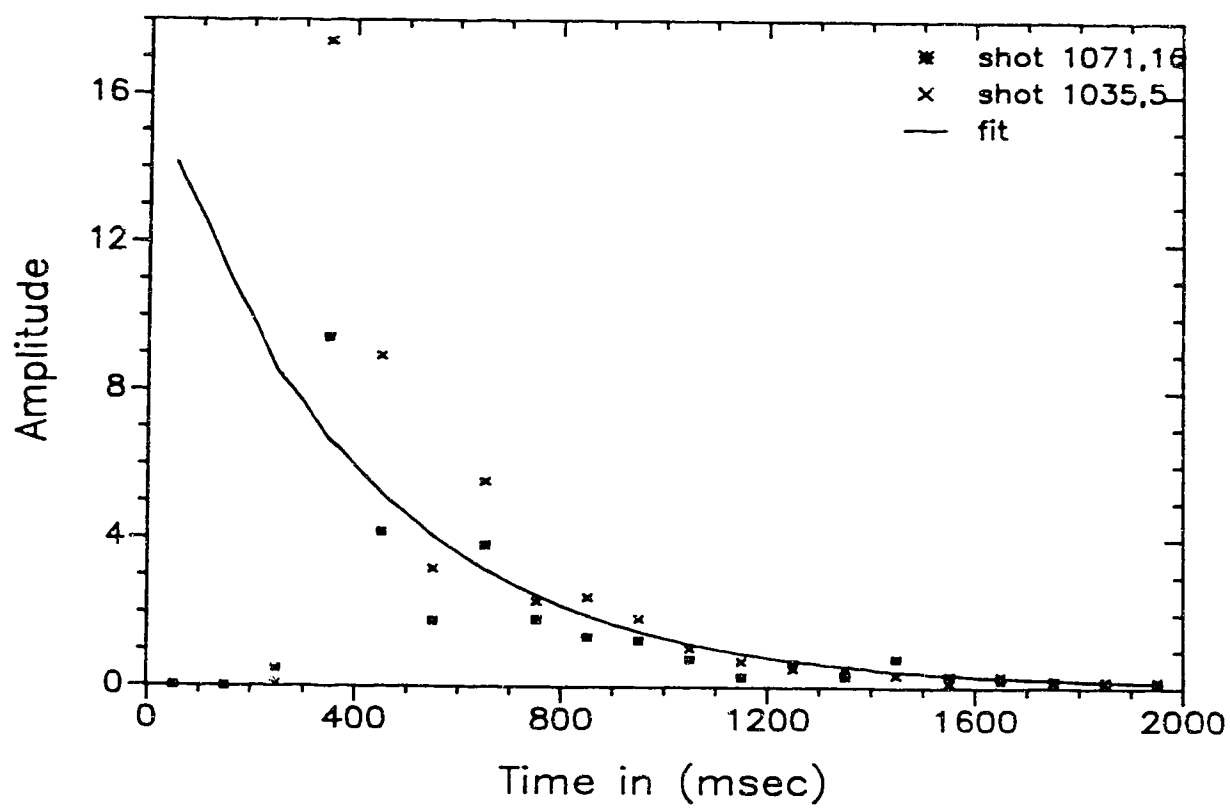


Figure 5.6 Amplitude decay function calculated for different traces in various shots.

the same time window (0.8 to 1.0 sec), was computed resulting in a trace factor. The ratio between the global factor to the trace factor was applied to each trace to all shots for all the three lines. Consequently, all the source records for all three lines have been normalized to a uniform amplitude energy.

5. The following processing step was a common midpoint (CMP) sorting operation. According to this sorting procedure the amplitude corrected shot gather records are transformed into trace gathers which have a common midpoint (half the source - receiver distance) for various offsets. The CMP gather is one of the most important coordinate transformations revealing direct information about impedance (velocity times density) contrasts due to change in geological stratigraphy if the dips are less than about  $20^\circ$  of the various geological formations encountered.

6. A normal moveout (NMO) was applied to each CMP gather, according to rms velocity values for the area under investigation. The interval velocities derived from the rms velocities were checked against sonic velocities obtain from a nearby logged well. This dynamic correction is a necessary operation in the seismic data processing stream because it removes the effect of offset dependence.

7. A normalized summation of all the traces found in the same CMP gather produces a stacked trace. A CMP stack section is a series of such stacked traces. Figures 5.7 to 5.9 illustrate the three CMP stack sections corresponding to lines 80, 81 and 82, respectively.

No pre or poststack deconvolution was applied to the data, since the deconvolution operator affects the reflection amplitudes of the data. Consequently, our stack sections are dominated by relatively low frequency. Figure 5.10, illustrates the power spectrum for the 400 - 600 ms time window of CMP #1032 for line 82. Clearly the dominant frequency shown is around 23 Hz. Also, no trim or residual statics were applied to our processing sequence since we are trying to preserve small time delays in the data caused by

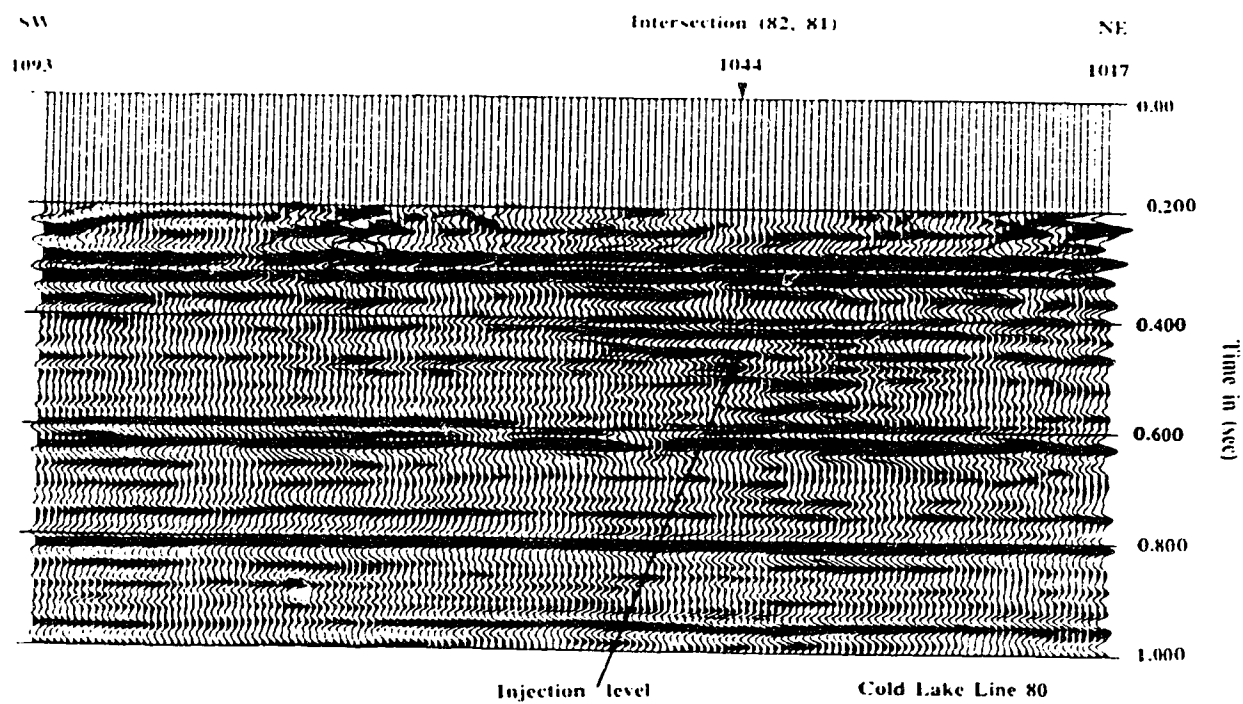


Figure 5.7 Common midpoint stack section for line 80.  
 (Relative amplitude processed, arrow indicates the steam injection level)

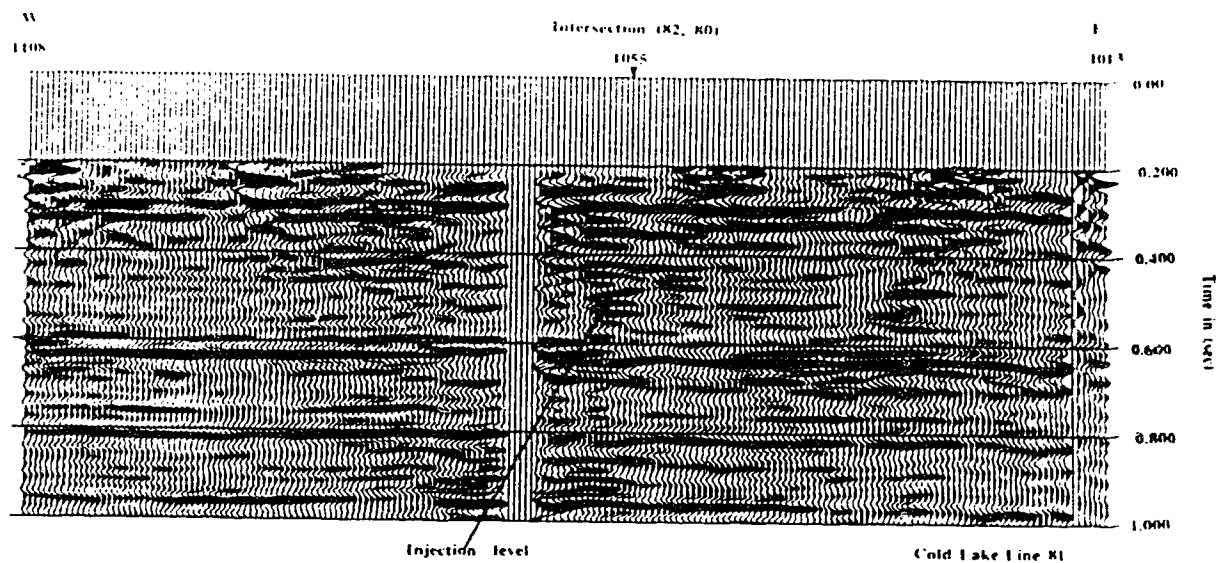


Figure 5.8 Common midpoint stack section for line 81.  
(Relative amplitude processed, arrow indicates the steam injection level)

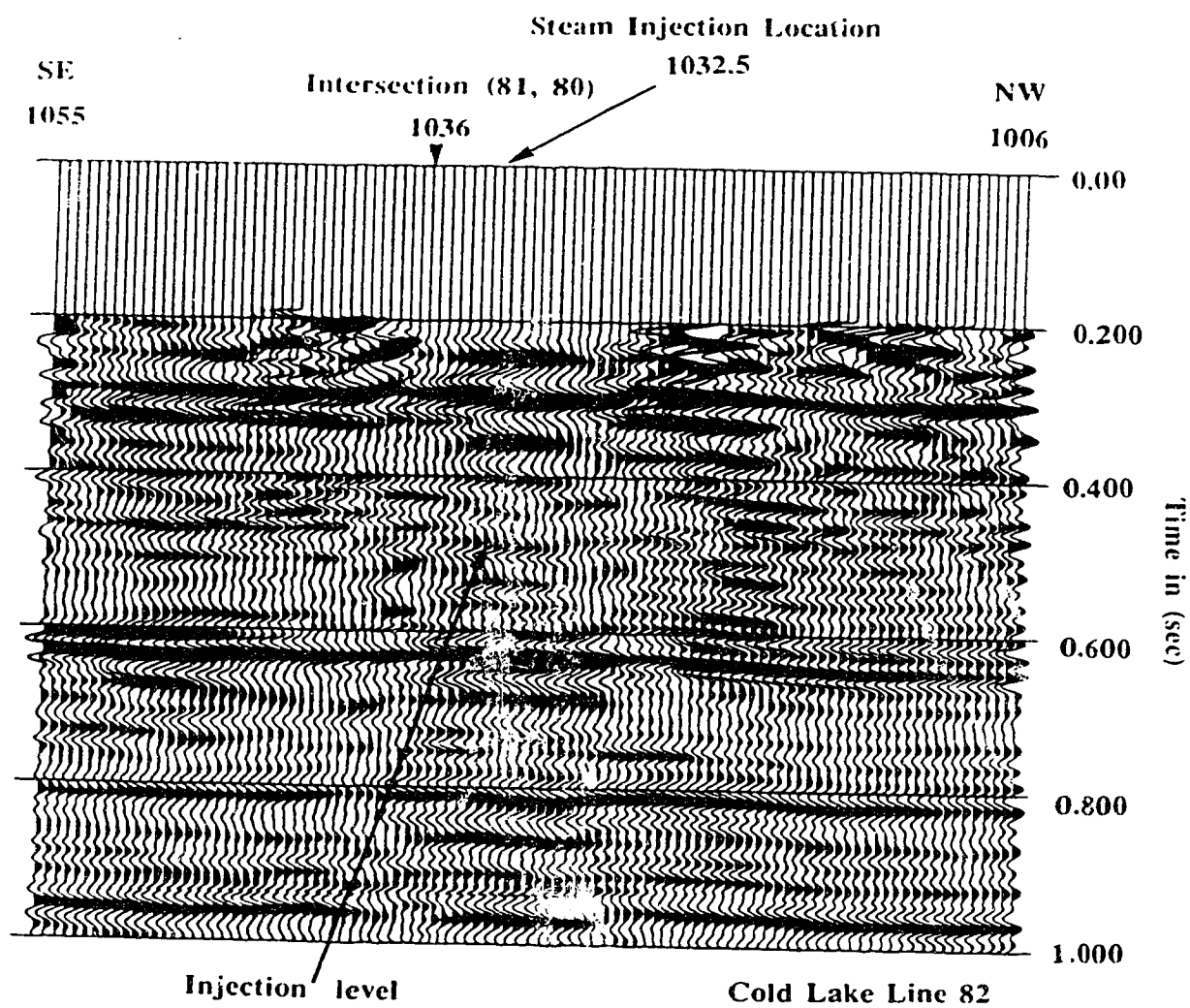


Figure 5.9 Common midpoint stack section for line 82.  
 (Relative amplitude processed, arrow indicates the steam injection level)



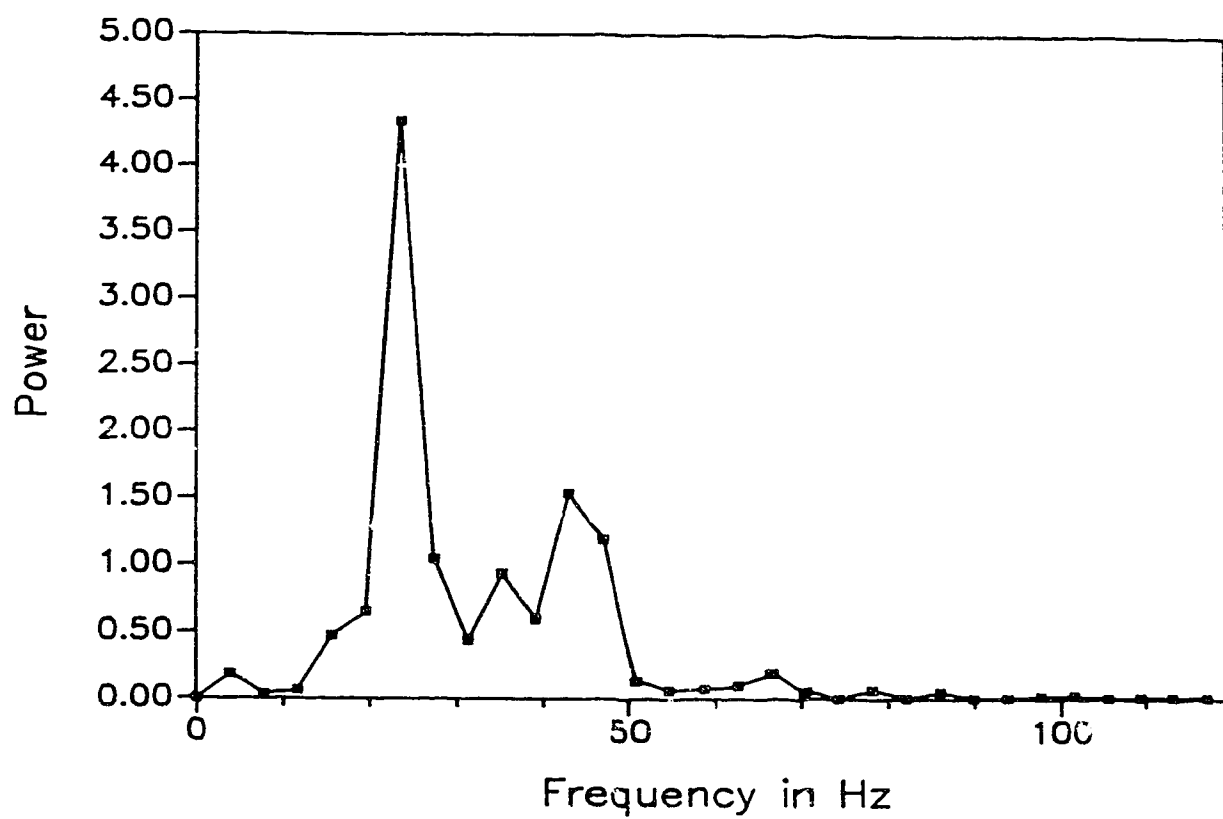


Figure 5.10 Power spectrum for CMP #1032, line 82.  
(Computed for the time interval between 400 ms - 600 ms)

the low velocity zone. For these reasons there are considerable differences in the appearance of our stacked sections from the ones processed by Esso. In principle a deconvolved section emphasizes more the higher frequencies and therefore has greater resolution. In practice the deconvolution procedure can introduce artifacts and will amplify high frequency noise. Therefore one needs a noise free data set which is difficult to obtain at Cold Lake where there is a great amount of industrial noise. At this stage of analysis we have chosen to avoid deconvolution (although Esso sections have it). It may be more advantageous to correct the original field data for the effect of natural attenuation ( $Q$ ) now that there are some estimates on this parameter for the area.

### **5.3 Zero offset modeling with the Exploding Reflector Model (ERM) including attenuation**

Forward modeling of zero offset stack data can be very useful in any stage of interpretation (Kalamis and Kjartansson, 1985; May and Hron, 1978; Kosloff and Baysal, 1983). Synthetic data are compared to field data and an estimate of the agreement between calculations and observations is directly obtained. A common midpoint (CMP) section may be regarded as data obtained from coincident source and receivers. In this zero offset model, the energy travel path from source to reflector is identical to that from reflector to receiver. The assumption is that all sources activated simultaneously, but each receiver records signals originating from the same source - receiver point. Such zero offset data do not correspond to any wavefield resulting from a simple experiment. As a result it is helpful to create a hypothetical physical experiment to provide an intuitive picture of zero offset sections. Such an experiment is known as the Exploding Reflector Model, (ERM; Lowenthal et al, 1976) where the energy sources are not at the surface, but they are distributed along the reflecting surfaces. In other words, the reflectors are represented by buried sources, which are *exploded* at the same time  $t=0$ . Therefore one needs to be

concerned only with upward traveling waves. Since the CMP record sections are always displayed in two-way travel time, one has to use half the velocity of the wave propagation to compensate for the one-way travel time.

In summary, modeling a zero-offset section using the principle of ERM one can start with a blank upgoing wavefield below the lowest reflector of interest, and use the wave equation or an approximation such as equation (4.10) with half the medium velocities, to continue the wavefield up towards the surface. Since a delta function at  $t=0$  has a Fourier transform that is simply a constant independent of frequency, one can model the exploding reflectors by adding the reflection coefficients to all of the frequencies at each depth step. The time section is then obtained by inversely Fourier transforming the results at the surface.

#### **5.4 Results incorporating a constant $Q$**

The fact that amplitude dependence of the propagation velocity and  $Q$  the attenuation factor, at strains less than  $10^{-6}$  has not been observed, strongly suggests that at these strains the material response is dominated by linear effects.

Kjartansson (1979), presented a linear model for attenuation of waves where  $Q$ , i.e., the portion of energy lost during each cycle or wavelength is independent of frequency. Frequency independent  $Q$  implies that the loss per cycle is independent of the time scale of oscillations at least for seismic reflection prospecting. In Chapter 6 some more discussion on  $Q$  is outlined. The constant  $Q$  model is mathematically much simpler than any of the nearly constant  $Q$  models, such as presented by Azimi et al (1968), Lomnitz (1957), Futterman (1962). Most of the nearly constant  $Q$  models have restricted their analysis to cases where  $Q$  is large, typically  $Q > 30$ . In contrast, the simplicity of the constant  $Q$  description allows the derivation of exact analytical expressions for the various frequency domain properties such as complex modulus phase velocity and the attenuation coefficient,

that are valid over any range of frequencies and for any positive value of  $Q$ .

Kjartansson (1979), used as a creep function a relation which plots as a straight line in a log-log plot given by the formula for  $t > 0$ :

$$\psi(t) = \frac{1}{M_0 \Gamma(1 + 2\gamma)} \left(\frac{t}{t_0}\right)^{2\gamma} \quad (5.1)$$

where  $\Gamma$  is the gamma function,  $t_0$  is an arbitrary reference time introduced so that  $t$  has the dimension of time, and  $M_0$  will have the dimension of modulus. Since the time derivative of the creep function can be thought as representing the compliance function for the case where strain results from a unit step stress excitation function, taking the time derivative of the equation (5.1) (Kjartansson, 1979), we have for  $t > 0$ :

$$s(t) = \frac{2\gamma}{M_0 \Gamma(1 + 2\gamma)} \left(\frac{t}{t_0}\right)^{2\gamma} \frac{1}{t} \quad (5.2)$$

Taking the Fourier transform of (5.2) and since the Fourier transform of the modulus  $M(\omega)$  is equal to  $M(\omega) = 1/S(\omega)$ , solving equation (5.2) in terms of the modulus we have:

$$M(\omega) = M_0 \left(\frac{i\omega}{\omega_0}\right)^{2\gamma} = M_0 \left|\frac{\omega}{\omega_0}\right|^{2\gamma} e^{i\pi\gamma \operatorname{sgn}(\omega)} \quad (5.3)$$

where  $\operatorname{sgn}(\omega) = +1$  for  $\omega > 0$  and  $\operatorname{sgn}(\omega) = -1$  for  $\omega < 0$  and  $\omega_0 = 1/t_0$ .

From the definition of  $Q$  which is related to the phase angle between stress and strain (Aki and Richards, 1980), or equivalently as the ratio of the imaginary part to the real part of the modulus  $M(\omega)$ , from equation (5.3) we have:

$$\frac{1}{Q} = \frac{\operatorname{Im}(M(\omega))}{\operatorname{Re}(M(\omega))} = \frac{\sin(\pi\gamma)}{\cos(\pi\gamma)} = \tan(\pi\gamma)$$

or

$$\gamma = \frac{1}{\pi} \tan^{-1}\left(\frac{1}{Q}\right) \quad (5.4)$$

To model the propagation of the waves in the constant  $Q$  media, using the 45<sup>0</sup> paraxial approximation to the wave equation given by equation (4.10) described in Chapter 4 one has to replace the  $m(x,z) = \omega/v(x,z)$  where now  $v(x,z)$  is given by:

$$v = \sqrt{\frac{M(\omega)}{\rho}} = \sqrt{\frac{M_0(\omega)}{\rho}} \left| \frac{\omega}{\omega_0} \right|^\gamma e^{i\pi\gamma/2}$$

with

$$m(x,z) = \frac{\omega^{1-\gamma}}{v_0(x,z)} e^{-i\pi\gamma/2} \quad (5.5)$$

Therefore, the plane wave propagation in Kjartansson's frequency independent  $Q$  is completely specified by two parameters  $Q(x,z)$ , and the reference velocity  $v_0(x,z)$  at a reference frequency. In our examples the reference frequency  $\omega_0$  used was 1Hz.

The modified  $\omega$ -x 45<sup>0</sup> paraxial approximation to the scalar wave equation, described in Chapter 4, (equation 4.10) can be used to predict the wave field  $P(x,z=0,t)$  on the surface given the velocity distribution of the subsurface. This algorithm essentially can be run in the reverse direction (from the bottom up) and thus can be used to model a zero offset section according to Exploding Reflector Model (ERM). Given the reflectivity function at each interface and the interval phase velocities, each harmonic is extrapolated upwards throughout the depth model. Attenuation can be incorporated by adjusting the variable coefficient  $m(x,z)$  in equation (4.10) according to equation (5.5). The only concern is to use half the values of the interval velocities since we simulate an exploding reflector experiment. Since we are using the same equation (equation 4.10) as we did for the migration, and under the spirit that migration is the reverse of modeling one has to reverse the sign of the velocity values.

Figure 5.11 illustrates the depth velocity model employed in the  $\omega$  -  $x$  zero offset modeling algorithm together with the assigned geological formations. In this model the  $Q$  in the steam heated zone was equal to 8, where the  $Q$  in the surrounding upper crustal rocks was equal to a value of 30 (Macrides, 1987). Figure 5.12 depicts the zero offset synthetic section employing the above  $Q$  values. The trace spacing was 9m, the depth step employed was 5m and the sampling rate was 4ms. The relative amplitude processed common midpoint stack section for line 82 is shown in Figure 5.13. Comparing Figures 5.12 and 5.13, a reasonable agreement is illustrated concerning the lateral extent and the arrival time of the seismic anomaly due to the steam heated zone. The diffractions appearing on the synthetic section (Figure 5.12) do not appear in the real CMP stack section (Figure 5.13). This indicates that the lateral velocity changes are smoother than we anticipated. Also the variations shown in the real CMP stack section (Figure 5.13) can be attributed to geologic structure of the Paleozoic unconformity and to the various inhomogeneities such as gas pockets found in the Upper - Lower Grand Rapids and in the McMurray formations. It cannot be overlooked that there are many quasi-continuous and slightly dipping reflecting beds on the field sections which have not been imaged by our generalized model. This thesis has concentrated on the methods for injection imaging and has not dealt with minor velocities and structural anomalies. They are important but are more properly dealt within an exploration department in a commercial research laboratory.

### 5.5 Pre stack $\omega$ - $x$ depth migration

The depth migration algorithm described in Chapter 4 was employed to migrate seismic line 82 (Figure 5.9). Care must be taken to use the appropriate imaging condition for the post-stack depth migration and also to employ half the medium's velocities

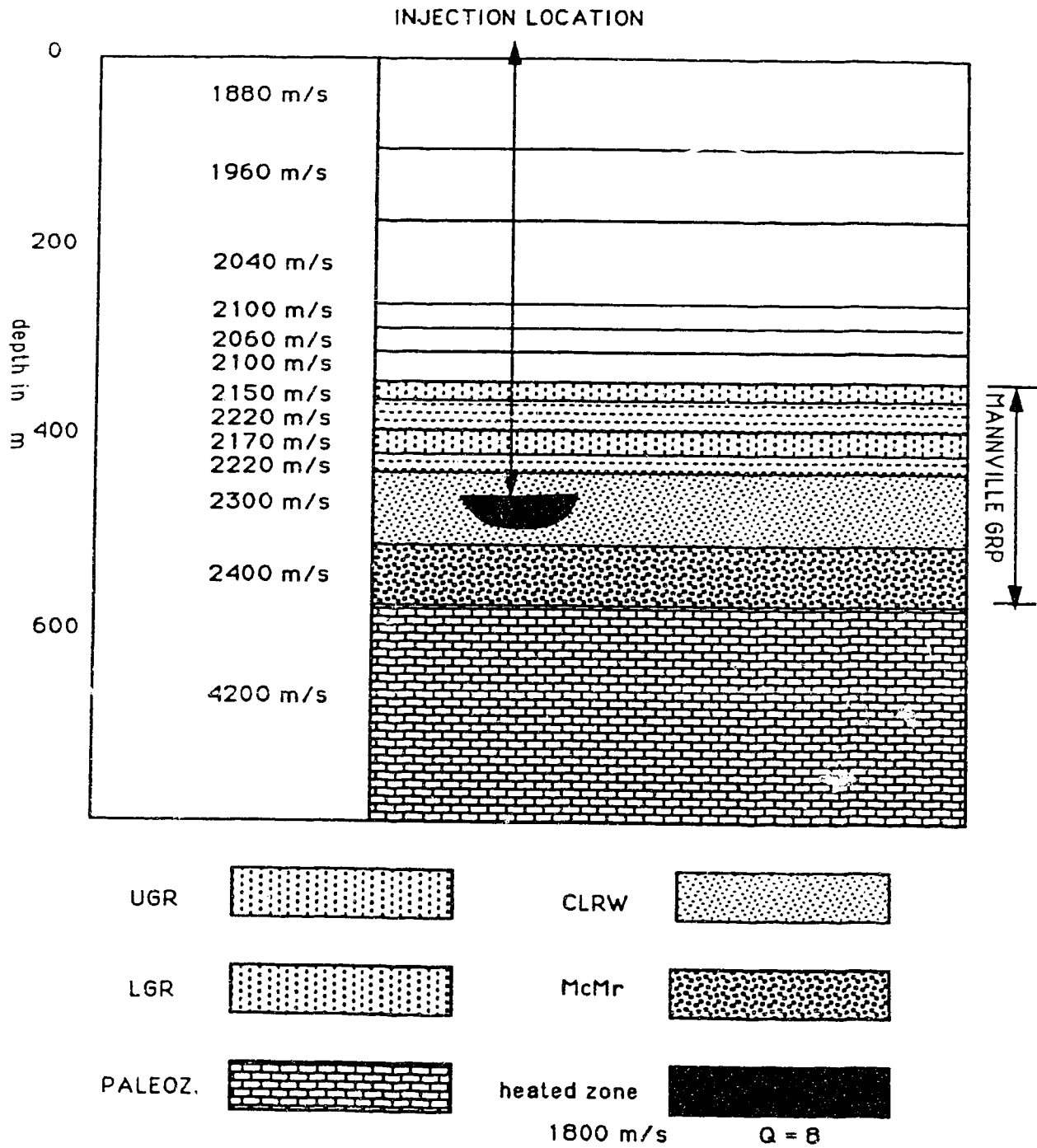


Figure 5.11 Depth model used for the zero offset modeling.  
(Q=8 in the steam and Q=30 in the background)

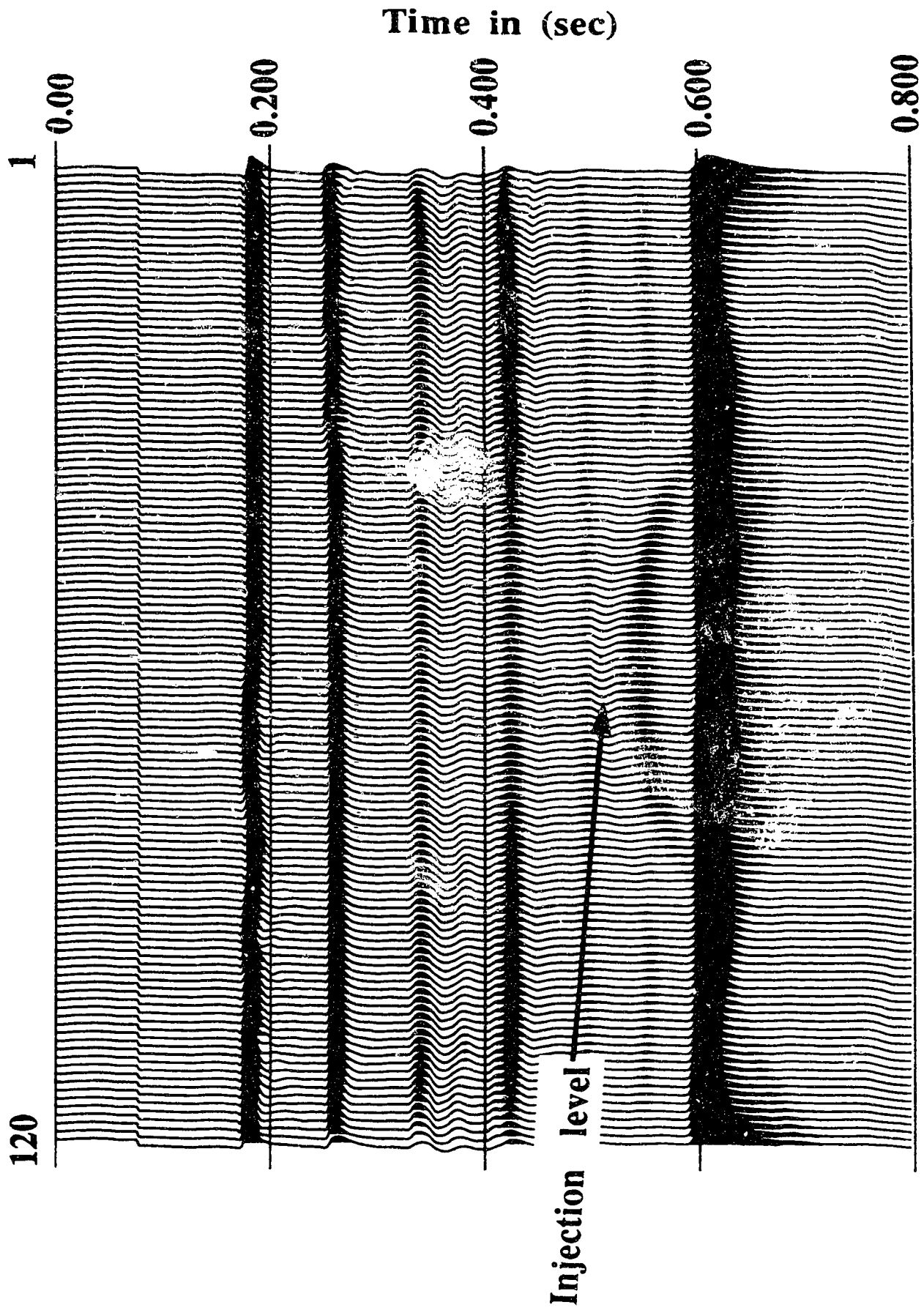


Figure 5.12 Zero offset synthetic section employing the depth model shown in Figure 5.11.



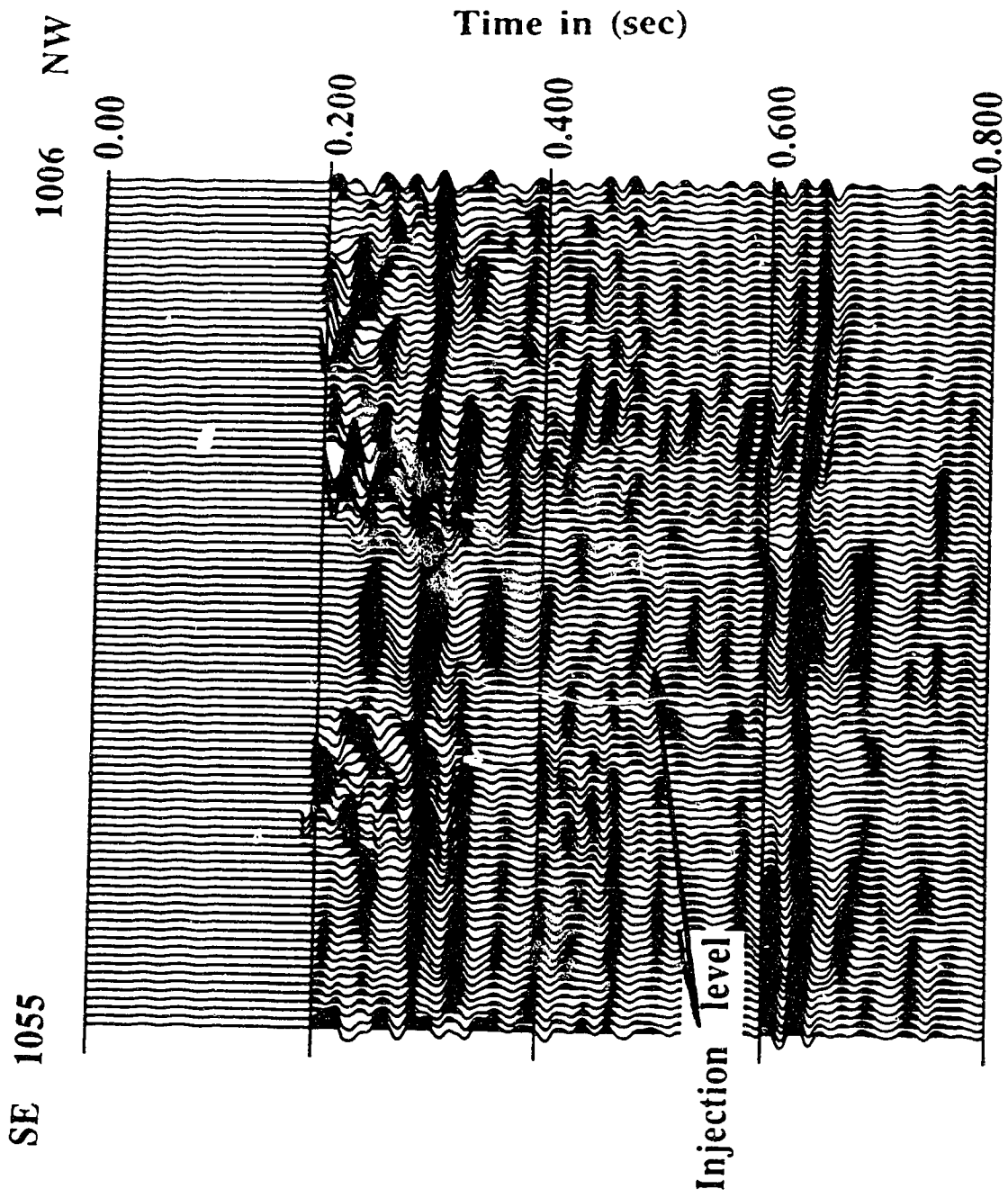


Figure 5.13 Common midpoint stack section for line 82.  
(Same as Fig. 5.9 but with different horizontal and vertical scales)

according to the ERM assumption. For the pre-stack depth migration the field shot gathers were corrected for geometrical spreading and for surface statics due to the weathered layer which includes glacial drift. An amplitude balancing factor was applied to all shot gathers to accommodate variable source energy.

Figure 5.14, depicts the first 0.7 sec of one of the split spread shot gathers consisting of 48 traces. Figure 5.15, illustrates the velocity - depth model used to compute the direct time arrivals for the time shifts to be employed during the imaging step in the pre-stack depth migration. Esso provided us with the information regarding the location of the steam injection and the depth where the steam has been injected which is around 450m. Figure 5.16, illustrates an after stack depth migrated section of the stack section shown in Figure 5.9, employing  $\omega$  -  $x$  migration (in the zero offset mode) algorithm (equation 4.10 - 4.11), using half the medium velocities and  $t_d(x,z)=0$  as the imaging condition according to ERM. Comparing the after stack depth migration in Fig. 5.16 to the originally unmigrated stack time section in Fig. 5.9 (page 78) one sees little difference. The top of the Paleozoic at 600m or 0.6s is discontinuous in both sections.

To obtain a better image of the subsurface it was decided to use migration before stacking the seismic data. We have taken the  $\omega$ - $x$  migration method developed in the previous chapter and obtained a new type of stacking section.

Figure 5.17, illustrates the migrated shot gather shown in Figure 5.14, after a spatial muting in order to keep the depth points which were illuminated by the respective shot. Performing the same operation for various shot gathers a series of migrated spatially muted shot records were obtained. A true depth point stack was followed according to equation (4.12) and the result is depicted in Figure 5.18 as a migrated  $\omega$ - $x$  stacked (MOXS) section. In both, pre and post stack depth migration operations a depth step of 4m was used to extrapolate the reflected upgoing wavefield downwards.

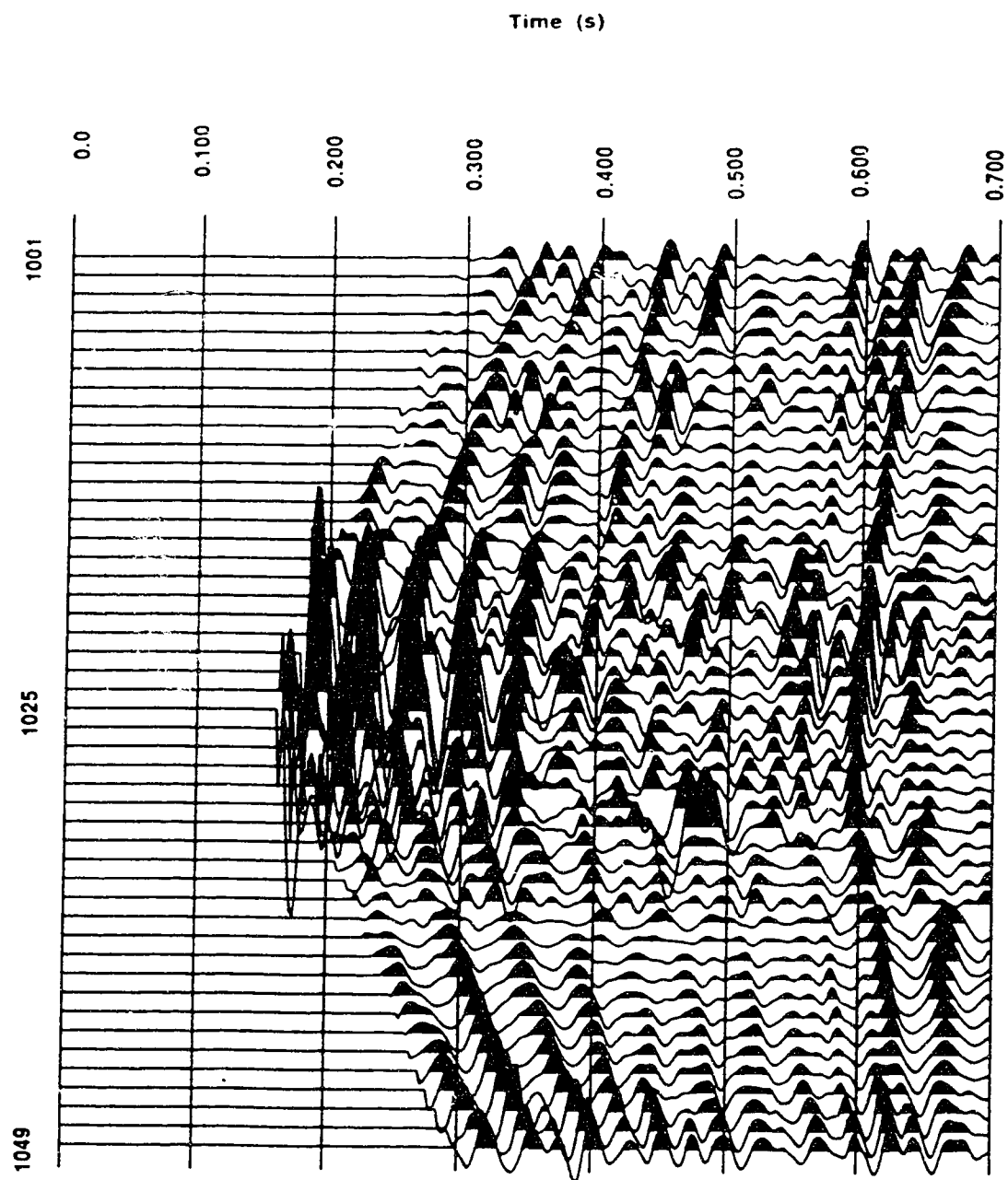


Figure 5.14 Shot gather # 1025 of line 82.

(First break muting, Surface statics, geometrical spreading, and trace balancing have been applied)

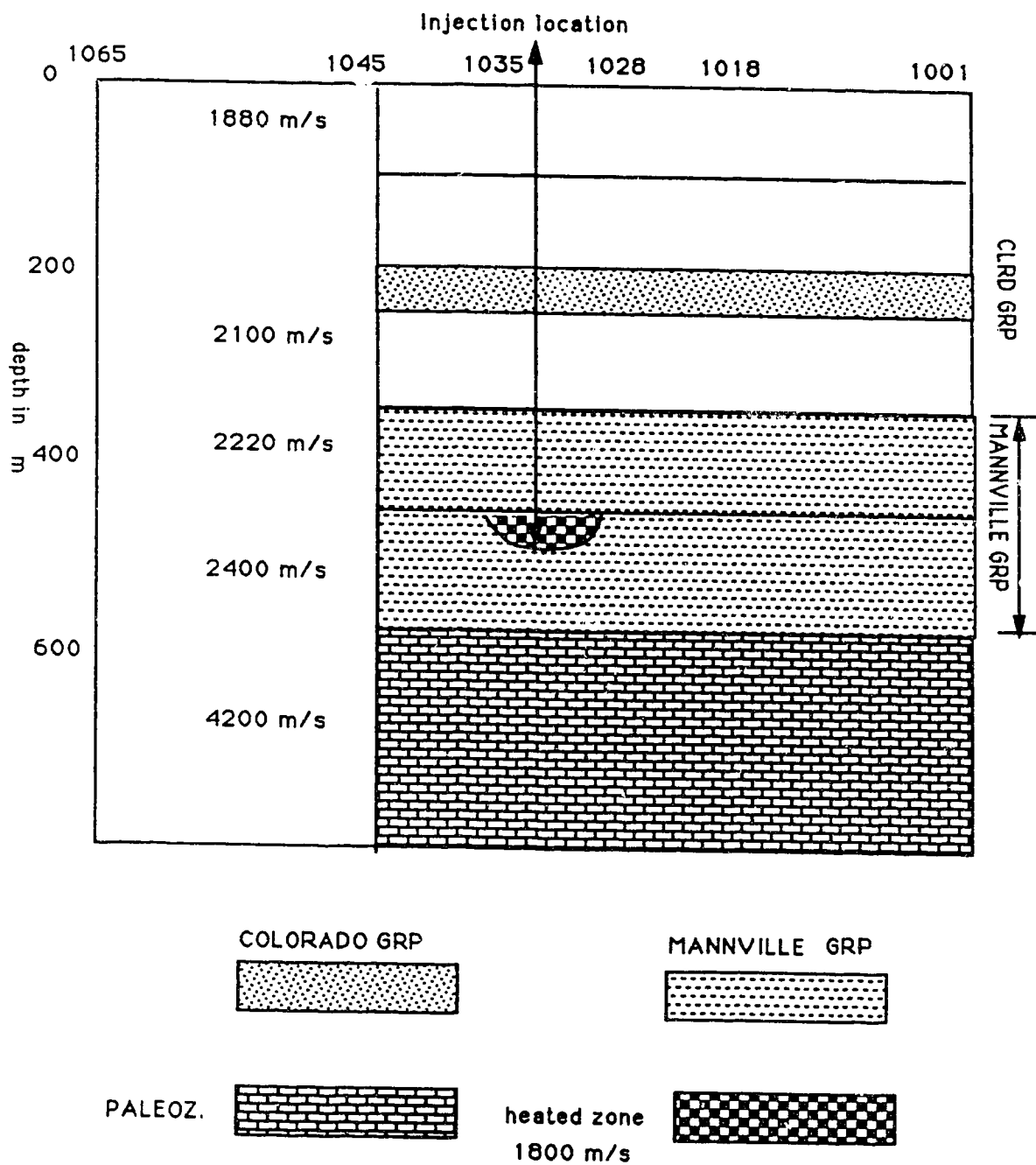


Figure 5.15 Velocity - depth model employed during the post-stack and pre-stack migrations.

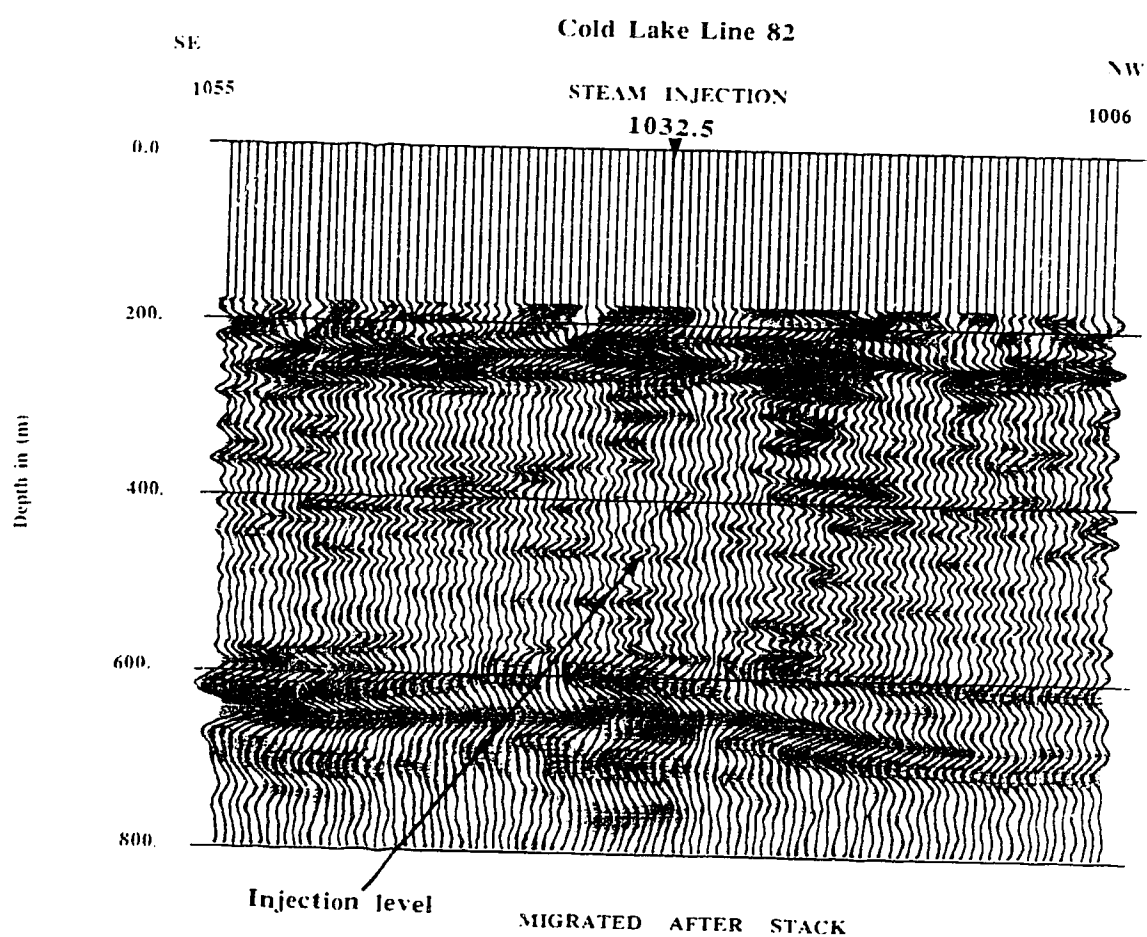


Figure 5.16 After stack depth migrated section for line 82  
(arrow indicates the steam injection level)

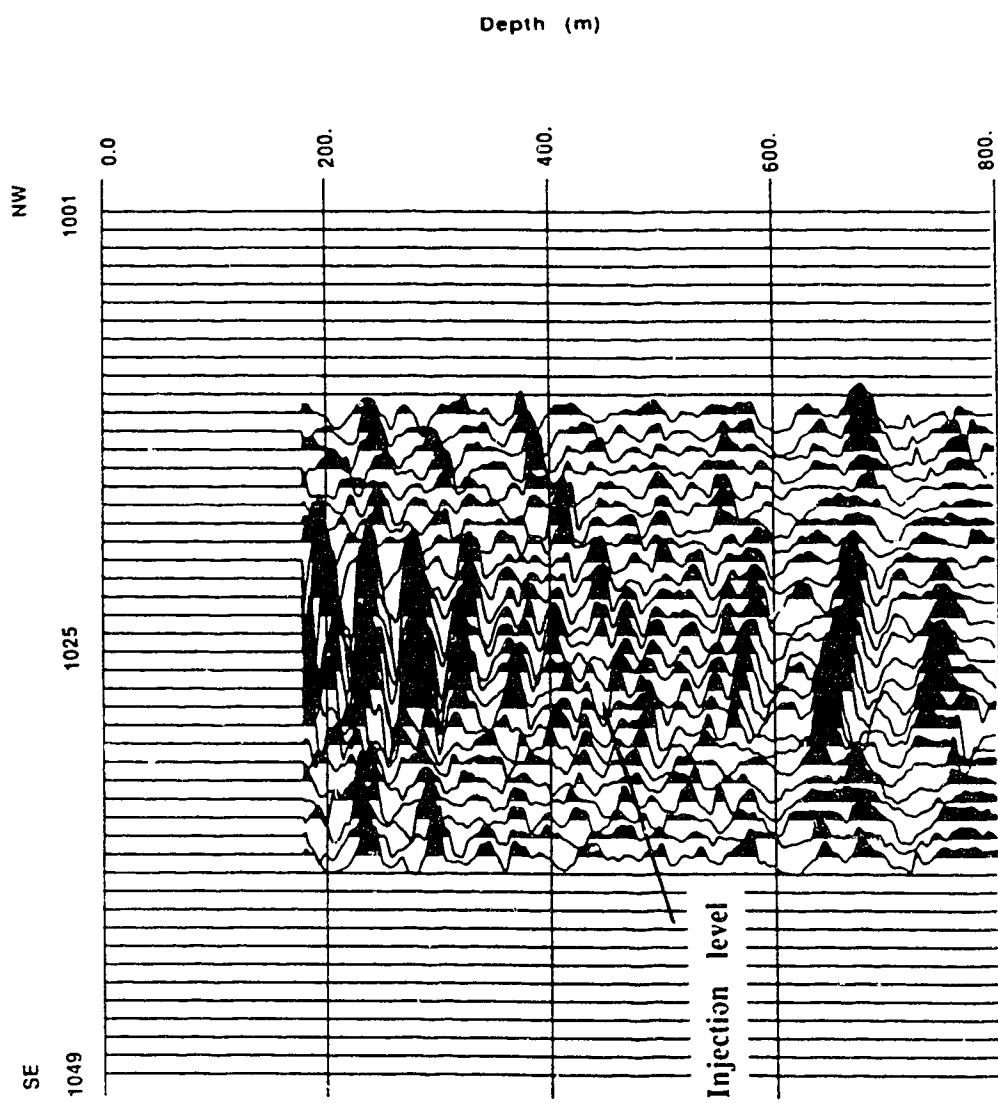


Figure 5.17 Migrated shot gather #1025 of line 82 after spatial muting.

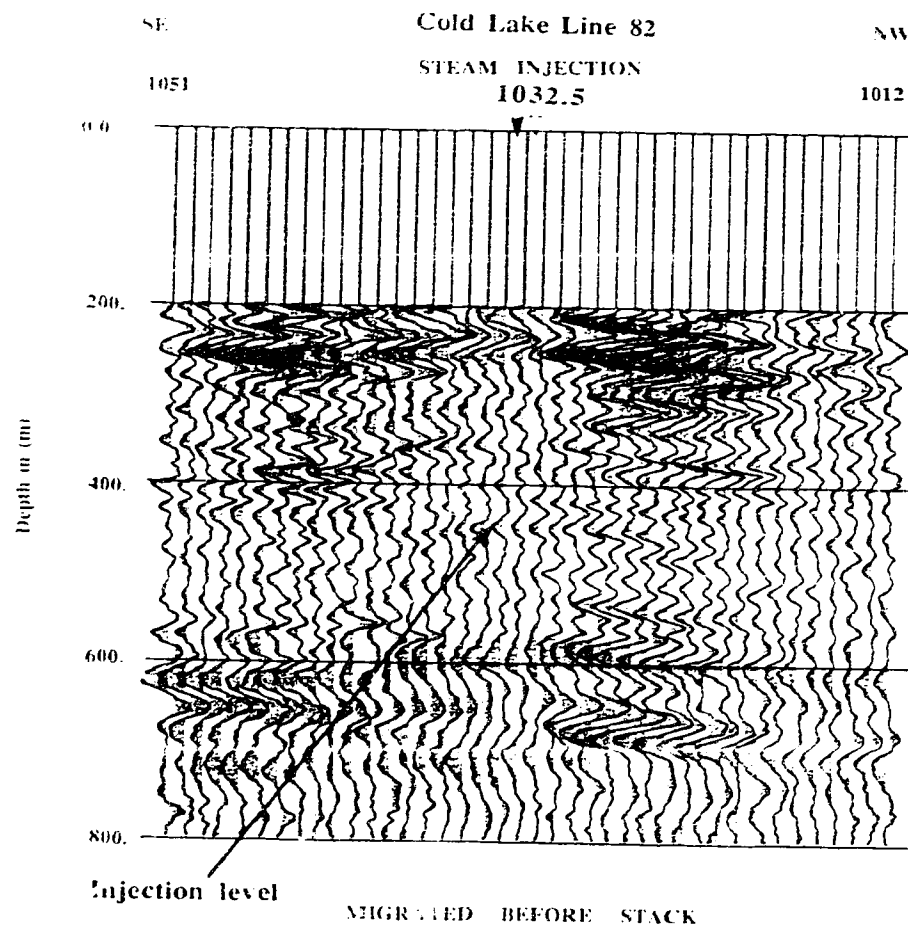


Figure 5.18 Migrated  $\omega$  -  $x$  stacked (MOXS) section for line 82, employing the pre-stack migration algorithm described in the text. (Arrow indicates the steam injection level).

Comparing both sections, namely, Figure 5.16 with Figure 5.18, one can see that the prestack migrated section shows higher overall resolution than the after stack migrated section. Also, in Figure 5.18 and at about 450m and between stations # 1029 to #1035 one can see that the reflected energy from the vapour zone due to the injected steam is more compactly imaged. It should be noted that the image of the Paleozoic horizon at 600m is much smoother than in Fig. 5.16. This would indicate that the lens of low velocity, due to the steam zone has been reasonably well corrected for.

## 5.6 Conclusions

A true amplitude processing of the three seismic reflection lines acquired by Esso over a steam injection location was carried out. It was shown that it is possible to carry out zero offset modeling incorporating attenuation and that this improves the model seismograms when compared to the field data. The relative reflection amplitude CMP stack section for line 82 was migrated and compared to the stack section obtained from a pre-stack shot gather migration. A new type of pre-stack seismic section **MOXS** (for migrated omega-x stack), has been developed which images the subsurface with higher resolution and better amplitude preservation. Although it has only been applied to a steam injection zone at Cold Lake, this method is quite general and may be applied to any seismic data set where subsurface inhomogeneities scatter or diffract the elastic waves.



## CHAPTER 6

### AMPLITUDE VERSUS ANGLE ANALYSIS FOR EOR PROCESSES

#### 6.1 Introduction.

In the last two decades the increasing importance of Enhanced Oil Recovery (EOR) and the realization that EOR plays an important role in the world's oil supply, has generated new experimental trials which involve the use of seismic methods for monitoring such processes. In this Chapter the changes in the reservoir formations caused by steam injection processes will be examined and methods of monitoring these with remote sensing seismic techniques will be explored. To provide a background to the interpretation of seismic wave measurements a short review on seismic wave attenuation due to wave propagation through fluid saturated porous media and the subsequent velocity dispersion will be given. In addition some observations on the petrophysical variations are included because of their reference to the theory of seismic reflection coefficients.

When steam is injected into the formation in sufficient volume to increase gas saturation even a few percent, what is observed on seismic reflection recordings is an amplitude enhancement (or *bright spot*) due to the change in the reflection coefficient over a region with hot vapor and the steam condensate in the reservoir formations. The large effects of fluid saturation on the compressional wave velocity,  $V_p$ , and relatively small effects on the shear wave velocity,  $V_s$ , is the reason why *bright spots* are detected over such heated zones. In general, the result on temperature changes and the change in fluid content cause in reducing the compressional wave velocity by as much as 10% to 60%.

An analysis based on reflection amplitude versus angle of incidence will be carried out for three seismic lines acquired over a steam injection location near Cold Lake, Alberta.

The results are imaged with a new type of display called an **ARPA** plot (Amplitude-Ratio for Partial Angle display on a common-mid-point section). This type of diagram distinguishes reflection zones with relatively low Poisson's ratio (0.16 - 0.20) and, as such, is able to delineate gas or steam zones from low or fully water saturated sediments. No pre-steam injection seismic reflection data were available to us, consequently we are not able to estimate the progression of the heated zone and the subsequent intrinsic wave attenuation.

## 6.2 A review of attenuation and velocity dispersion in fluid saturated rocks.

Attenuation is the anelastic process which dissipates seismic energy by conversion to heat thus decreasing the amplitude and modifying the frequency and phase content of a propagating wavelet. Seismic attenuation is commonly characterized by the quality factor  $Q$ . It is most often defined in terms of the mean stored energy  $W$  and the amount of the energy dissipated  $\Delta W$  during a single cycle of sinusoidal deformation:

$$Q = 4 \pi W / \Delta W \quad (6.1)$$

Two types of attenuation are known in the seismic literature, namely, the *intrinsic* attenuation due to rock anelasticity and the *apparent* attenuation. *Apparent* attenuation may be caused by interference effects and scattering from velocity or density inhomogeneities such as thinly bedded lithologic units. However, the *intrinsic* attenuation is of more interest in exploration geophysics because of its potential use in determining the presence and physical properties of the pore fluids (Meissner, 1983).

In a medium where wave propagation is linear and causal the presence of absorption requires the phase velocity to be a function of frequency. The relationship of frequency dependent phase velocity to frequency dependent absorption is known as the dispersion relationship, also as the Kramers - Kronig integrals, (Aki and Richards, 1980). Numerous dispersion - absorption pairs have been proposed. The method is usually to postulate a frequency independent or nearly frequency independent  $Q$  and use the Kramers - Kronig relationship to find the corresponding phase velocity.

Much of our current understanding of the physical process involved in wave attenuation and dispersion is due to the increased improvement of recent laboratory experiments that measure seismic velocity and attenuation over a range of frequencies, pressures, temperatures and fluid saturation. Spencer (1981), Winkler and Nur (1982), Murphy (1983), showed that attenuation and phase velocity are strongly dependent upon frequency in rocks containing fluids.

Attenuation in vacuum-dry rocks is negligible ( $Q$  of hundred of thousands) compared to typical  $Q$  values from the upper crust, even at low pressures (Clark et al, 1981; Murphy, 1983). It is strongly dependent upon fluid saturation in rocks containing a free fluid phase (Winkler and Nur, 1982; Murphy, 1983). These results mean that the absorption mechanism is due to the interaction of the pore fluids with the rock rather than absorption within the rock frame or the fluid.

Quantitative knowledge about velocity dispersion is difficult to obtain since there are no reliable methods by which one can measure the velocities as a continuous function of frequency over a broad band either in the field or in the laboratory. Velocity dispersion has both current and potential applications to exploration. In seismic and vertical profiling pulse shapes tend to distort with increasing travelttime due to absorption and dispersion within the earth. Potentially, measurements of dispersion and attenuation can be used as lithology and temperature indicators and/or microstructure indicators (Nyland, 1985; Tosaya et al, 1984).

Velocity dispersion in rocks is a pervasive, yet poorly understood topic in exploration geophysics. Essentially three different nonoverlapping frequency bands are used within the exploration community: seismic (10 - 150 ) Hz, sonic (1000 - 10000) Hz and ultrasonic (0.1 - 1 ) MHz. Velocity dispersion has been documented within each of these frequency bands (Wuenchel, 1965; Jones and Nur, 1983; Winkler, 1983; 1986).

Discrepancies between seismic and sonic velocities have also been interpreted in terms of velocity dispersion (Stewart et al, 1984). These results indicate that the frequency content, phase spectrum and velocity may be strong indicators of the type of pore fluid in a formation. Alternatively, if the type of the pore fluid is known, these attributes could be used to monitor temperature changes of a formation.

Wang and Nur (1988), use the low frequency limit Biot - Gassmann equations and the high frequency Biot equations, (Biot, 1956) to calculate velocity dispersions due to temperature increase in various rocks saturated with water and two heavy oils. The results show that the apparent velocity dispersions in light fluids (water and normal decane) saturated rocks are relative small, usually less than 3% to 5%, while those in the same rocks saturated with heavy oils are much larger, typically around 39%. Wang's results showed that Biot dispersions of both  $V_p$  and  $V_s$  are relatively small (usually less than 2%). The mechanism explained in the Biot theory that the velocity dispersions are caused by the inertial drag of the pore fluid; i.e. when an acoustic wave passes through a fluid saturated porous medium, the pore fluid moves under the differential pressure generated by the passing wave behind the solid frame. At low frequencies, the pore fluid is locked on the frame so there is no relative dispersion. At high frequencies, the effect of inertia caused by the density difference causes the motion of the pore fluid to lag behind that of the solid frame, which in turn leads to higher velocities.

A possible mechanism which can explain the velocity dispersion observed in Wang's experiments and calculations is the *local flow model*. Local flow means that the flow is controlled by the local fluctuations of the compressibility of the pore spaces. The

compressibility fluctuations are on the scale of pore size.

The local flow mechanism has been discussed by various investigators (e.g., O'Connell and Budiansky, 1977; Mavko and Nur, 1979; Winkler and Nur, 1982; Jones and Nur, 1983). Most of the laboratory data concerning wave propagation in fluid saturated porous media are best interpreted in terms of the local flow attenuation mechanism. This model predicts that  $Q$  and velocity depend upon the product of frequency and pore fluid viscosity, (Jones and Nur, 1983). When the dynamic modulus and  $Q$  are plotted as a function of frequency and pore fluid viscosity the resulting curves appear very similar to a standard linear solid or Zener peak (Jones, 1986).

The essential assumption in this mechanism is that some parts of the pore space are more compliant than other parts. A passing wave deforms the pore space and hence causes the pore fluid in the more compliant parts to tend to flow to the less compliant parts. The local flow mechanism also requires crack-crack and crack-pore connections in order to explain the dispersion results. That is to say, in order for the local flow to occur, the cracks and pores should be connected. In a partially saturated rock, pore fluid tends to flow to the empty regions of the pore space. The local flow mechanism is apparently related to the viscosity of the pore fluid, the permeability of the rock, the closure pressure of thin cracks, their aspect ratios, and the connectivity of the thin cracks to the round pores (high aspect ratio).

When the rock is saturated with a fluid of high viscosity, the time for the local flow to stop (or the pore pressure to equilibrate) is much longer due to the low mobility of the pore fluid. As a result the apparent dispersion of the velocity is larger. The opposite occurs when the rock is saturated with a fluid of low viscosity.

The apparent dispersion of the velocities explained in terms of the local flow mechanism depend not only on the viscosity of the pore fluid but also on the thin crack presence and their aspect ratios. If the pore space of a rock is only composed of round

pores (high aspect ratio), the velocity will basically have no dispersion since in this case all the parts of the pore space have the same compliance and hence there is no local flow to occur. As the effective pressure increases the crack tips connecting to the pores or other cracks will close, hence, the local flow activity of the pore fluid is limited and greatly decreased, with results in less apparent dispersion of the acoustic velocities.

The local flow mechanism is also related to the permeability of the rock. Low permeability rock usually contain cracks of small aspect ratios. For low permeability rocks in which the cracks are still connected, the apparent dispersion of the acoustic velocities should be higher than that for high permeability rocks since the local flow takes longer to get to equilibrium in low permeability rocks. No pre-steam injection seismic reflection data were available to us, consequently we were not able to observe and compute wave attenuation values from the available surface seismic reflection recordings. The values used in our model computations are either from hole to hole experiments or from laboratory data. This information on attenuation and dispersion should be taken into account in both forward modeling (chapter 5) and in pre-stack processing of the field data. In current processing of seismic data the degradation of high frequency is partially corrected by a deconvolution operation. Little attempt is being made currently to correct for dispersion which stretches the source wavelet but this could be corrected given a knowledge of  $Q$ .

### **6.3 Petrophysical changes during EOR processes.**

The influence of the pore fluid as separate from its pressure is related to its compressibility. When pore fluid is relatively incompressible (brine), the effective bulk modulus of the rock is high. Since this is only a volumetric change, the shear modulus is barely altered. In general, pore fluids tend to increase the compressional wave velocity because of their bulk modulus, but slightly decrease the shear wave velocity because of their density. When the pore fluid changes to steam or vapor the compressional velocity

drops sharply in comparison with the same rock fully saturated with water, whereas the shear velocity does not change much, in fact it may increase slightly due to the overall density decrease of the rock. When the ratio of the compressional to the shear wave velocities changes, a variation of the Poisson's ratio occurs. A change in the Poisson's ratio, produces a variation of seismic acoustic reflected amplitude at normal and nonnormal angles of incidence, (Ostrander, 1984; Domenico, 1976). There is strong evidence of Poisson's ratio as low as 0.16 in steam dominated geothermal fields (Majer and McEvilly, 1979), and between 0.20 to 0.23 in the *in situ* combustion processes, (Justice et al. 1989). Zones with low Poisson's ratio in the order of 0.15 - 0.23 (predominantly gas saturated zones) can cause an increase of reflected amplitude with angle, whereas, zones with high Poisson's ratio in the order of 0.35 - 0.4 (predominantly brine or water saturated ) cause a decrease in the reflected amplitude with angle. Such changes in the ratio of the seismic wave velocities and the Poisson's ratio suggest the application of seismic reflection methods in delineation and mapping of the heated zones generated by a thermal recovery during an EOR process.

The effect of confining pressure on rock is to deform the most compliant part of the pore space (e.g. microcracks and loose grain contacts) and increases the stiffness of the rock i.e. the effective bulk and shear moduli. The effect of high pore pressure due to the steam injection is to mechanically oppose the closing of cracks and grain contacts resulting from the confining pressure, thus leading to low effective moduli and velocities. When these two processes counteract each other they do not influence as much the variations of compressional and shear velocities.

Wang and Nur (1986; 1988), employing ultrasonic frequencies, demonstrated the effects of temperature on seismic velocities in oil saturated sands at confining pressures. The large decline in compressional velocity over the limited temperature interval of 20<sup>0</sup> C to 120<sup>0</sup> C, suggests that seismic velocities may serve in monitoring temperatures in heated oil zones around injector wells during a steam-flood or a fire-flood processes. They showed

experimentally that by increasing the temperature from 20<sup>0</sup> to 120<sup>0</sup> C the compressional and shear seismic wave velocities decrease. In particular the compressional velocity decreases by 10% to 15% in well consolidated sandstones saturated with heavy oil and by 15% to 40%, even 60%, in unconsolidated heavy oil and tar sands. The temperature dependence of the velocities is interpreted in terms of a phase transition of the heavy hydrocarbons and high pore pressure generated by the thermal expansion of the hydrocarbons. On the contrary, in a heated zone where most of the oil has been replaced by steam, we expect temperature effects to play a secondary role in the variation of both compressional and shear velocities of the reservoir.

Ito et al (1979), conducting laboratory measurements on Berea sandstone samples, demonstrated the variations of both compressional and shear wave velocities and thus Poisson's ratio, at geothermal temperatures (145 <sup>0</sup>C, and 195 <sup>0</sup>C) as the water in the pores is converted from liquid to vapor. They concluded that in the steam filled rock the compressional wave velocity is lower than in water filled rock. In contrast, the shear wave velocity is higher in steam filled rock. As a result the Poisson's ratio in steam saturated pores proved to be around 0.20 - 0.22 at 145 <sup>0</sup>C and 195 <sup>0</sup>C and 0.28 - 0.30 in water saturated pores at the same range of temperatures. Although laboratory measurements were made over a frequency range which is 10<sup>3</sup> - 10<sup>5</sup> higher than the typical *in situ* studies, the results provide important physical insight into the effects of steam on wave propagation in porous rocks.

Biot (1956), gave a theoretical treatment of elastic wave propagation in a fluid saturated porous solid where he accounted for the viscosity of a compressible fluid which may flow relative to the solid, causing frictional forces and consequently seismic attenuation. Gassman (1961), describes seismic wave propagation in a fluid saturated porous solid at low frequencies. One can visualize that for a long wavelength travelling wave, the relative displacement between fluid and rock skeleton is small compared to the



rock skeleton itself, because of the fluid viscosity. This justifies the assumption that fluid and solid move together. Geertsma (1961), using Biot's theory, developed basic equations for compressional seismic wave velocity as a function of frequency, as well as for zero and infinite frequencies.

For our purposes, to predict the effect on the compressional seismic velocity when steam is injected into the oil sand reservoir we have applied Geertsma's equation for zero frequency, neglecting the temperatures effects since we are dealing with a mature steam zone and assuming that there is a low percentage of hydrocarbon remaining in the pores of the reservoir. At zero frequency the equation is applicable when seismic wavelengths are much greater than pore dimensions as in the case of seismic reflection prospecting.

Geertsma's (1961) equation for the square of compressional seismic velocity at zero frequency in a fluid filled porous solid is given by:

$$v_p^2 = \frac{1}{\rho_b} \left[ \frac{(k_s - k_d)^2}{k_s(1 - \phi) - \left(\frac{k_d}{k_s}\right) + \phi \left(\frac{k_s}{k_f}\right)} + k_d + \frac{4}{3} N \right] \quad (6.2)$$

where

$k_s$  is the bulk modulus of the solid grain,

$k_d$  is the bulk modulus of the empty reservoir bulk material,

$\phi$  is the porosity,

$k_f$  is the bulk modulus of the pore fluid, and is given by the weighted by volume average of the steam condensate, steam and low viscosity bitumen:

$$\frac{1}{k_f} = S_w \left( \frac{1}{k_w} \right) + S_{st} \left( \frac{1}{k_{st}} \right) + S_{bit} \left( \frac{1}{k_{bit}} \right)$$

where  $S_w$ ,  $S_{st}$  and  $S_{bit}$  are the saturations of the steam condensate steam and bitumen satisfying:  $S_w + S_{st} + S_{bit} = 1$

and

$k_w$  is the bulk modulus for the steam condensate (water),

$k_{st}$  is the bulk modulus for the steam (gas), and

$k_{bit}$  is the bulk modulus for the bitumen

$N$  is the shear modulus of the dry bulk material,

and

$\rho_b$  is the bulk density and is given by:

$$\rho_b = \phi S_w \rho_w + \phi S_{st} \rho_{st} + \phi S_{bit} \rho_{bit} + (1 - \phi) \rho_s$$

where again  $\phi$  is the fractional porosity of the sand,  $S_w$ ,  $S_{st}$  and  $S_{bit}$  are the fractional volumes of the pores saturated with steam condensate, steam and low viscosity bitumen respectively,  $\rho_w$  is the steam condensate density,  $\rho_s$  is the sand grain density and  $\rho_{st}$  is the steam or gas density and  $\rho_{bit}$  is the bitumen density.

The fact that shear stresses are responsible for shear distortions the presence of fluid makes no difference to the shear modulus. Hence the shear modulus of the fluid saturated rock is the same as that of the skeleton alone.

The square of the shear velocity will be given by:

$$v_s^2 = \frac{N}{\rho_b}$$

(6.3)

Poisson's ratio,  $\sigma$ , for an isotropic solid may be given in terms of compressional and shear velocities of the saturated rock:

$$\sigma = \frac{(v_p^2/v_s^2 - 2)}{2 (v_p^2/v_s^2 - 1)}$$

(6.4)

Consequently, Poisson's ratio is expected to be a good discriminator between steam and hot water in the pore space and may be a useful tool in identifying these regions.

In summary, by current theoretical models the petrophysical alterations which contribute to velocity changes of seismic waves in hydrocarbon reservoirs during an EOR process may be caused predominantly by replacing the bitumen by steam or steam condensate and secondarily by temperature changes of the reservoir especially when most of the heavy oil is displaced from the pores of the porous medium.

#### 6.4 Amplitude versus angle variation due to steam injection.

Since the same petrophysical effects described earlier are anticipated to occur also *in-situ*, we can use remote seismic methods to continuously monitor reservoirs throughout the thermal enhanced oil process to map the flooded zones in a steam stimulation enhanced oil recovery operation. This velocity decrease and the variable fluid saturation imply that both a time delay and an amplitude brightening of seismic reflections from subsurface zones invaded by the steam zone can be observed on seismic sections.

When steam is injected at high pressures and temperatures (10 MPa, 315°C) into the Clearwater oil sands it is trapped by the shale barrier located above the perforation depth. At the same time as the heavy oil in the oil sands is produced the pores are filled with either steam (mixed with liberated gas) and steam condensate. Consequently, a boundary is formed between the shale above and the hot fluid saturated oil sands below. For the shale formation the values used were as follows: compressional velocity  $v_p = 2300$  m/sec, bulk density  $\rho = 2200$  kg/m<sup>3</sup>, Poisson's ratio 0.32, derived from a well logged near

the injection area resulting a shear wave velocity  $v_s = 1183$  m/sec. Assuming that the sands are composed by 100% quartz, employing equations (6.2 - 6.4), we compute the anticipated compressional and shear seismic wave velocities and Poisson's ratio for various water, bitumen and steam saturations ( $S_w$ ,  $S_{bit}$ ,  $S_{st}$ ). The petrophysical parameters describing the sand material were taken from White and Sengbush, (1987).

Table 6.1 depicts the compressional shear wave velocities, bulk density and Poisson's ratio for the saturated layer after steam injection for various water, bitumen and steam saturations ( $S_w$ ,  $S_{bit}$ ,  $S_{st}$ ).

**Table 6.1. Compressional and shear wave velocities, bulk densities and Poisson's ratios for various  $S_w$ ,  $S_{st}$ , and  $S_{bit}$**

$S_w$	$S_{st}$	$S_{bit}$	$V_p$ m/s	$V_s$ m/s	$\rho_b$ kg/m <sup>3</sup>	Poisson' ratio
0.00	0.90	0.10	1823	1217	1890	0.10
0.00	0.70	0.30	1806	1203	1932	0.10
0.65	0.25	0.10	1770	1166	2058	0.12
0.85	0.05	0.10	1841	1152	2109	0.18
0.70	0.00	0.30	2068	1151	2113	0.28
0.90	0.00	0.10	2224	1148	2122	0.32

Using the data depicted in Table 6.1 we calculate the P-P reflection coefficients according to Zoeppritz's equations, (Young and Braile, 1976). Figure 6.1a, illustrates P - P reflection coefficients for various water, bitumen and steam saturations ( $S_w$ ,  $S_{bit}$ ,  $S_{st}$ ) for a porosity  $\phi$  equal to 0.30. The absolute increase of the amplitude of the reflected

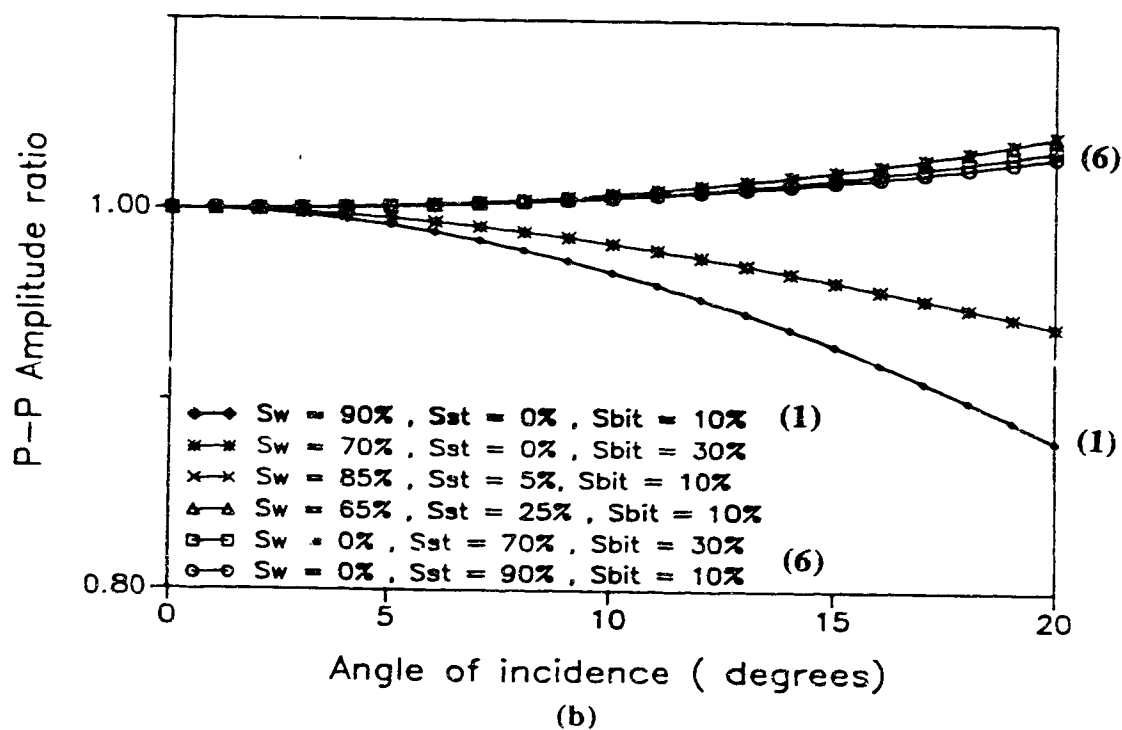
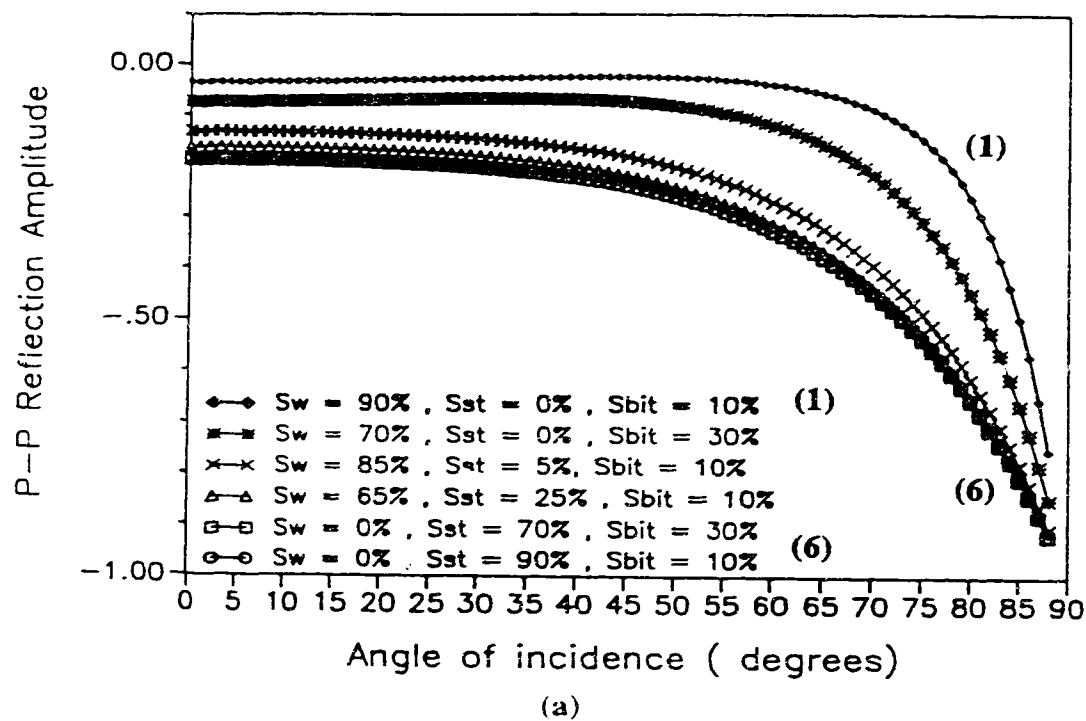


Figure 6.1 (a) P - P reflection coefficients for the shale - porous oil sand interface. (see text for details).

(b) Normalized P - P reflection coefficients shown in (a).

compressional wave is evident for even low percentage of steam saturation indicating that even an amount of 5% of steam is enough to increase the reflected amplitude with angle of incidence. When we have low viscosity bitumen and water in the pores the P-P reflection coefficient remains almost constant until  $60^\circ$  and then increases. Figure 6.1b, depicts the normalized ratios of the compressional reflection coefficients shown in Figure 6.1a. Clearly, the P - P reflection amplitude ratio is increasing for even a small amount of steam (gas) in the pores and decreasing when the pores are occupied with steam condensate and low viscosity bitumen.

## 6.5 Formulation of the Amplitude versus angle analysis

Amplitude versus source-receiver offsets or angle of incidence analyses are designed to reveal that angle dependent information, which, in certain depositional settings can provide an important clue to the presence of gas or water saturated contacts within the reservoir. Since the reflection coefficient depends on the reflection angle, such information is lost in the conventional common midpoint (CMP) stacking due to the fact that the amplitude of each event in the stack represents an average over all offsets.

Amplitude versus offset can be observed by plotting various CMP - NMO corrected gathers at selected offsets. Alternatively, amplitude versus angle can be observed from transformed traces recorded at fixed offsets into traces characterized by a range of angle of incidence.

To study reflectors at different times or equivalent depths it may be more convenient to use angle trace gathers. Using the root mean square velocity  $v_{rms}$  for the area and assuming no dip, (in fact the area under investigation has regional dips less than  $1^\circ$ ), time offset pairs can be computed as follows:

From the NMO equation for flat layer geometry we have:

$$t_x^2 = t_0^2 + \frac{x^2}{v_{rms}^2} \quad (6.5)$$

where  $x$  is the shot - receiver offset,  $t_0$  is the zero offset two-way travel time and  $t_x$  is the two-way travel time from the shot to a particular receiver offset  $x$ ;

After differentiation and noting that  $t_0$  is a constant we have:

$$2 t_x dt_x = \frac{2 x dx}{v_{rms}^2} \quad (6.6)$$

Cancelling out the 2's and recognizing that  $dt_x / dx = p = \sin \theta / v_1$  where  $\theta$  is the angle of incidence and  $v_1$  is the first layer interval velocity, solving for  $t_x$ , we have:

$$t_x = \frac{x}{p v_{rms}} \quad (6.7)$$

Substitute  $t_x$  in the equation (6.5), and solving for the shot receiver offset  $x$ , we have:

$$x = \frac{v_{rms}^2 p t_0}{\sqrt{1 - p^2 v_{rms}^2}} \quad (6.8)$$

As a result various time-offset windows are obtained for various angles of incidence  $\theta$  and different zero offset two-way traveltimes  $t_0$ . Figure 6.2, illustrates the time-offset windows calculated for the various range of central angles used, namely,  $5^\circ - 10^\circ$ ,  $10^\circ - 15^\circ$  and  $15^\circ - 20^\circ$ . These windows are applied to NMO corrected CMP gathers, to produce angle stack sections for the specified angles of incidence.

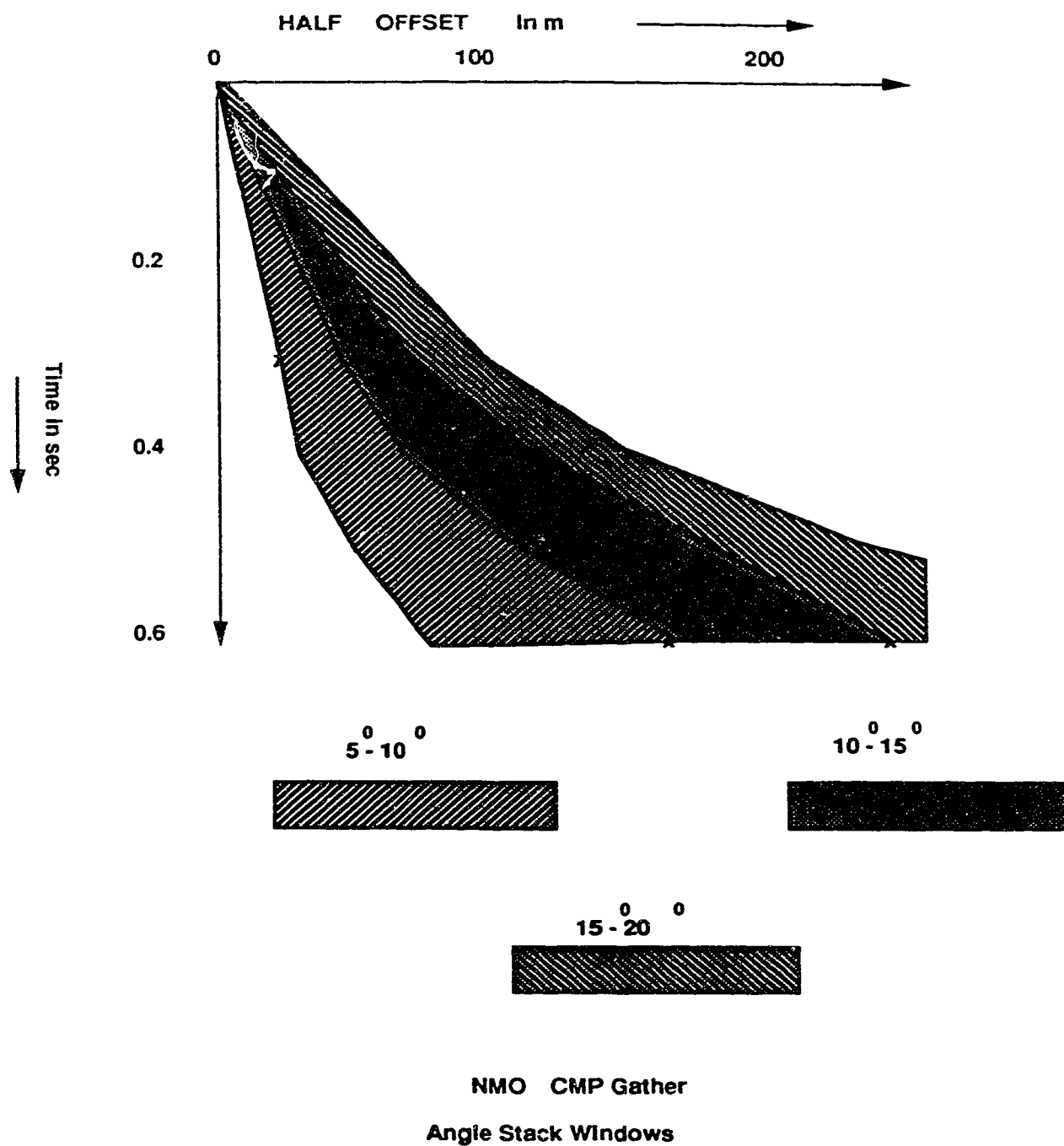


Figure 6.2 Time - offset windows computed for different angles of incidence namely,  $5^{\circ} - 10^{\circ}$ ,  $10^{\circ} - 15^{\circ}$ ,  $15^{\circ} - 20^{\circ}$ .



An angle gather, consists of traces which have been formed by combining those portion of the traces in a CMP gather that contain arrivals within a time range of reflection angles. The normalized sum of the portion of these traces results an angle stack trace. Performing these operations on all CMP gathers and stack we obtain the equivalent angle stack sections.

## 6.6 Imaging Amplitude versus offset reflection seismic data.

From the zero offset modeling described in Chapter 5 the heated zone is located at 500 ms on the CMP stack section. Figure 6.3(a - c), depict a time window (0.35 s - 0.65 sec) for various range of angles of these angle stacks for seismic reflection line 82. Gaps in the data are due to the fact that near offset traces were not recorded during the reflection seismic survey in some parts of the seismic lines. Figure 6.3(a - c) clearly illustrates the increase of amplitude with angle between CMP's #1028 to #1036 at around 0.5 s. Similar results can be revealed for lines 81 and 80 (not shown here).

The sum of the absolute seismic reflected amplitudes are computed within a 50 ms time window of selected time horizons of the angle stack sections. Running such time windows across the seismic angle stack sections, one gets an overview of reflected amplitude variation with angle for each CMP trace. Figure 6.4(a - c), depict amplitudes of three chosen angle windows namely  $5^{\circ}$  to  $10^{\circ}$ ,  $10^{\circ}$  to  $15^{\circ}$  and  $15^{\circ}$  to  $20^{\circ}$ , for the interval of 425 to 575 ms for every 50 ms time window, for line 82. Zero amplitude is due to the lack of recording near offset traces. Again one can see that between CMP # 1028 to CMP # 1036 and for the time gate of 475 - 525 ms the amplitudes for the  $15^{\circ}$  -  $20^{\circ}$  dominate whereas, for the adjacent CMP's the  $5^{\circ}$  -  $10^{\circ}$  amplitudes are stronger. Similar results can be observed for the other two lines (not shown here).

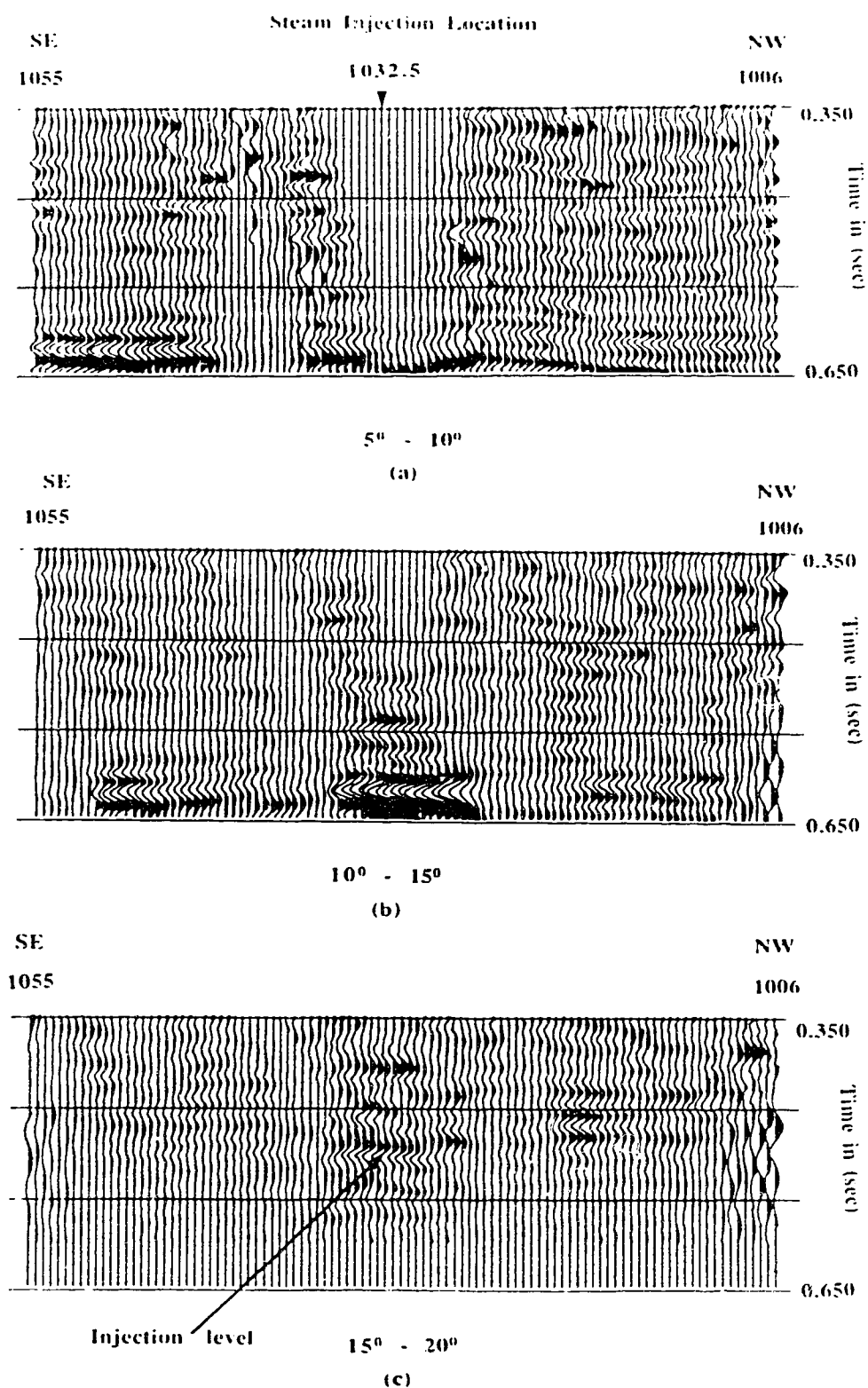


Figure 6.3 (a) Angle stack for the range of  $5^{\circ}$  -  $10^{\circ}$ , for line 82.  
 (b) Angle stack for the range of  $10^{\circ}$  -  $15^{\circ}$ , for line 82.  
 (c) Angle stack for the range of  $15^{\circ}$  -  $20^{\circ}$ , for line 82.  
 (arrow indicates the steam injection level)

## Cold Lake Line 82

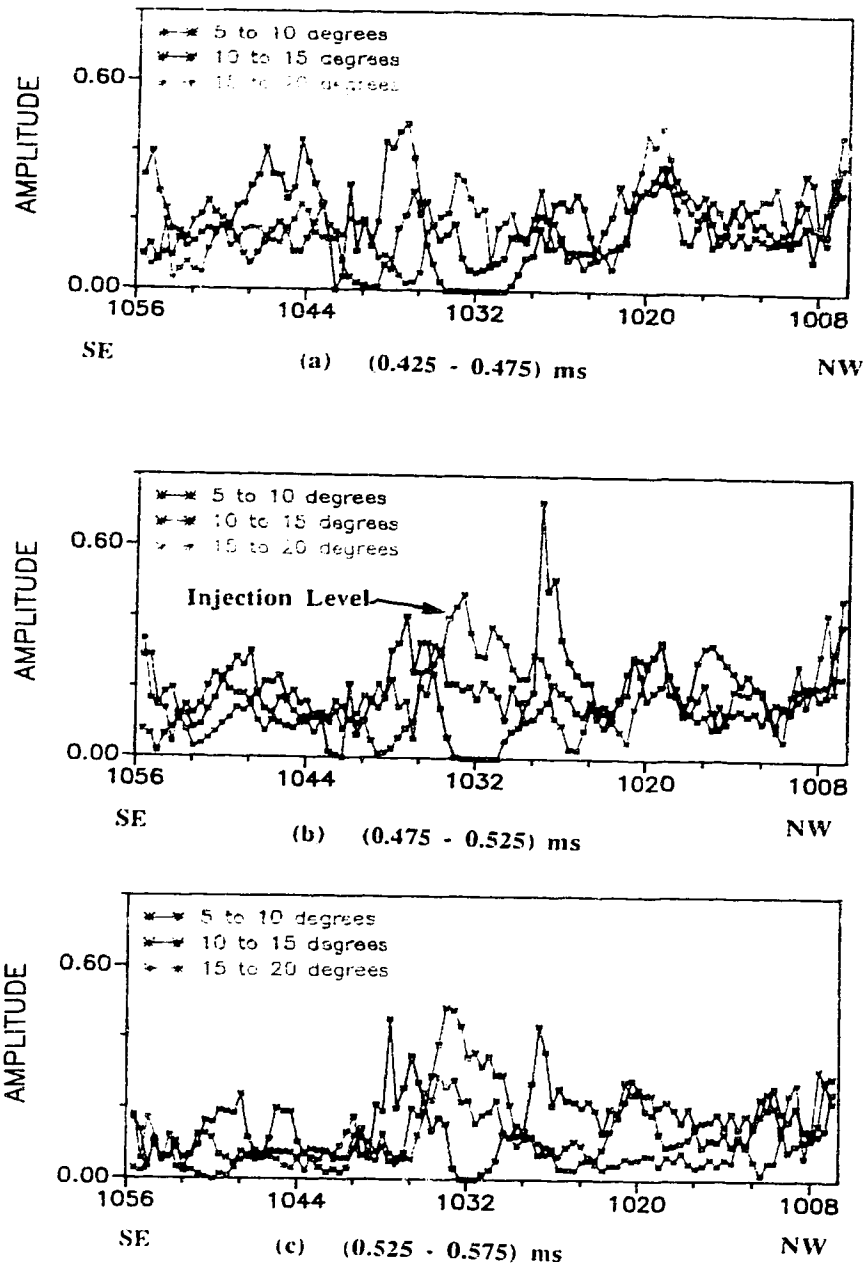


Figure 6.4 (a) Sum of reflected amplitudes for the (425 - 475) ms time window, for line 82. (b) Sum of reflected amplitudes for the (475 - 525) ms time window, for line 82. (c) Sum of reflected amplitudes for the (525 - 575) ms time window, for line 82.

An Amplitude-Ratio for Partial Angle (**ARPA**) plot, illustrates a summary of the magnitudes and the ratio of the reflected amplitudes with respect to the angle of incidence, for the various angles employed, with the respective CMP stack section displayed in the background. High reflected amplitude (red) and high amplitude-ratio (thickness of the vertical color lines) indicate low water or steam condensate saturation, i.e predominantly steam or gas zones.

Figures 6.5 to 6.10, depict **ARPA** plots for the three seismic reflection lines. In particular, in Figures 6.5 - 6.7, the background consists of stack sections where the full conventional seismic processing is applied (Esso's CMP sections), whereas in Figures 6.8 - 6.10 the amplitude preserved processing sequence described in Chapter 5 was applied to the section shown as the background. Figures 6.7 and 6.10 illustrate **ARPA** plots for line 82, where one clearly identifies the saturated zone located at 0.5 sec and extends from CMP # 1028 to CMP # 1036, having a lateral dimension of 144 m. Similarly, the high amplitude high ratio characteristics can be observed for line 81 (Figures 6.6, 6.9) and for CMPs #1052 to #1059 and for line 80 (Figures 6.5, 6.8) from CMPs #1038.5 to #1047.

The time zone between 0.525 - 0.575 ms which is the reflection from the McMurray formation is of interest too. For example for line 82 and for CMPs #1029 - #1035 the amplitude of the  $10^0$  to  $15^0$  angle window dominates over the other two. This is the manifestation of absorption and focusing occurring behind low velocity pods. Energy has been absorbed for the  $5^0$  -  $10^0$  (near vertical incidence) angle window whereas has been focused for the  $10^0$  -  $15^0$  angle window due to ray bending. The reason that the reflected amplitude dropped for the  $15^0$  -  $20^0$  angle window is due to the lack of wide offsets recorded for the depth under consideration namely 510m. In fact, due to ray bending around the heated zone, the estimated angle windows underestimate the real angles of

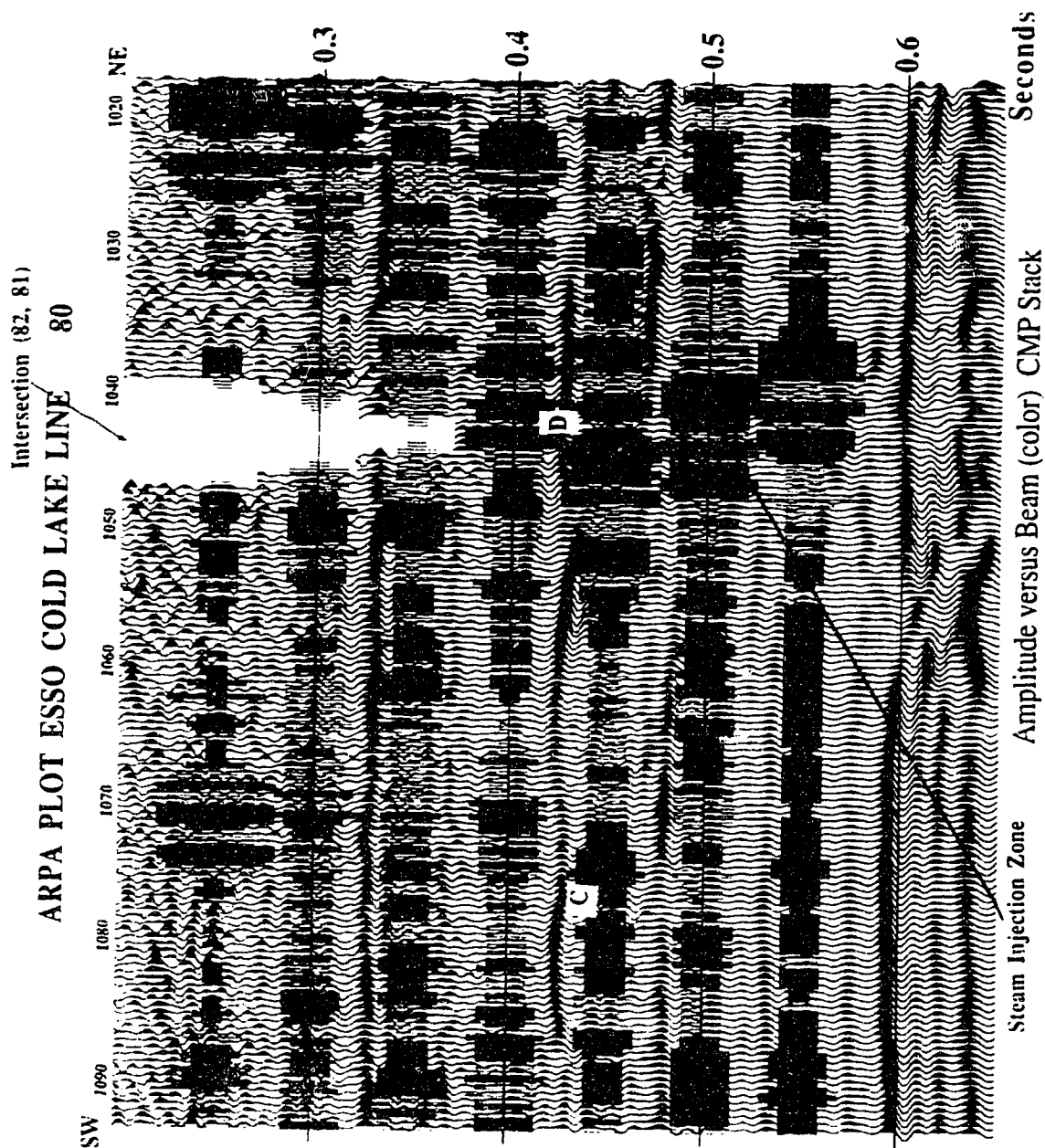


Figure 6.5 Amplitude Ratio for Partial Angles (ARPA) plot for line 80 with

Esso's processed CMP stack section shown as the background

(Locations C and D, indicate potential gas saturated regions.

Arrow indicates the steam injection level)

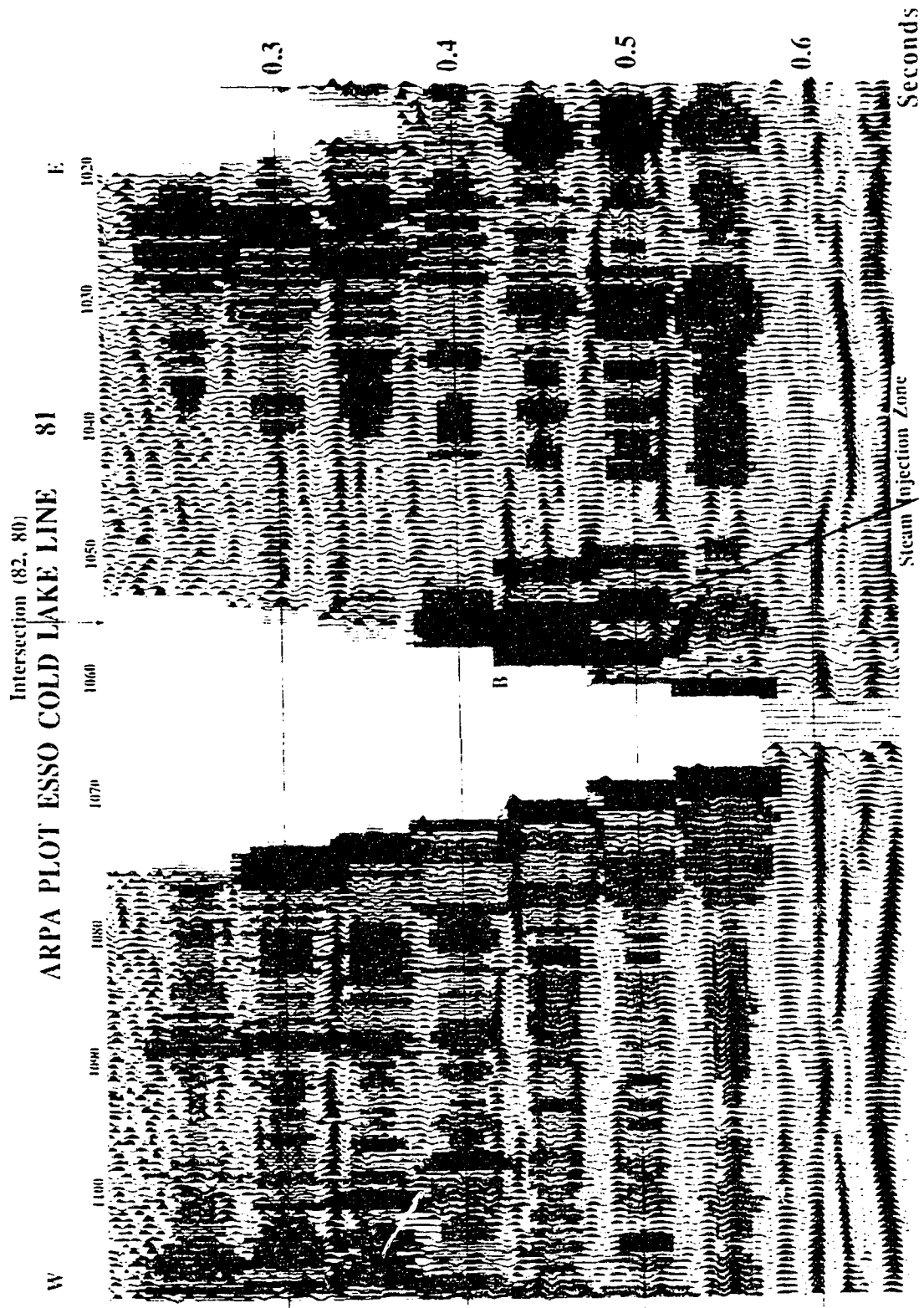


Figure 6.6 Amplitude Ratio for Partial Angles (ARPA) plot for line 81 with

Esso's processed CMP stack section shown as the background.

(Location B indicates a potential gas saturated region)

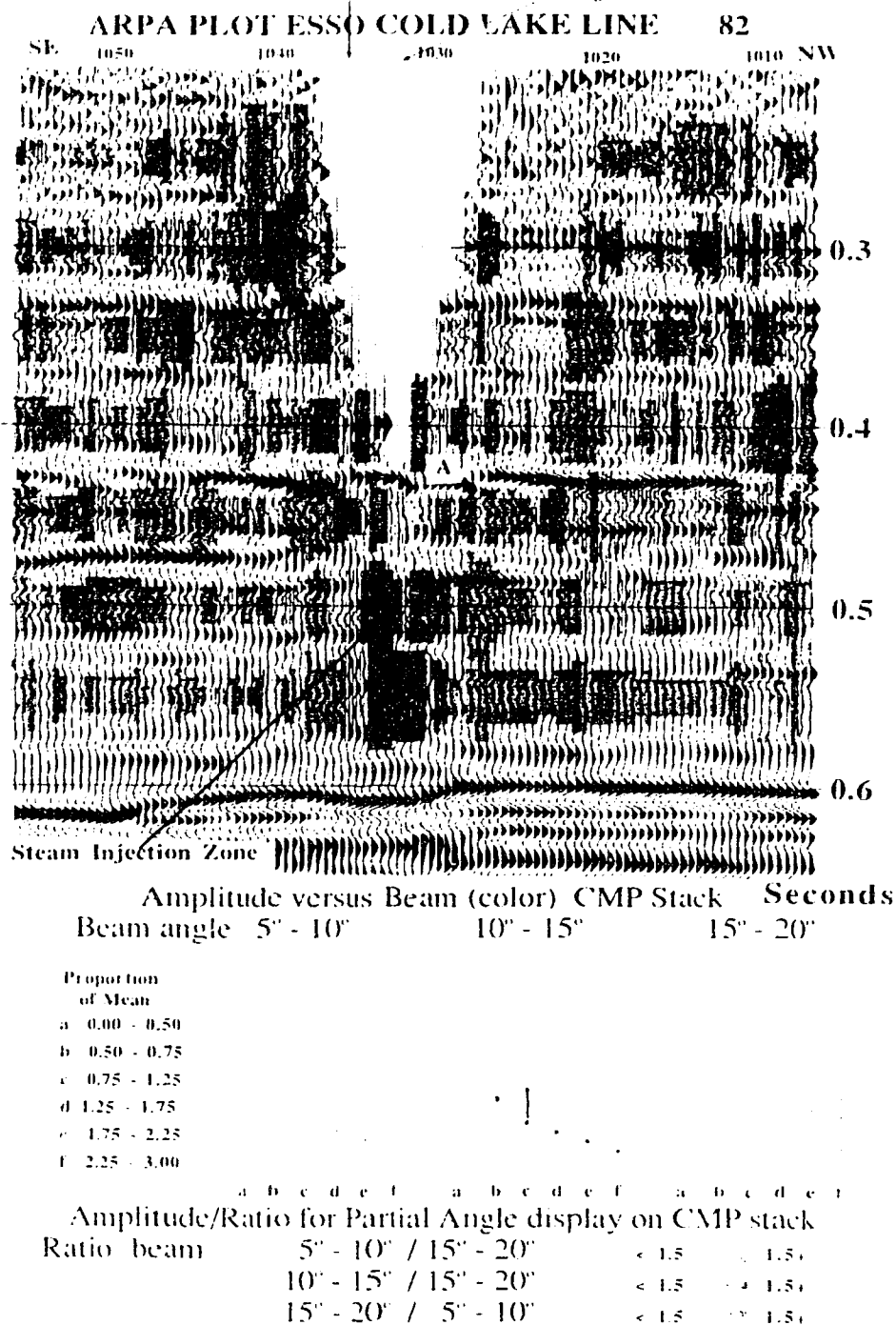


Figure 6.7 Amplitude Ratio for Partial Angles (ARPA) plot for line 82 with Esso's processed CMP stack section shown as the background (Location A indicates a potential gas saturated region). (arrow indicates the steam injection level)

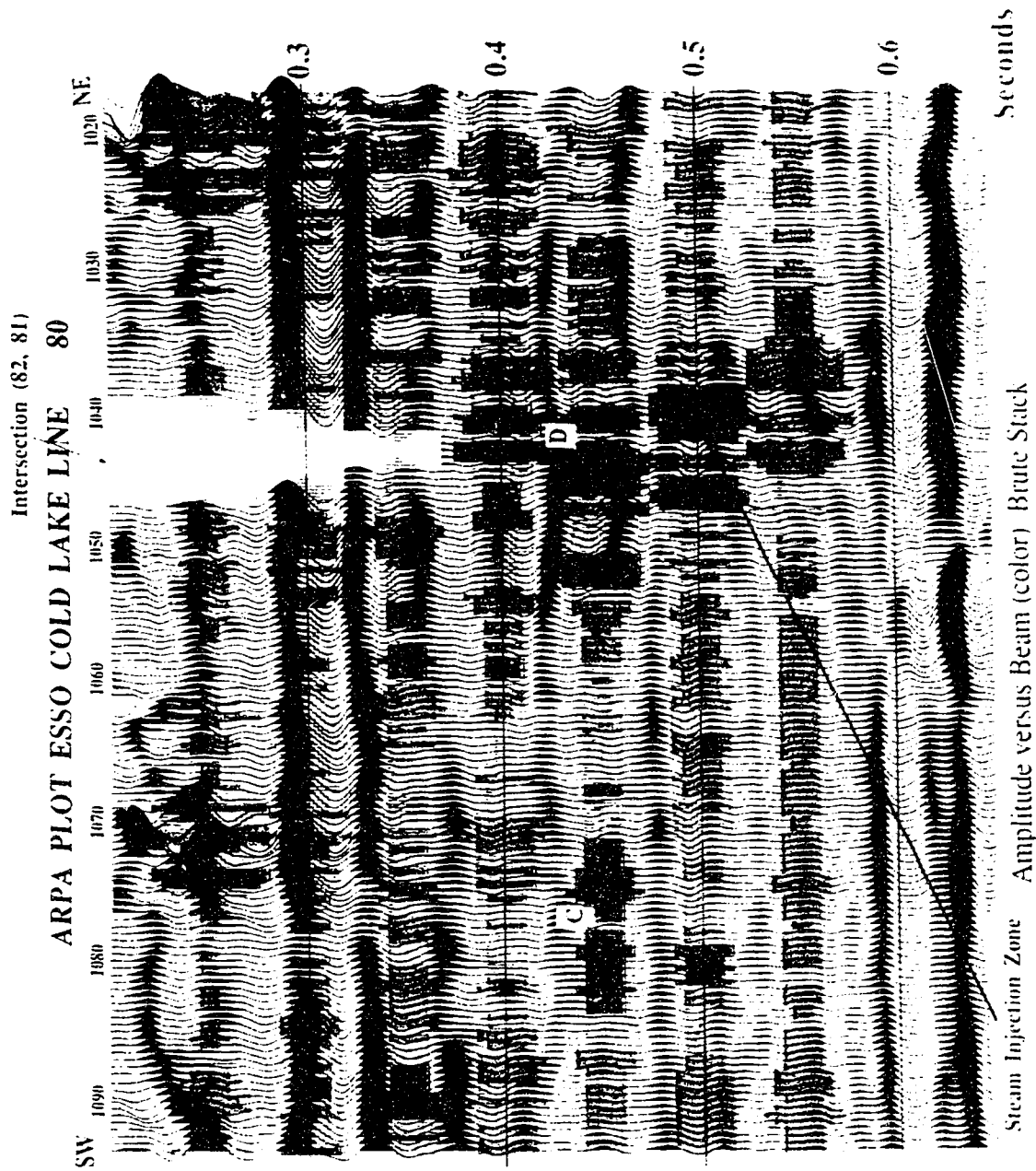


Figure 6.8 Amplitude Ratio for Partial Angles (ARPA) plot for line 80  
with relative amplitude processed CMP stack section shown as  
the background

Locations C and D, indicate potential gas saturated regions, arrow indicates the steam injection level.



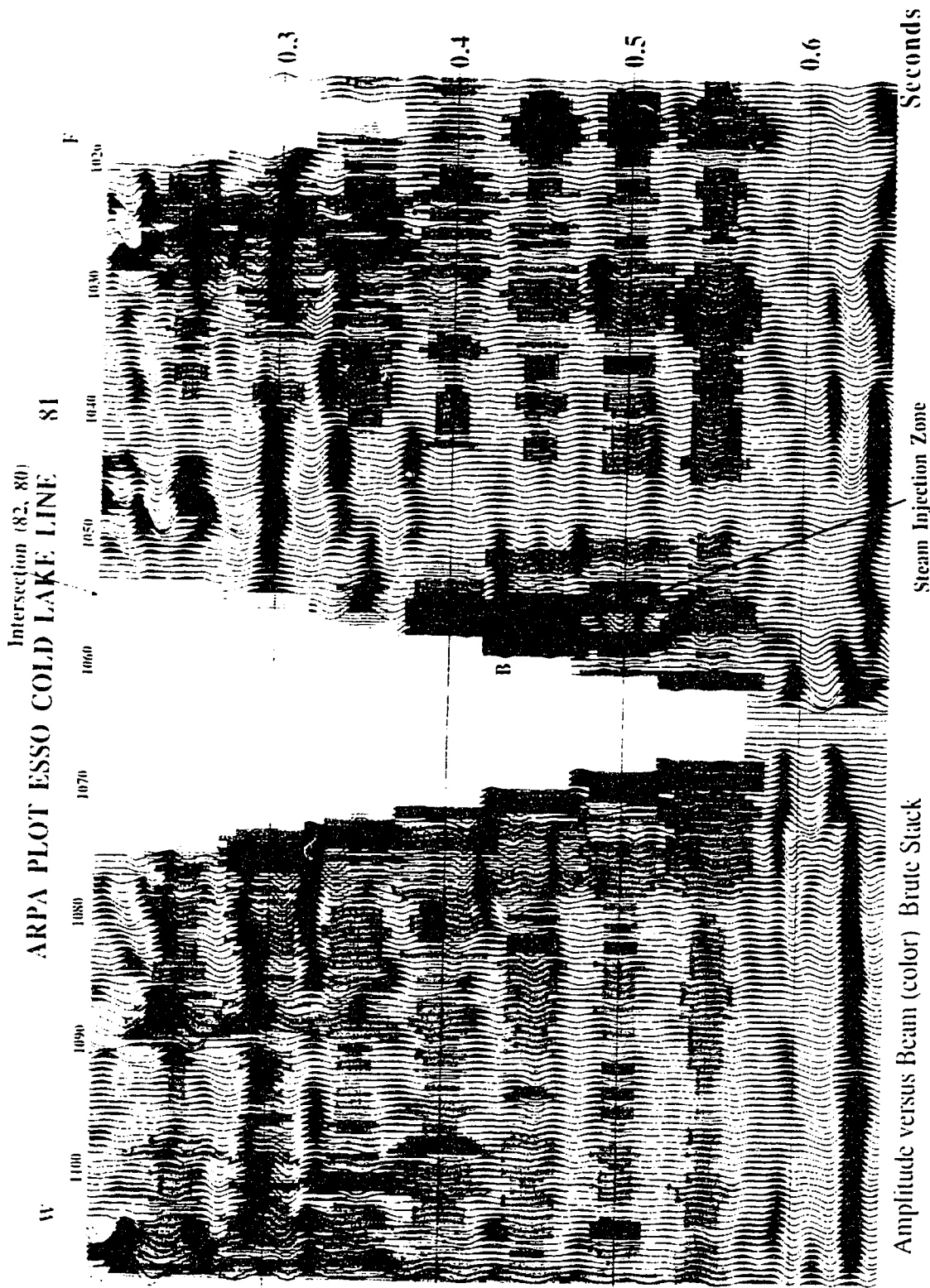


Figure 6.9 Amplitude Ratio for Partial Angles (ARPA) plot for line 81

with relative amplitude processed CMP stack section shown as  
the background

(Location B indicates a potential gas saturated region. Arrow indicates the steam injection level)

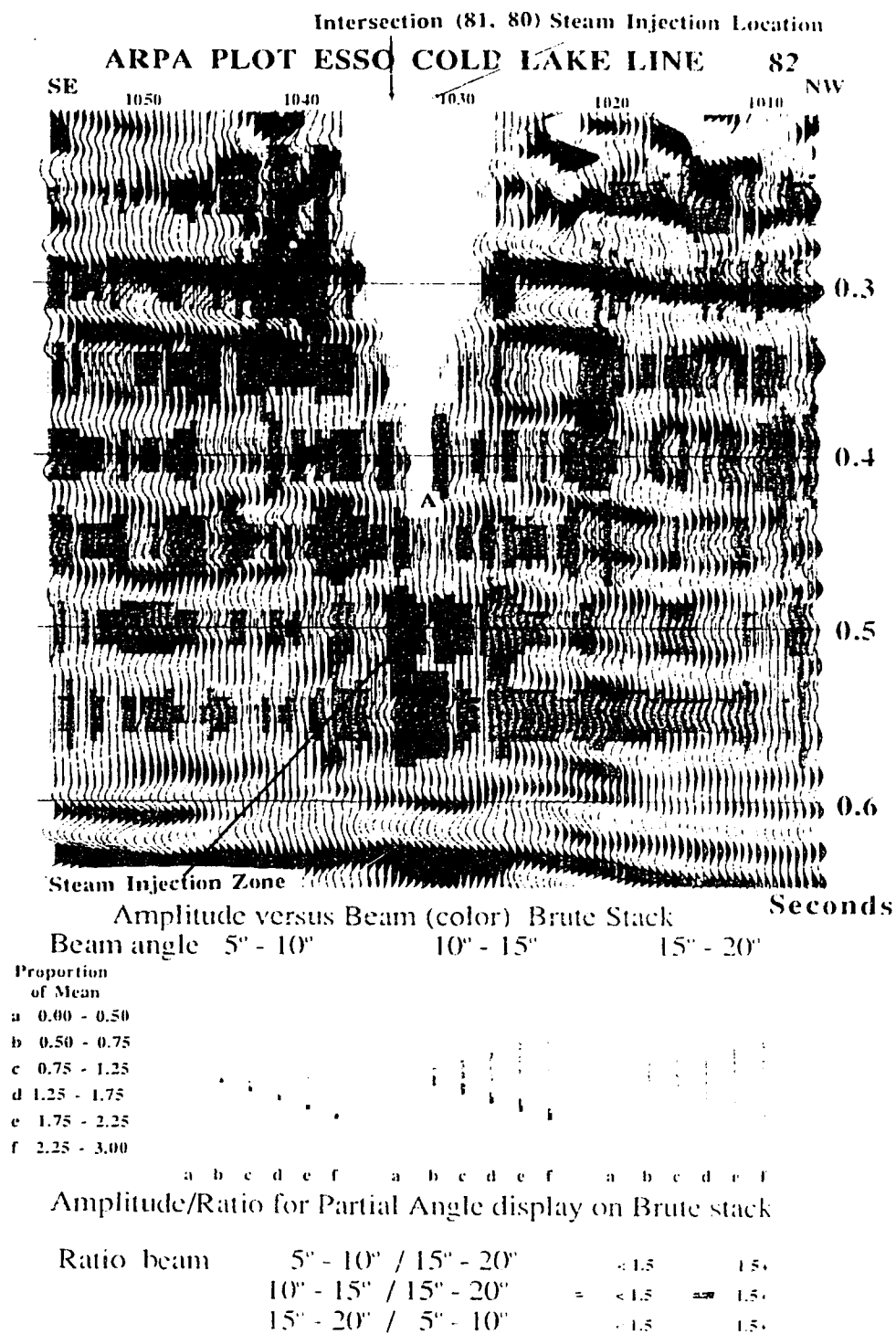


Figure 6.10 Amplitude Ratio for Partial Angles (ARPA) plot for line 82 with relative amplitude processed CMP stack section shown as the background (Location A indicates a potential gas saturated region. Arrow indicates the steam injection level).

incidence which are larger. Hence, for the  $10^0 - 15^0$  angle window we get contributions from larger angles as well. For the angle window beyond  $20^0$  we also run out of full coverage according to our limited offsets. Well log information reveals that the basal McMurray sands are mainly water bearing formations which also cause the reflection coefficient to remain constant with angle of incidence (Harrison et al, 1979). The same effects are observed in the other lines namely, 81 and 80.

Considering the above arguments one can establish the lateral extent of the steam injected zone by looking at both time windows, namely, 0.475 - 0.525 ms and 0.525 - 0.575 ms for the different seismic lines according to the two characteristics namely:

1. On the increase of reflected amplitude with angle for the time zone where the reservoir is located and,
2. The increase of reflected amplitude for the  $10^0 - 15^0$  angle window due to the focusing effects behind the low velocity pod.

Figure 6.11, illustrates the final interpretation derived for the lateral extent of the reservoir zone affected by the steam. The boundaries between the seismic lines are simply manually interpolated due to the lack of data in these regions. The extent of the zone is, for line 80 from CMPs #1038 to #1047 a total of 162m, for line 81 from CMPs #1052 to #1059 a total of 126m and for line 82 from CMPs #1028 to #1036 a total of 144m.

Inspecting the **ARPA** plots one identifies other places where the same characteristics do appear. For instance in Figures 6.7 and 6.10 location A indicates a potential gas zone. In Figures 6.6 and 6.9 location B also indicates a high reflected amplitude for large angles. Finally, locations C and D in Figures 6.5 and 6.8 also indicate potential gas saturated regions. Moreover geological information reveals that gas pockets in various zones are often present in the Upper and Lower Grand Rapids formations.

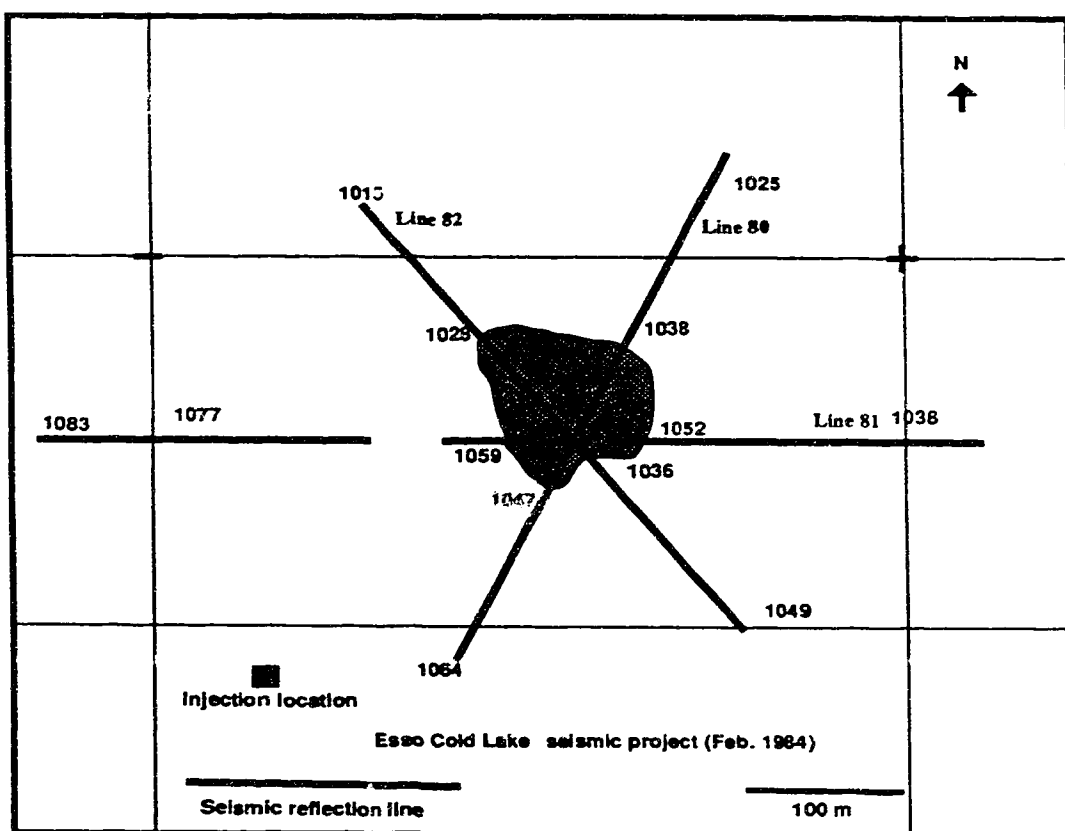


Figure 6.11 Plan view of the area under investigation illustrating the lateral boundaries of the steam invaded zone (Part of the seismic lines and the surface location of steam injection well are also shown).

Marx and Langenheim (1959), developed an analysis for steam injection growth based on reservoir heating by hot fluid injection. For a period of three years of steam injection an estimate of the steam zone diameter is found to be equal to 106m and for a five year period of steam injection the steam zone diameter is found to be equal to 180m. Appendix E outlines the procedure and the calculations involved to produce the above steam zone estimates.

## 6.7 Conclusions

During thermal EOR operations the reservoir formations undergo substantial physical alterations. Seismic reflection surveys, when well acquired and carefully processed, are able to detect such changes and thus, can be used to monitor these EOR processes. A pre-stack amplitude versus angle analysis of the seismic reflection lines identified the steam invaded zones. The Amplitude-Ratio for partial angle plots (ARPA), proved to be a helpful imaging tool in distinguishing changes in Poisson's ratio and therefore whether steam vapor or steam condensate was present in the heated zone.

## CHAPTER 7

### CONCLUSIONS

This thesis explores methods by which one may interpret seismic reflection data for the anisotropic properties of the layers and seeks to find new ways of displaying the elastic wave information to image small heterogeneous zones with high resolution, and to display Poisson's ratio as an interpretative tool in obtaining fluid content.

As nearly two-thirds of the original oil in place can not be recovered by conventional recovery methods in most oil reservoirs, methods of Enhanced Oil Recovery (EOR) become more and more important. Real time mapping of EOR operations can provide the opportunity to control or modify the recovery process, thus reducing operating costs. Since reservoir heterogeneities have been shown to be the most important cause of EOR failure, detailed reservoir characterization is essential before embarking upon such a project. The petrophysical parameters describing the reservoir undergo substantial alterations when such EOR operations take place. The preferred directional orientation due to the new dynamics introduced into the reservoir formation may cause seismic anisotropy. Two new algorithms adapted for the vector CDC - 205 supercomputer employing the MacCormack finite difference splitting technique were developed to model P-SV and SH seismic wave propagation in transversely isotropic media. Full waveform synthetic seismograms were computed for various isotropic and anisotropic models, which illustrated the necessity of such algorithms. Since the computation of the full waveforms is essential in the non-linear full waveform inversion, we believe that the algorithms will show enormous potential for the estimation of the anisotropic parameters of the inhomogeneous media. The extension of the present algorithms to model seismic elastic waves propagating in the three dimensional anisotropic inhomogeneous media is one of

future concern and interest to the author.

In the last two decades geophysical, specifically seismic techniques and digital image processing techniques, have been directed towards the improvement of spatial image resolution of the reservoir. Migration is a technique which enhances lateral resolution and thus contributes to the delineation of heterogeneous zones. A new type of migration before stack has been developed in this thesis to image diffracted elastic waves. The migrated omega -  $\omega$  stacked (MOXS) depth images obtained illustrate the effectiveness of the algorithm in obtaining higher resolution and better amplitude preservation on seismic depth sections than normal after - stack common midpoint (CMP) conventional depth migration algorithms. The algorithm in this research can be incorporated into an iterative method to perform depth migration and velocity analysis simultaneously. Another future application for the migration algorithm presented here is the tomographic - prestack depth migration approach where one updates the velocity field by performing a tomographic inversion and then uses this new velocity field to perform a shot gather depth migration. The shot gather depth migration algorithm developed in this research can be used to migrate mixed-mode (P-SV) wavefields. However, it is necessary to separate the wave types P-wave and SV wave prior to migration. This may be achieved through wave mode filtering, (Devaney and Oristaglio, 1986; Dankbaar, 1985). Migration then can be performed twice; once for the P-waves and once for the SV waves. For the P-waves one has to follow the steps described in Chapter 4. For the SV waves, one has to perform ray-tracing according to P-wave velocities followed by a downward continuation (equations 4.10 ; 4.11; Chapter 4) according to S-wave velocities. Then perform the imaging condition according to equation 4.13, Chapter 4.

Esso Resources conducted in 1984, a seismic experiment over a steam injection site, near Cold Lake Alberta, consisting of the acquisition of three seismic lines. A relative amplitude processing was carried out in the Seismology Laboratory at the University of

Alberta, employing various innovative algorithms written by the author. The images produced by the reflected energy from the steam invaded zone on the three seismic sections, were identified and correlated with synthetic zero offset modeling sections.

The prestack migration developed in this thesis was applied to the relative amplitude processed shot gathers. After a common geophone stack operation, according to equation 4.13 Chapter 4, the obtained MOXS section imaged more compactly the lateral boundaries of the steam invaded zone than an after stack depth migrated section, which is routinely applied during an industrial seismic data processing stream.

An amplitude versus angle (AVA) analysis was performed on the common midpoint (CMP) gathers to obtain information on the variation of the reflection coefficient with ray angle. This appears to be a promising method for identifying clearly the presence of gas in the porous oil sands. A new type of imaging method, (namely, Amplitude Ratio for Partial Angle (ARPA) plots) was developed, which illustrated the magnitude of the reflected amplitude and the amplitude ratios, for various angles of incidence. The background shown in the ARPA plots are the the normal CMP seismic stack sections. Incorporating the thermomechanical seismic boundary conditions for interfaces separating porous media as described by De La Cruz and Spanos (1989), into the ARPA plots, is of future consideration. After interpreting the ARPA plots and having consulted the results obtained from the pre-stack depth migration algorithm and the zero offset modeling sections, we identified the lateral extents of the steam invaded zone.

The experimental data which have been provided by Esso Resources and used in this study was obtained to make use of existing seismic processing methods. In future field experiments it is recommended that modifications be made to exploit the advantages of the new algorithm developed here. This involves three dimensional field acquisition, the production of higher frequency sources, closer receiver spacing and recording over a wider range of angles of incidence ( $0^0$  to  $40^0$  or even  $60^0$ ). Although pre - steam seismic data was



not available in this test area, it should become a standard practice to serve as a base line of data against time dependent alterations during enhanced recovery operations.

In general one may state that seismic experimental methods when properly designed and when the data is carefully processed appear to show great promise in being used to determine the properties of other heterogeneous zones (molten areas, overpressured gas pockets) in the crust of the Earth. It is anticipated that algorithms and procedures developed and explored in this thesis will be used directly in fundamental studies on the properties of the crust as with LITHOPROBE data.

## BIBLIOGRAPHY

- Aki, K., and Richards P. G, 1980, Quantitative Seismology, Theory and methods, W. H Freeman and Co., San Fransisco.
- Alterman, Z. and Karal, F.C., 1968. Propagation of elastic waves in layered media by Finite Difference methods, Bulletin of the Seismological Society of America, 58, 367-398.
- Azimi, S. A., Kalinin, A V., and Pivovanov, B. L., 1968, Impulse and transient characteristics of media with linear and quadratic absorption laws, Phys. Solid Earth, 88-93.
- Bailey, N. J. L., Jobson, A. M., and Rogers, M. A., 1973, Bacterial degradation of crude oil: Comparison of field and experimental data: Chemical Geology, 11, 202 - 220.
- Bamford,D.,and Crampin,S.,1977. Seismic anisotropy:-the state of the art, Geophysical Journal of the Royal Astronomical Society ,49, 1-8.
- Bayliss, A., Jordan, K.E., LeMesurier, B.J. and Turkel, E., 1986. A fourth order accurate finite difference scheme for the computation of elastic waves, Bulletin of the Seismological Society of America, 76, 1115-1132.
- Berkhout, A. J.,1982, Seismic migration:Imaging of acoustic energy by wave field extrapolation. A. Theoretical aspects: Elsevier Science Publishers, N. Y.
- \_\_\_\_\_, 1984, Seismic migration:Imaging of acoustic energy by wave field: Elsevier Science Publishers, N.Y.
- \_\_\_\_\_, 1987, Applied seismic wave theory, Elsevier Science Publishers, N.Y.
- Biot, M. A., 1956, Theory of propagation of elastic waves in porous solid. I Low frequency range, J. Accoust. Soc. Am., 28, 168-178. II High frequency range, J. Acoust. Soc. Am., 28, 179-191.
- Booth, D.C., and Crampin, S.,1983a. The anisotropic reflectivity technique:theory, Geophysical Journal of the Royal Astronomical Society.,72,

755-766.

- , 1983b. The anisotropic reflectivity technique :anomalous arrivals from an anisotropic upper mantle, *Geophysical Journal of the Royal Astronomical Society*, 72, 767-782.
- Britton, M.W., William, L. M., Leibrecht, R. J., and Harmon, R. A., 1983, Street Ranch Pilot Test of Fractured - Assisted Steamflood Technology: *Journal of Petroleum Technology*, 35, 511 - 522.
- Carter, J.A., and Frazer, N.L., 1984, Accommodating lateral velocity changes in Kirchhoff migration by means of Fermat's principle, *Geophysics*, 49, 46 - 53.
- Cerveny, V., and Firbas, P., 1984. Numerical modelling and inversion of travel times of seismic body waves in inhomogeneous anisotropic media, *Geophysical Journal of the Royal Astronomical Society*, 76, 41-51.
- Cerveny, V., and Ravindra, R., 1970, *Theory of seismic head waves*, University of Toronto Press.
- Chang, W. F., and McMechan G. A., 1986, Reverse - time migration of offset vertical seismic profiling data using the excitation time imaging condition, *Geophysics*, 51, 67 - 84.
- Claerbout, J. F., 1970, Coarse grid calculations of waves in inhomogeneous media with application to delineation of complicated seismic structure, *Geophysics*, v. 35, pp. 407-418.
- , 1976, *Fundamentals of Geophysical data Processing*, McGraw Hill Inc.
- , 1985, *Imaging the Earth's Interior*, Blackwell Scientific Publications.
- Clark, V. A., Spencer, T. W., and Tittmann, B. R., 1981, The effect of thermal cycling on the seismic quality factor  $Q$  of sedimentary rocks, *J. Geophys. Res.*, 86, 7087-7094.
- Clayton and Engquist, 1980, Absorbing boundary conditions for acoustic and elastic wave equations, *Bull. Seism. Soc. Am.*, 67, 1529 - 1540.

- Crampin, S., 1977. A review of the effects of anisotropic layering on the propagation of surface waves, *Geophysical Journal of the Royal Astronomical Society*, 49, 9-27.
- \_\_\_\_\_, 1981. A review of wave motion in anisotropic and cracked elastic media, *Wave motion*, 3, 343-391.
- \_\_\_\_\_, 1984. An introduction to wave propagation in anisotropic media, *Geophysical Journal of the Royal Astronomical Society*, 76, 17-28
- Daley, P.F., and Hron, F., 1977. Reflection and transmission coefficients for transversely isotropic media, *Bulletin of the Seismological Society of America*, 67, 661-675.
- \_\_\_\_\_, 1979. SH waves in layered transversely isotropic media- An asymptotic expansion approach, *Bulletin of the Seismological Society of America*, 69, 689-711.
- Dankbaar, J. W. M., 1985, Separation of P and S waves, *Geophysical Prospecting*, 28, 676 - 689.
- De La Cruz, V., and Spanos. T. J. T., 1989, The reflection and transmission of seismic waves at the boundaries of porous media, *Journal of Geophys. Res.*, (in press).
- Devaney, A. and Oristaglio, M. C., 1986, A plane wave decomposition for elastic wave fields applied to the separation of P waves and S waves in vector seismic data, *Geophysics*, 51, 419 - 423.
- Domenico, S. N., 1976, Effect of brine-gas mixture on velocity in an unconsolidated sand reservoir, *Geophysics*, 41, 882 - 894.
- Dusseault, M. B., 1977, The geotechnical characteristics of the Athabasca oil sands, Ph.D. thesis, University of Alberta, Edmonton, Alberta.
- Energy Resources Conservation Board, 1979. The Cold Lake project, ERCB 79-E, C-2, Alberta.
- Farouq Ali, S. M., 1974, Current status of steam injection as a heavy oil recovery method, *Journal of Canadian Petroleum Technology*, 13, 54 -

68.

- \_\_\_\_\_, 1982, Elements of heavy oil recovery, University of Alberta press.
- Fawcette, J.A., and Clayton, R.W., 1984, Tomographic reconstruction of velocity anomalies, Bull. Seis. Soc. Am, 74, 2201 - 2219.
- Flock, D. L., and Lee, J., 1977, An experimental investigation of steam displacement of a medium gravity crude oil: The oil sands of Canada - Venezuela, CIM special volume, 17, 386 - 394.
- French, W. S., 1975, Computer migration of oblique seismic reflection profiles, Geophysics, v. 40, pp.961-980.
- Fryer, J.G., and Frazer, L.N., 1984. Seismic waves in stratified anisotropic media, Geophysical Journal of the Royal Astronomical Society, 78, 691-710.
- Futterman, W. I., 1962, Dispersive body waves, J. Geophys. Res., 67, 5279 - 5291.
- Gassman, F., 1961, Elastic waves through a packing of spheres, Geophysics, 16, 673-685.
- Gajewski, D., and Psencik, I., 1987. Computation of high frequency seismic wavefields in 3-D laterally inhomogeneous anisotropic media, Geophysical Journal of the Royal Astronomical Society, 91, 383 - 411.
- Gazdag, J., 1978, Wave equation migration with the phase shift method, Geophysics, v. 46, pp.1342-1351.
- Geertsma, J., 1961, Velocity-log interpretation. The effect of rock bulk compressibility, J. Soc. Petr. Eng., 1, 235-248.
- Gottlieb, D. and Turkel, E., 1976. Dissipative two-four methods for time dependent problems: Mathematical Computations, 30, 703-723.
- Grant, F. S. and West, G. F., 1965. Interpretation theory of Applied Geophysics, McGraw-Hill, New York.
- Greaves, R. J., and Fulp, J. T., 1987, Three dimensional seismic monitoring of an enhanced oil recovery process, Geophysics, 52, 1175

- 1187.

Hale, D., 1984, Dip-moveout by Fourier transform, *Geophysics*, v. 49, pp. 741-757

Harrison, D. B., Glaister, R. P., Nelson, H. W., 1979, Reservoir description of the Clearwater oil sand Cold Lake, Alberta, Canada, in: R.F Meyer; C. T. Steele (eds). *The future of heavy crude oil and tar sands*, 264 - 279.

Harris, M. C., and Sobkowicz, J. C., 1977, Engineering behavior of oil sand: The oil sands of Canada - Venezuela, *CIM special volume*, 17, 270 - 280.

Helbig, K., 1983. Elliptical Anisotropy its significance and meanings: *Geophysics*, 48, 825 - 832.

Hron, F., May, B. T., Covey, D.J. and Daley, P.F., 1986. Synthetic seismic sections for acoustic, elastic, anisotropic and vertically inhomogeneous layered media, *Geophysics*, 51, 710 - 735.

Ito, H., DeVilbiss, J., and Nur, A., 1979, Compressional and shear waves in saturated rock during water - steam transition, *Journal of Geophysical Research*, 84, 4731-4735.

Jain, S., and Wren, A. E., 1980, Migration before stack - Procedure and significance, *Geophysics*, 45, 204 - 212.

Johnston, R. L., 1982, *TEAPACK user's manual mathematical subroutines for numerical methods*, John Wiley & Sons, Inc.

Jones, T. D., 1986, Pore fluids and frequency dependent wave propagation, *Geophysics*, 51, 1939-1953.

Jones, T. D., and Nur, A., 1983, Velocity and attenuation in sandstone at elevated temperatures and pressures, *Geophys. Res. Lett.*, 10, 140-143.

Justice, J. H., Vassiliou, A. A., Singh, S., Logel, J. D., Hall, B. R., Hutt, P. R., Solanki, J. J., 1989, Acoustic tomography for monitoring enhanced oil recovery, *The Leading Edge*, 8, 12 - 19.

- Kelamis, P.G., and Kjartansson, E., 1985, Forward modeling in the Frequency space domain, *Geophys. Prosp.*, 32, 252 - 262.
- Kendall, G. H., 1977. Importance of reservoir in evaluating in situ recovery methods for Cold Lake Heavy oil part I, Reservoir Description, *Journal of Canadian Petroleum Geology*, 16, 41 - 47.
- Kennett, B.L.N., 1983. Seismic wave propagation in Stratified media, Cambridge University Press.
- Kjartansson, E., 1979, Constant Q wave propagation and attenuation, *J. Geophys. Res.* 84, 4737 - 4748.
- Kosloff, D., and Baysal, E., 1983, Migration with the full acoustic wave equation, *Geophysics*, 48, 677 - 687.
- Levin, F., K., 1980. Seismic velocities in transversely isotropic media 2: *Geophysics*, 45, 3 - 17.
- \_\_\_\_\_, 1978. The reflection refraction and diffraction of waves in media with elliptical velocity dependence: *Geophysics*, 43, 528 - 537.
- Loewenthal, D., Lu, L., Roberson, R., and Sherwood, J. W. C., 1976, The wave equation applied to migration, *Geophysical Prospecting*, 24, 380 - 399.
- Lomnitz, C., 1957, Linear dissipation in solids, *J. Appl. Phys.*, 28, 201 - 205.
- Love, A. E. H., 1927, *Mathematical theory of elasticity*, Cambridge, London.
- Macrides, C., 1987, Seismic tomography in Oil Sands for monitoring thermal recovery process, Ph.D. thesis, University of Alberta, Edmonton.
- Macrides, C., and Kanasewich, E. R., 1987, Seismic attenuation and Poisson's ratio in oil sands from crosshole measurements, *J. Can. Soc. of Expl. Geophys.*, 23, 46-55.
- Macrides, C., Kanasewich, E. R., and Bharatha, S., 1988, Multiborehole seismic imaging in steam injection heavy oil recovery projects, *Geophysics*, 53, 65-75.
- Majer, E. L., and McEvilly, T. V., 1979, *Seismological Investigations at*

- the Geysers geothermal field, *Geophysics*, 44, 246 - 249.
- Martynov, V., N. and Mikhailenko, B., G., 1984. Numerical modeling of propagation of elastic waves in anisotropic media for the half space and the sphere, *Geophysical Journal of the Royal Astronomical Society*, 76, 53 - 63.
- Marx, J. W. and Langenheim, R. H., 1959, Reservoir heating by hot fluid injection, *Trans. AIME*, 216, 312-315.
- Mavko, G, and Nur, A., 1979, Wave attenuation in partially saturated rocks, *Geophysics*, 44, 161-178.
- May, B., and Hron, F., 1978, Synthetic seismic sections of typical petroleum traps, *Geophysics*, 43, 1119 - 1147.
- Meissner, R. 1983, Attenuation of seismic waves in sediments: Proc. 11<sup>th</sup> World Petroleum Congress, 363 - 379.
- Mitchell, A.R., and Griffiths, D.F., 1980, The finite difference method in Partial Differential Equations, John Wiley & Sons.
- Mora, P.R., 1987, Nonlinear two-dimensional elastic inversion of multioffset seismic data, *Geophysics*, v. 52, pp.1211-1228.
- Muller, G, and Temme, P., 1987, Fast frequency - wavenumber migration for depth dependent velocity, *Geophysics*, 52, 1483 - 1491.
- Murphy, W. M., 1983, Effects of partial water saturation on attenuation in Massillon sandstone and Vycor porous glass, *J. Acoust. Soc. Am.*, 71, 1458 - 1468.
- Nyland, E., 1985, Seismic Attenuation in oil sands, *Aostran journal of research*, 2, 47 - 51.
- Nyland, E., and Dusseault, M.B., 1983, Fireflood microseismic monitoring; Results and potential for EOR process control, *Journal Canadian Petroleum Technology*, 22, 62 -68.
- Ostrander, W.,J., 1984. Plane wave reflection coefficients for gas sands at nonnormal angle of incidence, *Geophysics*, 49, 1637 - 1648.



- Outtrim, C. P., and Evans, R. G., 1977, Alberta's oil sands reserves and their evaluation: The oil sands of Canada - Venezuela, CIM special volume, 17, 36 - 66.
- O'Connell, R. J. and Budiansky, B., 1977, Viscoelastic properties of fluid saturated cracked solids, J. Geophys. Res., 82, 5719-5736.
- Petrashen, G., I., and Kashtan, B., M., 1984. Theory of body wave propagation in inhomogeneous anisotropic media, Geophysical Journal of the Royal Astronomical Society, 76, 29-39.
- Postma, G. W., 1955. Wave propagation in stratified medium: Geophysics, 20, 780 - 806.
- Pullin, N., Matthews, L., and Hirsche, K., 1987, Techniques applied to obtain very high resolution 3-D seismic imaging at an Athabasca tar sands thermal pilot, The Leading Edge, 6, 10 - 15
- Reshef, M., and Kosloff, D., 1986, Migration of common shot gathers, Geophysics, 51, 324 - 331.
- Schultz, P.S., and Sherwood, J.W.C., 1980, Depth migration before stack, Geophysics, 45, 376 - 393.
- Schneider, W. A., 1978, Integral formulation for migration in two and three dimensions, Geophysics, v. 43, pp. 49-76.
- Shah, P., M., 1973, Ray tracing in three dimensions, Geophysics 38, 600 - 604.
- Shepherd, D. W., 1979. Steam stimulation recovery of Cold Lake bitumen in :R.F. Meyer, C.T. Steele, (eds). The future of heavy crude oil and tar sands; 1979, 349 - 360.
- Spencer, J. W., 1981, Stress relaxations at low frequencies in fluid saturated rocks. Attenuation and modulus dispersion. J. Geophys. Res., 86, 1803-1812.
- Stewart, R. R., Huddleston, P. D., and Kan, T. K., 1984, Seismic versus sonic velocities: A vertical seismic profiling study, Geophysics, 49, 1153-1168.
- Stolt, R. H., 1978, Migration by Fourier transform, Geophysics, v. 43, 23-48.

- Stolt, R., and Benson, A.K., 1986, Seismic migration - theory and practise, Geophysical Press.
- Strang, G., 1968. On the construction and comparison of difference schemes: SIAM Journal of Numerical Analysis, 5, 506-517.
- Tarantola, A., 1986, A strategy for non-linear elastic inversion of seismic reflection data, Geophysics, v. 51, pp. 1893-1903.
- Temme, P., 1984, A comparison of common midpoint, single-shot and plane wave depth migration, Geophysics, 49, 1896 - 1907.
- Thomsen, L., 1986. Weak elastic anisotropy: Geophysics, 51, 1954-1966.
- , 1988. Reflection seismology over azimuthally anisotropic media, Geophysics, 53, 304-313.
- Tosaya, C. A., and Nur, A. M., DaPrat, G., 1984, Monitoring of thermal EOR fronts by seismic methods, Soc. Petr. Eng. Tech., paper SPE - 12744, 6pp.
- Turkel, E., 1974, Phase error and stability of second order methods for hyperbolic problems, J. Comp. Phys., 15, 226 - 250.
- Tsingas, C., and Kanasewich, E., R., 1989, Migration of common shot gathers in the omega-x domain, paper PRO-15, presented at the CSEG conference June 11 to 15, 1989.
- Tsingas, C., Vafidis, A., and Kanasewich, E. R., 1989, Elastic wave propagation in transversely isotropic media, submitted for publication.
- Vafidis, A., 1988. Supercomputer finite difference methods for seismic wave propagation, PhD dissertation University of Alberta, Edmonton.
- Virieux, J., 1984. SH-wave propagation in heterogeneous media: Velocity-stress finite-difference method: Geophysics, 49, 1933-1957.
- Virieux, J., 1986. P-SV wave propagation in heterogeneous media: Velocity-stress finite-difference method: Geophysics, 51, 889-901.
- Wang, Z, and Nur, A., 1986. Effect of temperature on wave velocities in sands and

sandstones with heavy hydrocarbons, Society of Petroleum Engineers,(SPE 15646).

\_\_\_\_\_, 1988, Effect of temperature on seismic wave velocities in rocks saturated with hydrocarbons: SPE Reservoir Engineering, 3, 158 - 164.

Wapenaar, C.P.A., Kinneging, N.A., and Berkhout, A.J.,1987, Principle of prestack migration based on the full elastic two-way wave equation, Geophysics, 52, 151 - 173.

Wayland, R. J., and Lee, D., 1986, Seismic mapping of EOR processes, The Leading Edge, 5, 36 - 40.

Wayland, R. J., and Leighton, A. T., 1985, Mapping technology: a key to EOR control,Oil and Gas Journal, 83, 48, 109 - 115.

Weglein, A. B.,1982, Multidimensional seismic analysis: Migration and Inversion, Geoexploration , v. 20, pp.47-60.

Wenzel, F., 1988, Approximate traveltimes in laterally inhomogeneous media, Geophysics, 53, 129 - 130.

White, J., E., 1982. Computed waveforms in transversely isotropic media, Geophysics, 47, 771 - 783.

White, J. E., and Sengbush, R. I., 1987, Production seismology, Volume 10, Geophysical Press Ltd.

Winkler, K. W., 1983, Frequency dependent ultrasonic properties of high - porosity sandstones, J. Geophys. Res., 88, 9439 - 9499.

\_\_\_\_\_, 1986, Estimates of velocity dispersion between seismic and ultrasonic frequencies, Geophysics, 51, 183-189.

Winkler, K. W., and Nur, A., 1982, Seismic attenuation: Effects of pore fluids and frictional sliding, Geophysics, 47, 1 - 15.

Winterstein, D., F., 1986. Anisotropy effects in P wave and SH wave stacking velocities

- contain information on lithology: *Geophysics*, 51, 661 - 672.
- Wright, J., 1987. The effects of transverse isotropy on reflection amplitude versus offset: *Geophysics*, 52, 564-567.
- Wuenchel, P. C., 1965, Dispersive body waves an experimental study, *Geophysics*, 30, 539 - 551.
- Yilmaz, O., and Claerbout, J. F., 1980, Prestack partial migration, *Geophysics*, 45, 1753 - 1779.
- Yilmaz, O., 1987, *Seismic data processing*, Society of Exploration Geophysicists, Tulsa, OK
- Young, G. B., and Braile, L. W., 1976, A computer program for the application of Zoeppritz's amplitude equation and Knott's energy equations, *Bull. Seismol. Soc. Am.*, 66, 1881 - 1885.

## Appendix A1

The MacCormack type scheme for the elastic P-SV wave equation in transversely isotropic media.

In the x-direction given by equations :

a) for  $n = 2k, k=0, 1, 2, \dots$

$$\dot{u}_{j,m}^{(1)} = \dot{u}_{j,m}^n - \frac{p}{6} \rho_{j,m}^{-1} (7 (\sigma_{xx})_{j,m}^n - 8 (\sigma_{xx})_{j+1,m}^n + (\sigma_{xx})_{j+2,m}^n)$$

$$\dot{u}_{j,m}^{n+1} = \frac{1}{2} (\dot{u}_{j,m}^{(1)} + \dot{u}_{j,m}^n) + \frac{p}{12} \rho_{j,m}^{-1} (7 (\sigma_{xx})_{j,m}^{(1)} - 8 (\sigma_{xx})_{j-1,m}^{(1)} + (\sigma_{xx})_{j-2,m}^{(1)})$$

$$\dot{w}_{j,m}^{(1)} = \dot{w}_{j,m}^n - \frac{p}{6} \rho_{j,m}^{-1} (7 (\sigma_{xz})_{j,m}^n - 8 (\sigma_{xz})_{j+1,m}^n + (\sigma_{xz})_{j+2,m}^n)$$

$$\dot{w}_{j,m}^{n+1} = \frac{1}{2} (\dot{w}_{j,m}^{(1)} + \dot{w}_{j,m}^n) + \frac{p}{12} \rho_{j,m}^{-1} (7 (\sigma_{xz})_{j,m}^{(1)} - 8 (\sigma_{xz})_{j-1,m}^{(1)} + (\sigma_{xz})_{j-2,m}^{(1)})$$

$$(\sigma_{xx})_{j,m}^{(1)} = (\sigma_{xx})_{j,m}^n - \frac{p}{6} (\lambda_{\parallel} + 2 \mu_{\parallel})_{j,m} (7 \dot{u}_{j,m}^n - 8 \dot{u}_{j+1,m}^n + \dot{u}_{j+2,m}^n)$$

$$(\sigma_{xx})_{j,m}^{n+1} = \frac{1}{2} ((\sigma_{xx})_{j,m}^{(1)} + (\sigma_{xx})_{j,m}^n) + \frac{p}{12} (\lambda_{\parallel} + 2 \mu_{\parallel})_{j,m} (7 \dot{u}_{j,m}^{(1)} - 8 \dot{u}_{j-1,m}^{(1)} + \dot{u}_{j-2,m}^{(1)})$$

$$(\sigma_{zz})_{j,m}^{(1)} = (\sigma_{zz})_{j,m}^n - \frac{p}{6} \lambda_{\perp,j,m} (7 \dot{u}_{j,m}^n - 8 \dot{u}_{j+1,m}^n + \dot{u}_{j+2,m}^n)$$

$$(\sigma_{zz})_{j,m}^{n+1} = \frac{1}{2} ((\sigma_{zz})_{j,m}^{(1)} + (\sigma_{zz})_{j,m}^n) + \frac{p}{12} \lambda_{\perp,j,m} (7 \dot{u}_{j,m}^{(1)} - 8 \dot{u}_{j-1,m}^{(1)} + \dot{u}_{j-2,m}^{(1)})$$

$$(\sigma_{xz})_{j,m}^{(1)} = (\sigma_{xz})_{j,m}^n - \frac{p}{6} \nu_{j,m} (7 \dot{w}_{j,m}^n - 8 \dot{w}_{j+1,m}^n + \dot{w}_{j+2,m}^n)$$

$$(\sigma_{xz})_{j,m}^{n+1} = \frac{1}{2} ((\sigma_{xz})_{j,m}^{(1)} + (\sigma_{xz})_{j,m}^n) + \frac{p}{12} v_{j,m} (7 \dot{w}_{j,m}^{(1)} - 8 \dot{w}_{j-1,m}^{(1)} + \dot{w}_{j-2,m}^{(1)})$$

b) for  $n = 2k+1, k=0, 1, 2, \dots$

$$\dot{u}_{j,m}^{(1)} = \dot{u}_{j,m}^n + \frac{p}{6} \rho_{j,m}^{-1} (7 (\sigma_{xx})_{j,m}^n - 8 (\sigma_{xx})_{j-1,m}^n + (\sigma_{xx})_{j-2,m}^n)$$

$$\dot{u}_{j,m}^{n+1} = \frac{1}{2} (\dot{u}_{j,m}^{(1)} + \dot{u}_{j,m}^n) - \frac{p}{12} \rho_{j,m}^{-1} (7 (\sigma_{xx})_{j,m}^{(1)} - 8 (\sigma_{xx})_{j+1,m}^{(1)} + (\sigma_{xx})_{j+2,m}^{(1)})$$

$$\dot{w}_{j,m}^{(1)} = \dot{w}_{j,m}^n + \frac{p}{6} \rho_{j,m}^{-1} (7 (\sigma_{xz})_{j,m}^n - 8 (\sigma_{xz})_{j-1,m}^n + (\sigma_{xz})_{j-2,m}^n)$$

$$\dot{w}_{j,m}^{n+1} = \frac{1}{2} (\dot{w}_{j,m}^{(1)} + \dot{w}_{j,m}^n) - \frac{p}{12} \rho_{j,m}^{-1} (7 (\sigma_{xz})_{j,m}^{(1)} - 8 (\sigma_{xz})_{j+1,m}^{(1)} + (\sigma_{xz})_{j+2,m}^{(1)})$$

$$(\sigma_{xx})_{j,m}^{(1)} = (\sigma_{xx})_{j,m}^n + \frac{p}{6} (\lambda_{\parallel} + 2\mu_{\parallel})_{j,m} (7\dot{u}_{j,m}^n - 8\dot{u}_{j-1,m}^n + \dot{u}_{j-2,m}^n)$$

$$(\sigma_{xx})_{j,m}^{n+1} = \frac{1}{2} ((\sigma_{xx})_{j,m}^{(1)} + (\sigma_{xx})_{j,m}^n) - \frac{p}{12} (\lambda_{\parallel} + 2\mu_{\parallel})_{j,m} (7\dot{u}_{j,m}^{(1)} - 8\dot{u}_{j+1,m}^{(1)} + \dot{u}_{j+2,m}^{(1)})$$

$$(\sigma_{zz})_{j,m}^{(1)} = (\sigma_{zz})_{j,m}^n + \frac{p}{6} \lambda_{\perp,j,m} (7\dot{u}_{j,m}^n - 8\dot{u}_{j-1,m}^n + \dot{u}_{j-2,m}^n)$$

$$(\sigma_{zz})_{j,m}^{n+1} = \frac{1}{2} ((\sigma_{zz})_{j,m}^{(1)} + (\sigma_{zz})_{j,m}^n) - \frac{p}{12} \lambda_{\perp,j,m} (7\dot{u}_{j,m}^{(1)} - 8\dot{u}_{j+1,m}^{(1)} + \dot{u}_{j+2,m}^{(1)})$$

$$(\sigma_{xz})_{j,m}^{(1)} = (\sigma_{xz})_{j,m}^n + \frac{p}{6} \nu_{j,m} (7\dot{w}_{j,m}^n - 8\dot{w}_{j-1,m}^n + \dot{w}_{j-2,m}^n)$$

$$(\sigma_{xz})_{j,m}^{n+1} = \frac{1}{2} ((\sigma_{xz})_{j,m}^{(1)} + (\sigma_{xz})_{j,m}^n) - \frac{p}{12} \nu_{j,m} (7\dot{w}_{j,m}^{(1)} - 8\dot{w}_{j+1,m}^{(1)} + \dot{w}_{j+2,m}^{(1)})$$

Similarly in the z-direction we get :

a) for  $n = 2k$ ,  $k=0, 1, 2, \dots$

$$\dot{u}_{j,m}^{(1)} = \dot{u}_{j,m}^n - \frac{p}{6} \rho_{j,m}^{-1} (7(\sigma_{xz})_{j,m}^n - 8(\sigma_{xz})_{j,m+1}^n + (\sigma_{xz})_{j,m+2}^n)$$

$$\dot{u}_{j,m}^{n+1} = \frac{1}{2} (\dot{u}_{j,m}^{(1)} + \dot{u}_{j,m}^n) + \frac{p}{12} \rho_{j,m}^{-1} (7(\sigma_{xz})_{j,m}^{(1)} - 8(\sigma_{xz})_{j,m-1}^{(1)} + (\sigma_{xz})_{j,m-2}^{(1)})$$

$$\dot{w}_{j,m}^{(1)} = \dot{w}_{j,m}^n - \frac{p}{6} \rho_{j,m}^{-1} (7(\sigma_{zz})_{j,m}^n - 8(\sigma_{zz})_{j,m+1}^n + (\sigma_{zz})_{j,m+2}^n)$$

$$\dot{w}_{j,m}^{n+1} = \frac{1}{2} (\dot{w}_{j,m}^{(1)} + \dot{w}_{j,m}^n) + \frac{p}{12} \rho_{j,m}^{-1} (7(\sigma_{zz})_{j,m}^{(1)} - 8(\sigma_{zz})_{j,m-1}^{(1)} + (\sigma_{zz})_{j,m-2}^{(1)})$$

$$(\sigma_{xx})_{j,m}^{(1)} = (\sigma_{xx})_{j,m}^n \frac{p}{6} \lambda_{\perp,j,m} (7 \dot{w}_{j,m}^n - 8 \dot{w}_{j,m+1}^n + \dot{w}_{j,m+2}^n)$$

$$(\sigma_{xx})_{j,m}^{(n+1)} = \frac{1}{2} ((\sigma_{xx})_{j,m}^{(1)} + (\sigma_{xx})_{j,m}^n) + \frac{p}{12} \lambda_{\perp,j,m} (7 \dot{w}_{j,m}^{(1)} - 8 \dot{w}_{j,m-1}^{(1)} + \dot{w}_{j,m-2}^{(1)})$$

$$(\sigma_{zz})_{j,m}^{(1)} = (\sigma_{zz})_{j,m}^n \frac{p}{6} (\lambda_{\perp} + 2\mu_{\perp})_{j,m} (7 \dot{w}_{j,m}^n - 8 \dot{w}_{j,m+1}^n + \dot{w}_{j,m+2}^n)$$

$$(\sigma_{zz})_{j,m}^{(n+1)} = \frac{1}{2} ((\sigma_{zz})_{j,m}^{(1)} + (\sigma_{zz})_{j,m}^n) + \frac{p}{12} (\lambda_{\perp} + 2\mu_{\perp})_{j,m} (7 \dot{w}_{j,m}^{(1)} - 8 \dot{w}_{j,m-1}^{(1)} + \dot{w}_{j,m-2}^{(1)})$$

$$(\sigma_{xz})_{j,m}^{(1)} = (\sigma_{xz})_{j,m}^n - \frac{p}{6} v_{j,m} (7 \dot{u}_{j,m}^n - 8 \dot{u}_{j,m+1}^n + \dot{u}_{j,m+2}^n)$$

$$(\sigma_{xz})_{j,m}^{n+1} = \frac{1}{2} ((\sigma_{xz})_{j,m}^{(1)} + (\sigma_{xz})_{j,m}^n) + \frac{p}{12} v_{j,m} (7 \dot{u}_{j,m}^{(1)} - 8 \dot{u}_{j,m-1}^{(1)} + \dot{u}_{j,m-2}^{(1)})$$

b) for  $n = 2k+1$ ,  $k=0, 1, 2, \dots$

$$\dot{u}_{j,m}^{(1)} = \dot{u}_{j,m}^n + \frac{p}{6} \rho_{j,m}^{-1} (7 (\sigma_{xz})_{j,m}^n - 8 (\sigma_{xz})_{j,m-1}^n + (\sigma_{xz})_{j,m-2}^n)$$

$$\dot{u}_{j,m}^{n+1} = \frac{1}{2} (\dot{u}_{j,m}^{(1)} + \dot{u}_{j,m}^n) - \frac{p}{12} \rho_{j,m}^{-1} (7 (\sigma_{xz})_{j,m}^{(1)} - 8 (\sigma_{xz})_{j,m+1}^{(1)} + (\sigma_{xz})_{j,m+2}^{(1)})$$

$$\dot{w}_{j,m}^{(1)} = \dot{w}_{j,m}^n + \frac{p}{6} \rho_{j,m}^{-1} (7 (\sigma_{zz})_{j,m}^n - 8 (\sigma_{zz})_{j,m-1}^n + (\sigma_{zz})_{j,m-2}^n)$$



$$\dot{w}_{j,m}^{n+1} = \frac{1}{2} (\dot{w}_{j,m}^{(1)} + \dot{w}_{j,m}^n) - \frac{p}{12} \rho_{j,m}^{-1} (7 (\sigma_{zz})_{j,m}^{(1)} - 8 (\sigma_{zz})_{j,m+1}^{(1)} + (\sigma_{zz})_{j,m+2}^{(1)})$$

$$(\sigma_{xx})_{j,m}^{(1)} = (\sigma_{xx})_{j,m}^n + \frac{p}{6} \lambda_{\perp,j,m} (7 \dot{w}_{j,m}^n - 8 \dot{w}_{j,m-1}^n + \dot{w}_{j,m-2}^n)$$

$$(\sigma_{xx})_{j,m}^{(n+1)} = \frac{1}{2} ((\sigma_{xx})_{j,m}^{(1)} + (\sigma_{xx})_{j,m}^n) - \frac{p}{12} \lambda_{\perp,j,m} (7 \dot{w}_{j,m}^{(1)} - 8 \dot{w}_{j,m+1}^{(1)} + \dot{w}_{j,m+2}^{(1)})$$

$$(\sigma_{zz})_{j,m}^{(1)} = (\sigma_{zz})_{j,m}^n + \frac{p}{6} (\lambda_{\perp} + 2\mu_{\perp})_{j,m} (7 \dot{w}_{j,m}^n - 8 \dot{w}_{j,m-1}^n + \dot{w}_{j,m-2}^n)$$

$$(\sigma_{zz})_{j,m}^{(n+1)} = \frac{1}{2} ((\sigma_{zz})_{j,m}^{(1)} + (\sigma_{zz})_{j,m}^n) - \frac{p}{12} (\lambda_{\perp} + 2\mu_{\perp})_{j,m} (7 \dot{w}_{j,m}^{(1)} - 8 \dot{w}_{j,m+1}^{(1)} + \dot{w}_{j,m+2}^{(1)})$$

$$(\sigma_{xz})_{j,m}^{(1)} = (\sigma_{xz})_{j,m}^n + \frac{p}{6} v_{j,m} (7 \dot{u}_{j,m}^n - 8 \dot{u}_{j,m-1}^n + \dot{u}_{j,m-2}^n)$$

$$(\sigma_{xz})_{j,m}^{n+1} = \frac{1}{2} ((\sigma_{xz})_{j,m}^{(1)} + (\sigma_{xz})_{j,m}^n) - \frac{p}{12} v_{j,m} (7 \dot{u}_{j,m}^{(1)} - 8 \dot{u}_{j,m+1}^{(1)} + \dot{u}_{j,m+2}^{(1)})$$

## Appendix A2

The MacCormack type scheme for SH wave propagation in elliptically anisotropic media:

In the x direction :

$$\dot{v}_{j,m}^{(1)} = \dot{v}_{j,m}^n - \frac{p}{6} \rho_{j,m}^{-1} (7 (\sigma_{xy})_{j,m}^n - 8 (\sigma_{xy})_{j+1,m}^n + (\sigma_{xy})_{j+2,m}^n)$$

$$\dot{v}_{j,m}^{n+1} = \frac{1}{2} (\dot{v}_{j,m}^{(1)} + \dot{v}_{j,m}^n) + \frac{p}{12} \rho_{j,m}^{-1} (7 (\sigma_{xy})_{j,m}^{(1)} - 8 (\sigma_{xy})_{j-1,m}^{(1)} + (\sigma_{xy})_{j-2,m}^{(1)})$$

$$(\sigma_{xy})_{j,m}^{(1)} = (\sigma_{xy})_{j,m}^n - \frac{p}{6} \mu_{j,m} (7 \dot{v}_{j,m}^n - 8 \dot{v}_{j+1,m}^n + \dot{v}_{j+2,m}^n)$$

$$(\sigma_{xy})_{j,m}^{n+1} = \frac{1}{2} ((\sigma_{xy})_{j,m}^{(1)} + (\sigma_{xy})_{j,m}^n) + \frac{p}{12} \mu_{j,m} (7 \dot{v}_{j,m}^{(1)} - 8 \dot{v}_{j-1,m}^{(1)} + \dot{v}_{j-2,m}^{(1)})$$

Those difference equations are employed in alternate time steps with the following ones

$$\dot{v}_{j,m}^{(1)} = \dot{v}_{j,m}^n + \frac{p}{6} \rho_{j,m}^{-1} (7 (\sigma_{xy})_{j,m}^n - 8 (\sigma_{xy})_{j-1,m}^n + (\sigma_{xy})_{j-2,m}^n)$$

$$\dot{v}_{j,m}^{n+1} = \frac{1}{2} (\dot{v}_{j,m}^{(1)} + \dot{v}_{j,m}^n) - \frac{p}{12} \rho_{j,m}^{-1} (7 (\sigma_{xy})_{j,m}^{(1)} - 8 (\sigma_{xy})_{j+1,m}^{(1)} + (\sigma_{xy})_{j+2,m}^{(1)})$$

$$(\sigma_{xy})_{j,m}^{(1)} = (\sigma_{xy})_{j,m}^n + \frac{p}{6} \mu_{j,m} (7 \dot{v}_{j,m}^n - 8 \dot{v}_{j-1,m}^n + \dot{v}_{j-2,m}^n)$$

$$(\sigma_{xy})_{j,m}^{n+1} = \frac{1}{2} ((\sigma_{xy})_{j,m}^{(1)} + (\sigma_{xy})_{j,m}^n) - \frac{p}{12} \mu_{j,m} (7 \dot{v}_{j,m}^{(1)} - 8 \dot{v}_{j+1,m}^{(1)} + \dot{v}_{j+2,m}^{(1)})$$

Similarly in the z-direction we get

$$\dot{\mathbf{v}}_{j,m}^{(1)} = \dot{\mathbf{v}}_{j,m}^n - \frac{p}{6} \rho_{j,m}^{-1} (7 (\sigma_{zy})_{j,m}^n - 8 (\sigma_{zy})_{j,m+1}^n + (\sigma_{zy})_{j,m+2}^n)$$

$$\dot{\mathbf{v}}_{j,m}^{n+1} = \frac{1}{2} (\dot{\mathbf{v}}_{j,m}^{(1)} + \dot{\mathbf{v}}_{j,m}^n) + \frac{p}{12} \rho_{j,m}^{-1} (7 (\sigma_{zy})_{j,m}^{(1)} - 8 (\sigma_{zy})_{j,m+1}^{(1)} + (\sigma_{zy})_{j,m+2}^{(1)})$$

$$(\sigma_{zy})_{j,m}^{(1)} = (\sigma_{zy})_{j,m}^n - \frac{p}{6} v_{j,m} (7 \dot{\mathbf{v}}_{j,m}^n - 8 \dot{\mathbf{v}}_{j,m+1}^n + \dot{\mathbf{v}}_{j,m+2}^n)$$

$$(\sigma_{zy})_{j,m}^{n+1} = \frac{1}{2} ((\sigma_{zy})_{j,m}^{(1)} + (\sigma_{zy})_{j,m}^n) + \frac{p}{12} v_{j,m} (7 \dot{\mathbf{v}}_{j,m}^{(1)} - 8 \dot{\mathbf{v}}_{j,m+1}^{(1)} + \dot{\mathbf{v}}_{j,m+2}^{(1)})$$

which are employed in alternate steps with,

$$\dot{\mathbf{v}}_{j,m}^{(1)} = \dot{\mathbf{v}}_{j,m}^n + \frac{p}{6} \rho_{j,m}^{-1} (7 (\sigma_{zy})_{j,m}^n - 8 (\sigma_{zy})_{j,m+1}^n + (\sigma_{zy})_{j,m+2}^n)$$

$$\dot{\mathbf{v}}_{j,m}^{n+1} = \frac{1}{2} (\dot{\mathbf{v}}_{j,m}^{(1)} + \dot{\mathbf{v}}_{j,m}^n) - \frac{p}{12} \rho_{j,m}^{-1} (7 (\sigma_{zy})_{j,m}^{(1)} - 8 (\sigma_{zy})_{j,m+1}^{(1)} + (\sigma_{zy})_{j,m+2}^{(1)})$$

$$(\sigma_{zy})_{j,m}^{(1)} = (\sigma_{zy})_{j,m}^n + \frac{p}{6} v_{j,m} (7 \dot{\mathbf{v}}_{j,m}^n - 8 \dot{\mathbf{v}}_{j,m+1}^n + \dot{\mathbf{v}}_{j,m+2}^n)$$

$$(\sigma_{zy})_{j,m}^{n+1} = \frac{1}{2} ((\sigma_{zy})_{j,m}^{(1)} + (\sigma_{zy})_{j,m}^n) - \frac{p}{12} v_{j,m} (7 \dot{\mathbf{v}}_{j,m}^{(1)} - 8 \dot{\mathbf{v}}_{j,m+1}^{(1)} + \dot{\mathbf{v}}_{j,m+2}^{(1)})$$

## APPENDIX B

### B1 The difference approximation

In order to compute the monochromatic wavefield at  $Q(x,z)$ , we discretize the differential equation (4.10), and approximate  $Q(x,z)$  by a mesh function  $q_n^m$  where  $m=i \Delta x$ , with  $i=1,\dots,N_x$  and  $n=k \Delta z$ , with  $k=1,\dots,N_z$ .

where  $\Delta x$  and  $\Delta z$  are the finite difference mesh grid spacings for the horizontal and vertical axes respectively.  $N_x$  indicates the number of traces in the gather and  $N_z$  the number of depth steps. For simplification we note that  $m(i \Delta x, k \Delta z) = m$ . Replacing the differentials with their respective finite differences the following:

$$-\frac{i}{2m} \delta_{xx} \delta_z Q - 2m i \delta_z Q + \delta_{xx} Q = 0 \quad (B1)$$

where  $\delta_z = \partial/\partial z$ ,  $\delta_{xx} = \partial^2 / \partial x^2$

A higher order (fourth) of accuracy for the approximation of the second order differential is the Douglas formula and is given by (Mitchell and Griffiths, 1980; Claerbout, 1985) :

$$\delta_{xx} = \frac{1}{\Delta x^2} \left( \frac{\delta^2}{1 + \gamma \delta^2} \right) \quad (B2)$$

where  $\Delta x$  is the grid spacing and  $\gamma = 1/12$  (Mitchell and Griffiths (1980) and  $\delta^2$  is the operator  $(1, -2, 1)$ .

An implicit Crank -Nicolson (Mitchell and Griffiths, 1980; Claerbout 1976,1985) finite difference algorithm scheme is employed to solve the resultant difference equation. This algorithm is unconditionally stable (Mitchell and Griffiths, 1980) and involves more than

one point at the advanced depth level centered at  $n+1/2$  according to :

$$q_{n+1/2}^m = \frac{1}{2} (q_{n+1}^m + q_n^m) \quad (\text{B3})$$

The finite difference approximation of the differential equation (B1) employing equations (B2) and (B3) reads:

$$\begin{aligned} & -\frac{i}{2 \Delta x^2 m} \left( \frac{\delta^2}{1 + \gamma \delta^2} \right) \left( \frac{q_{n+1}^m - q_n^m}{\Delta z} \right) + \frac{1}{2} \frac{\delta^2}{\Delta x^2 (1 + \gamma \delta^2)} q_{n+1}^m + \\ & + \frac{1}{2} \frac{\delta^2}{\Delta x^2 (1 + \gamma \delta^2)} q_n^m - \frac{2 m i}{\Delta z} (q_{n+1}^m - q_n^m) = 0 \end{aligned} \quad (\text{B4})$$

Multiply throughout by  $\Delta x^2 (1 + \gamma \delta^2)$  we have:

$$-\frac{i \delta^2}{2 m \Delta z} (q_{n+1}^m - q_n^m) + \frac{\delta^2}{2} (q_{n+1}^m + q_n^m) - \frac{2 m i \Delta x^2}{\Delta z} (1 + \gamma \delta^2) (q_{n+1}^m - q_n^m) = 0 \quad (\text{B5})$$

Simplifying by setting the laterally varying coefficients as A and B one has:

$$A(m,n) = \frac{i}{2 m \Delta z}$$

$$B(m,n) = \frac{2 m i \Delta x^2}{\Delta z}$$

and apply the operator  $\delta^2 = (1, -2, 1)$  we have:

$$\begin{aligned}
 & -A q_{n+1}^{m+1} + 2A q_{n+1}^m - A q_{n+1}^{m-1} + A q_n^{m+1} - 2A q_n^m + A q_n^{m-1} \\
 & + \frac{1}{2} q_{n+1}^{m+1} - q_{n+1}^m + \frac{1}{2} q_{n+1}^{m-1} + \frac{1}{2} q_n^{m+1} - q_n^m + \frac{1}{2} q_n^{m-1} \\
 & - B q_{n+1}^m + B q_n^m - B \gamma q_{n+1}^{m+1} + 2B \gamma q_{n+1}^m - B \gamma q_{n+1}^{m-1} \\
 & + B \gamma q_n^{m+1} - 2B \gamma q_n^m + B \gamma q_n^{m-1} = 0
 \end{aligned} \tag{B6}$$

Separate the terms with index  $n+1$  to the left hand side and the terms with index  $n$  to the right hand side and after some algebraic simplifications we have:

$$\begin{aligned}
 & (-A + \frac{1}{2} - B \gamma) q_{n+1}^{m+1} + (2A - 1 - B + 2B\gamma) q_{n+1}^m + \\
 & + (-A + \frac{1}{2} - B \gamma) q_{n+1}^{m-1} = \\
 & (-A - \frac{1}{2} - B \gamma) q_n^{m+1} + (2A + 1 - B + 2B\gamma) q_n^m + \\
 & + (-A - \frac{1}{2} - B \gamma) q_n^{m-1}
 \end{aligned}$$

(B7)

Replacing the coefficients of the q's and note that the first is equal to the third we get for the left hand side:

$$\overline{A}(m,n) = (-A + \frac{1}{2} - B\gamma)$$

$$\overline{B}(m,n) = (2A - 1 - B + 2B\gamma)$$

and for the right hand side:

$$\overline{C}(m,n) = (-A - \frac{1}{2} - B\gamma)$$

$$\overline{D}(m,n) = (2A + 1 - B + 2B\gamma)$$

or in compact form:

$$\overline{A}q_{n+1}^{m+1} + \overline{B}q_{n+1}^m - \overline{A}q_{n+1}^{m-1} = \overline{C}q_n^{m+1} + \overline{D}q_n^m + \overline{C}q_n^{m-1}$$

(B8)

Taking the n+1 values to be the unknown, while all the n present values are known, we end up with a system of simultaneous equations given as follows:

$$\begin{bmatrix} \text{bl} & \overline{A}_1 & 0 & . & . & 0 \\ \overline{A}_2 & \overline{B}_2 & \overline{A}_2 & . & . & 0 \\ 0 & \overline{A}_3 & \overline{B}_3 & \overline{A}_3 & . & 0 \\ . & . & . & . & . & 0 \\ 0 & . & . & \overline{A}_{m-1} & \overline{B}_{m-1} & \overline{A}_{m-1} \\ 0 & 0 & . & . & \overline{A}_m & \text{br} \end{bmatrix} \begin{bmatrix} q_{n+1}^1 \\ q_{n+1}^2 \\ . \\ . \\ q_{n+1}^{m-1} \\ q_{n+1}^m \end{bmatrix} = \begin{bmatrix} d_n^1 \\ d_n^2 \\ . \\ . \\ d_n^{m-1} \\ d_n^m \end{bmatrix}$$

(B9)

where

$$d_n^m = \overline{C}q_n^{m+1} + \overline{D}q_n^m + \overline{C}q_n^{m-1} \quad (B10)$$

The  $b_l$  and  $b_r$  are adjustable and are evaluated according to the boundary conditions. The above system is a triadiagonal system that is, except for three diagonals all the elements of the matrix in (B9) are zero. Claerbout, (1985), gives an elegant method for the solution of such systems. This method will be described in the following section.

## B2. Solving the Triadiagonal system of simultaneous equations.

Here we follow Claerbout (1985), to solve the system (B9). Let the simultaneous equations be written as a difference equation:

$$a_j q_{j+1} + b_j q_j + c_j q_{j-1} = d_j \quad (B11)$$

with  $j = 1, \dots, m$ , where  $m$  is the number of traces in the gather.

Introduce two new variables  $e_j$  and  $f_j$  along with an equation

$$q_j = e_j q_{j+1} + f_j \quad (B12)$$

which with shifted index can be written:

$$q_{j-1} = e_{j-1} q_j + f_{j-1} \quad (B13)$$

Insert (B13) to (B11) :

$$a_j q_{j+1} + b_j q_j + c_j (e_{j-1} q_j + f_{j-1}) = d_j \quad (B14)$$



Now rearrange (B14) to resemble (B12) :

$$q_j = \frac{-a_j}{b_j + c_j e_{j-1}} q_{j+1} + \frac{d_j - c_j f_{j-1}}{b_j + c_j e_{j-1}} \quad (\text{B15})$$

Compare (B15) with (B12) , we can see that recursion for  $e_j$  and  $f_j$  can be obtained as :

$$e_j = \frac{-a_j}{b_j + c_j e_{j-1}}$$

with  $e_1 = -a_1 / b_1$

and

$$f_j = \frac{d_j - c_j f_{j-1}}{b_j + c_j e_{j-1}}$$

with  $f_1 = d_1 / b_1$

For the right hand boundary we have from (B9) that:

$$A_{m-1} q_{m-1} + b_r q_m = d_m \quad (\text{B16})$$

and from (B13) replacing  $j$  by  $m$  we get:

$$q_{m-1} - e_{m-1} q_m = f_{m-1} \quad (\text{B17})$$

Solving the system of the two equations for  $q_m$  we have:

$$q_m = \frac{d_m - A_{m-1} f_{m-1}}{b_r + A_{m-1} e_{m-1}}$$

where  $b_l$  and  $b_r$  are evaluated using the 15 degree absorbing boundary condition, Clayton and Engquist, (1980).

Having  $e_j$  and  $f_j$  we can compute the rest of  $q_j$  's from equation (B13) going backwards.

### B3. Stability analysis for the 45 degrees paraxial approximation.

The problem of stability of a finite difference calculation used to solve equation (4.10) consists of finding a condition under which the difference:

$$q_n^m - \overline{q_n^m} = (Z_n^m)$$

between the theoretical and numerical solutions of the difference equation bounded as  $n$  tends to infinity, (Mitchell and Griffiths, 1980).

The von Neumann procedure consists of considering an harmonic decomposition of the error  $Z_n^m$  at grid points at a given depth level leading to error function

$$E(x) = \sum_j A_j e^{i b_j x}$$

where in general the frequencies  $|b_j|$  and  $j$  are arbitrary.

It is necessary to consider only the single term  $e^{ibx}$  where  $b$  is a any real number. For convenience, suppose that the depth being considered is  $z=0$ . To investigate the error propagation as  $z$  increases, it is necessary to find a solution of the finite difference equation (B1) which reduces to  $e^{ibx}$  where  $z=0$ . Let such a solution be:

$e^{az} e^{ibx}$ , where  $a = a(b)$  is complex in general. The original error component will not grow with increasing depth if  $|e^{ak}| \leq 1$  for all  $a$ .

Boundary conditions are neglected by the von Neumann method (Mitchell and Griffiths, 1980), which applies in theory only to pure initial value problems. It does however provide necessary conditions for stability of constant coefficient problems regardless of the type of boundary conditions.

Substitute

$$Z_n^m = e^{a n k} e^{i b m h}$$

where  $k = \Delta z$  and  $h = \Delta x$ , into the difference equation (B5) with  $A = -A$  and  $B = -B$  indicating downgoing waves and divide by  $e^{a n k} e^{i b m h}$ . We have:

$$\begin{aligned}
& A e^{a k} e^{i b h} - 2 A e^{a k} + A e^{a k} e^{-i b h} \\
& - A e^{i b h} + 2 A - A e^{-i b h} + \frac{1}{2} e^{a k} e^{i b h} - e^{a k} + \frac{1}{2} e^{a k} e^{-i b h} + \\
& + \frac{1}{2} e^{i b h} - 1 + \frac{1}{2} e^{-i b h} + B e^{a k} - B + B \gamma e^{a k} e^{i b h} - 2 B \gamma e^{a k} + B \gamma e^{a k} e^{-i b h} - \\
& - B \gamma e^{i b h} + 2 B \gamma + B \gamma e^{-i b h} = 0
\end{aligned}
\tag{B18}$$

Multiplying by  $e^{a k}$  throughout and recognizing that exponential terms can be expressed as cosines we have:

$$\begin{aligned}
& A e^{2 a k} (2 \cos(b h) - 2) - A e^{a k} (2 \cos(b h) - 2) + \frac{1}{2} e^{2 a k} (2 \cos(b h) - 2) + \frac{1}{2} e^{a k} (2 \cos(b h) - 2) \\
& + B e^{2 a k} - B e^{a k} + B \gamma e^{2 a k} (2 \cos(b h) - 2) - B \gamma e^{a k} (2 \cos(b h) - 2) = 0
\end{aligned}
\tag{B19}$$

Recognizing that  $(1 - \cos(t)) = 2 \sin^2(t/2)$  and simplifying by denoting  $\xi = e^{a k}$  and multiplying by -1 throughout we have:

$$\begin{aligned}
& 4 A \xi^2 \sin^2(b h / 2) - 4 A \xi \sin^2(b h / 2) + 2 \xi^2 \sin^2(b h / 2) + \\
& + 2 \xi \sin^2(b h / 2) - B \xi^2 + B \xi + 4 B \gamma \xi^2 \sin^2(b h / 2) - 4 B \gamma \xi \sin^2(b h / 2) = 0
\end{aligned}
\tag{B20}$$

Factoring out  $\xi^2$  and  $\xi$  we get a second order polynomial equation in  $\xi$  as:

$$\begin{aligned}
& \xi^2 (4 A \sin^2(b h / 2) + 2 \sin^2(b h / 2) - B + 4 B \gamma \sin^2(b h / 2)) \\
& + \xi (-4 A \sin^2(b h / 2) + 2 \sin^2(b h / 2) + B - 4 B \gamma \sin^2(b h / 2)) = 0
\end{aligned}
\tag{B21}$$

setting  $S = 2 \sin^2(b h / 2)$ ,  $C = 4 A \sin^2(b h / 2) - B + 4 B \gamma \sin^2(b h / 2)$  and recognizing that the coefficients of  $\xi^2$  and  $\xi$  are the same except the  $-S$  and  $+S$  terms we get a simplified equation:

$$\xi^2 (C + S) - \xi (C - S) = 0$$

Solving for  $\xi$  we get the two solutions  $\xi_1 = 0$  and  $\xi_2 = (C - S) / (C + S)$

Since  $C$  is a pure imaginary number the amplification factor -  $\xi$  then takes the form of a complex number divided by its complex conjugate. Expressing the complex number in polar form it becomes clear that such a number has a magnitude of unity. Hence,  $|\xi| = 1$  and this satisfies the unconditional stability criterion, namely  $|\xi| \leq 1$ .

#### B4. Absorbing Boundary conditions

The so called 15<sup>0</sup> paraxial absorbing boundary conditions were employed in the solution of the equation (4.10), (Clayton and Enquist, 1980). The effectiveness of the absorbing boundary conditions given here can be shown by comparing their effective reflection coefficient at the boundaries. The two dimensional scalar wave equation is given as:

$$P_{xx} + P_{zz} = \frac{1}{v^2} P_{tt} \quad (B22)$$

Taking the 15<sup>0</sup> paraxial approximation we have:

$$P_x + \frac{1}{v} P_t = 0 \quad (B23)$$

Consider an incident (upcoming) plane wave travelling at the  $-z$ ,  $+x$ , direction according to  $P_I = \exp(ik_x x - ik_z z - i\omega t)$  which initiates a reflection from the right boundary of the form  $P_R = r \exp(-ik_x x - ik_z z - i\omega t)$ , where  $r$  is the effective reflection coefficient. Locally near

the boundary the wave field ( $P_I + P_R$ ) will satisfy the boundary condition. Applying the boundary condition given above we obtain:

$$ik_x - i r k_x - i \frac{\omega}{v} - i r \frac{\omega}{v} = 0$$

or

$$r = \frac{k_x - \omega/v}{k_x + \omega/v}$$

(B24)

recognizing that  $k_x = k \sin(\theta)$  where  $k = \omega/v$  and  $\theta$  is the angle between the travelling wave and the vertical side boundary we have:

$$r = - \frac{1 - \sin(\theta)}{1 + \sin(\theta)}$$

(B25)

Thus when the wave hits the boundary with  $\theta = 0^0$  (i.e travelling in the vertical direction) then  $r = -1$ . The absorbing boundary conditions in this case are matched to the exact paraxial wave equation. On the contrary, when the wave hits the side boundary within incident angles greater than  $0^0$  then one can see that the effective reflection coefficient gets smaller.

### APPENDIX C

#### Dispersion analysis for the 45 degrees parabolic wave equation and its finite difference approximation

To find the effect of the 45 degrees parabolic wave approximation, we shall consider the case of a plane wave propagating in a homogeneous medium for which  $\omega/v(x,z) = k$ .

Then since  $P(x,z) = \exp(ik_x x + i k_z z)$  represents a downgoing plane wave, the time shifted monochromatic wavefield  $Q(x,z)$  will be equal to:

$$Q(x,z) = \exp(-ik_x x + (k_z - k) z) \quad (C1)$$

Put (C1) into the equation (B1) after calculating the following derivatives and write

$$\exp(A) = \exp i (k_x x + (k_z - k) z) \text{ and ,}$$

$$\delta_z Q = i(k_z - k) \exp(A)$$

$$\delta_{zzx} Q = -i k_x^2 (k_z - k) \exp(A)$$

$$\delta_{xx} Q = -k_x^2 \exp(A)$$

We have recognizing that  $m=k$ , that:

$$2 i^2 k (k_z - k) + \frac{i^2}{2 k} [-k_x^2 (k_z - k)] - k_x^2 = 0$$

or

$$-4k^2(k_z - k) + k_x^2(k_z - k) - 2k_x^2 k = 0$$

and thus:

$$k_z = \frac{3k_x^2 k - 4 k^3}{k_x^2 - 4 k^2}$$

(C2)

To normalize we divide by  $k$  giving:

$$\frac{k_z}{k} = \frac{3k_x^2 - 4k^2}{k_x^2 - 4k^2}$$

(C3)

where  $\lambda$  is a dominant wavelength, and  $k = 2\pi/\lambda$  and  $k_x = k \sin\theta$ , where  $\theta$  is the angle of wavefront propagation measured from the vertical axis.

To compute the dispersion relation for the finite difference approximation one has to substitute:

$$q_m^n = \exp i (k_x m \Delta x + (k_z - k) n \Delta z)$$

into the difference equation given by (B5).

Doing so one gets:

$$\begin{aligned} & -A \exp i (k_x(m+1)\Delta x + (k_z - k) (n+1) \Delta z) \\ & + 2A \exp i (k_x m \Delta x + (k_z - k) (n+1) \Delta z) \\ & - A \exp i (k_x(m-1) \Delta x + (k_z - k) (n+1) \Delta z) \\ & + A \exp i (k_x(m+1) \Delta x + (k_z - k) n \Delta z) \\ & - 2A \exp i (k_x(m) \Delta x + (k_z - k) n \Delta z) \\ & + A \exp i (k_x(m-1) \Delta x + (k_z - k) n \Delta z) \\ & + \frac{1}{2} \exp i (k_x(m+1) \Delta x + (k_z - k)(n+1) \Delta z) \\ & - \exp i (k_x(m) \Delta x + (k_z - k)(n+1) \Delta z) \\ & + \frac{1}{2} \exp i (k_x(m-1) \Delta x + (k_z - k)(n+1) \Delta z) \\ & + \frac{1}{2} \exp i (k_x(m+1) \Delta x + (k_z - k)(n) \Delta z) \\ & - \exp i (k_x(m) \Delta x + (k_z - k)(n) \Delta z) \\ & + \frac{1}{2} \exp i (k_x(m-1) \Delta x + (k_z - k)(n) \Delta z) \end{aligned}$$

$$\begin{aligned}
& - B \exp i (k_x(m) \Delta x + (k_z-k)(n+1) \Delta z) \\
& + B \exp i (k_x(m) \Delta x + (k_z-k)(n) \Delta z) \\
& - B\gamma \exp i (k_x(m+1) \Delta x + (k_z-k)(n+1) \Delta z) \\
& + 2B\gamma \exp i (k_x(m) \Delta x + (k_z-k)(n+1) \Delta z) \\
& - B\gamma \exp i (k_x(m-1) \Delta x + (k_z-k)(n+1) \Delta z) \\
& + B\gamma \exp i (k_x(m+1) \Delta x + (k_z-k)(n) \Delta z) - 2 B\gamma \exp i (k_x(m) \Delta x + (k_z-k)(n) \Delta z) \\
& + B\gamma \exp i (k_x(m-1) \Delta x + (k_z-k)(n) \Delta z) = 0
\end{aligned}$$

(C4)

Divide (C4) by  $\exp i (k_x m \Delta x + (k_z - k) n \Delta z)$  and using the following trigonometric identities

$$\cos(k_x \Delta x) = \frac{e^{ik_x \Delta x} + e^{-ik_x \Delta x}}{2}$$

and

$$\cos((k_z - k) \Delta x) = \frac{e^{i(k_z - k) \Delta x} + e^{-i(k_z - k) \Delta x}}{2}$$

and that

$$2 \sin^2(k \Delta x / 2) = (1 - \cos(k \Delta x))$$

we get the following:

$$\begin{aligned}
& 4 A \sin^2(k_x \Delta x / 2) e^{i(k_z - k) \Delta z} - 4 A \sin^2(k_x \Delta x / 2) - \\
& - 2 \sin^2(k_x \Delta x / 2) e^{i(k_z - k) \Delta z} - 2 \sin^2(k_x \Delta x / 2) - \\
& - B e^{i(k_z - k) \Delta z} + B + 4 B \gamma \sin^2(k_x \Delta x / 2) e^{i(k_z - k) \Delta z} - \\
& - 4 B \gamma \sin^2(k_x \Delta x / 2) = 0
\end{aligned}$$

(C5)

or



$$\begin{aligned}
& A(e^{i(k_z-k)\Delta z} - 1) * 4 \sin^2(k_x \Delta x / 2) - (e^{i(k_z-k)\Delta z} + 1) * 2 \sin^2(k_x \Delta x / 2) - \\
& - B(e^{i(k_z-k)\Delta z} - 1) + 4 B \gamma (e^{i(k_z-k)\Delta z} - 1) * \sin^2(k_x \Delta x / 2) = 0
\end{aligned}
\tag{C6}$$

Substitute in (C6) the expressions for  $A = i/(2 k \Delta z)$  and  $B = 2 k i \Delta x^2 / \Delta z$  we have:

$$\begin{aligned}
& i \frac{(e^{i(k_z-k)\Delta z} - 1)}{(e^{i(k_z-k)\Delta z} + 1)} = \frac{-2 \sin^2(k_x \Delta x / 2)}{\left[ \frac{1}{k \Delta z} + \frac{4 k \gamma \Delta x^2}{\Delta z} \right] * 2 \sin^2(k_x \Delta x / 2) - \frac{2 k \Delta x^2}{\Delta z}}
\end{aligned}
\tag{C7}$$

recognizing that

$$\tan(x/2) = -i \frac{e^{ix} - 1}{e^{ix} + 1}$$

we have :

$$\begin{aligned}
& \tan\left[\frac{(k_z-k)\Delta z}{2}\right] = \frac{2 \sin^2(k_x \Delta x / 2)}{\left[ \frac{1}{k \Delta z} + \frac{4 k \gamma \Delta x^2}{\Delta z} \right] * 2 \sin^2(k_x \Delta x / 2) - \frac{2 k \Delta x^2}{\Delta z}}
\end{aligned}
\tag{C8}$$

or

$$\begin{aligned}
& \frac{k_z}{k} = 1 + \frac{2}{k \Delta z} \tan^{-1} \left( \frac{2 \sin^2(k_x \Delta x / 2)}{\left[ \frac{1}{k \Delta z} + \frac{4 k \gamma \Delta x^2}{\Delta z} \right] * 2 \sin^2(k_x \Delta x / 2) - \frac{2 k \Delta x^2}{\Delta z}} \right)
\end{aligned}
\tag{C9}$$

## APPENDIX D

Cerveny and Ravindra (1971), showed that for two dimensional inhomogeneous media the system of ordinary first order differential equations for rays is given by:

$$dx(t)/dt = v(x,z) * \cos(e_x)$$

$$dz(t)/dt = v(x,z) * \sin(e_x)$$

$$\partial e_x / \partial t = \partial v(x,z) / \partial x * \sin(e_x) - \partial v(x,z) / \partial z * \cos(e_x)$$

(C. 1)

where x and z are the Cartesian coordinates of the ray, v(x,z) is the compressional velocity of the medium and  $e_x$  is the angle between the ray path and the horizontal coordinate.

A fourth order Runge - Kutta extrapolation method (Johnston,1982), was employed to solve numerically the above system of equations.

## Appendix E

### Formation heating by steam injection.

When steam at a given temperature,  $T_S$ , is injected into an oil bearing formation at temperature  $T_R$ , it displaces a certain fraction of the in-place oil while condensing and heating the rock and fluids simultaneously. The condensate formed preheats the rock further ahead. Under idealized conditions (no gravity segregation of steam, uniform thickness and no pressure drop, i.e., temperature drop in the steam invaded zone), it could be postulated that the heated zone is at constant temperature,  $T_S$ , extending from the injection end to a point where the temperature abruptly drops from  $T_S$  to  $T_R$ . Marx and Langenheim, (1959), first postulated such a picture for steam injection. The M-L treatment implies that the condensate transfers the heat over an infinitesimal distance constituting the *condensation front*. The result is a step function temperature profile in which  $T_S$  drops to  $T_R$ . Under the assumptions described above, a heat balance at any time  $t$  gives:

$$Q_i = Q_{ob} + Q_s$$

(E1)

i.e. Heat injection rate = Heat loss rate to overburden and underburden + Heating rate of the rock and fluids to  $T_S$ .

This heat balance equation results in a differential equation and the solution of this equation gives the steam zone volume  $V_S$  as:

$$V_s = \frac{Q_i M_s h_i^2 F_1}{4 k_{hob} M_{ob} (T_S - T_R)}$$

(E2)

$Q_i$  is the heat injection rate given by:

$$Q_i = (350/24) i_{st} [(h_w - h_R) + f_{st} L_V] \quad (E3)$$

where,

$i_{st}$  is the steam injection rate,

$f_{st}$  is the steam quality, ( 1 for pure steam)

$h_w$  is the enthalpy of the saturated water,

$h_R$  is the enthalpy of the water at reservoir conditions and

$L_V$  is the latent heat of the steam

$M_s$  is the volumetric heat capacity of the Formation (Clearwater),

$h_t$  is the thickness of the Formation,

$k_{hob}$  is the thermal conductivity of the overburden and

$F_1$  is the so called M-L function given by:

$$F_1 = \exp(-n) \operatorname{erfc}(t_D)^{1/2} + 2\left(\frac{t_D}{\pi}\right)^{1/2} - 1$$

and  $\operatorname{erfc}$  denotes the complementary error function (1- erf) and the dimensionless  $t_D$  is proportional to the injection time  $t$  as:

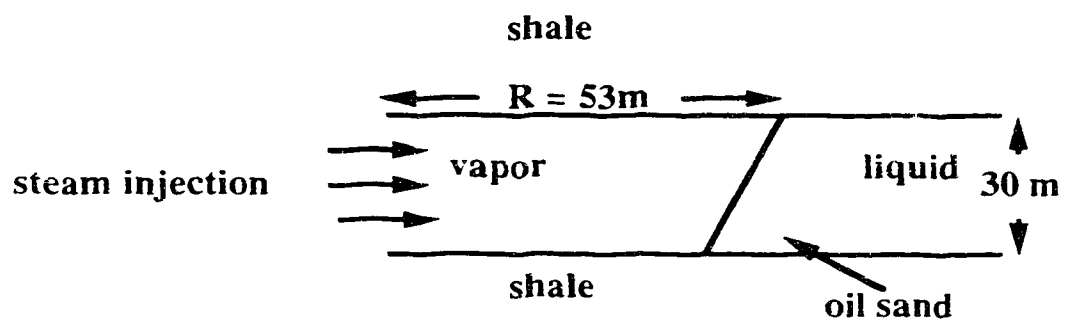
$$t_D = \frac{4 k_{hob} M_{ob} t}{h_t^2 M_s^2} \quad (E4)$$

Steam of quality  $f_{st} = 70\%$ , is injected at a pressure of 10 MPa into the Clearwater Formation. From steam tables (Farouq Ali, 1982) we find that the corresponding temperature is  $310^\circ\text{C}$  and also the corresponding values for  $h_w$ ,  $h_R$  and  $L_V$ . From equation (E3) we find that  $Q_i$  is equal to 18,747,368 BTU/hr. The volumetric heat capacity

of the Clearwater is  $2500 \text{ KJ}/(\text{m}^3 \text{ } ^\circ\text{K})$ . The thickness of the reservoir at the location of the experiment is around 30m. The thermal conductivity is  $2.1 \text{ W}/(\text{m } ^\circ\text{K})$  and the heat capacity of the overburden is  $2650 \text{ KJ}/(\text{m}^3 \text{ } ^\circ\text{K})$ . Reservoir temperature is  $12 \text{ } ^\circ\text{C}$ . Substituting all the above values into equation (E4) and for a steam injection period of three years, we find  $t_D$  to be equal to 0.360. From tabular values we find that  $F_1$  is equal to 0.325. Then substituting in equation (E2) and incorporating equation (E3) we find that the steam zone volume is equal to  $256,860 \text{ m}^3$ . Assuming a cylindrical steam zone with a thickness of 30m and solving for the radius, we find that  $R=53\text{m}$ . Thus the diameter will be 106m.

For a steam injection period of five years performing the same analysis as above we estimate a steam zone radius of approximately 90m, and thus a diameter of 180m. Figure E. 1, illustrates the estimated steam zones for three and five years of steam injection periods.

For 3 years



For 5 years

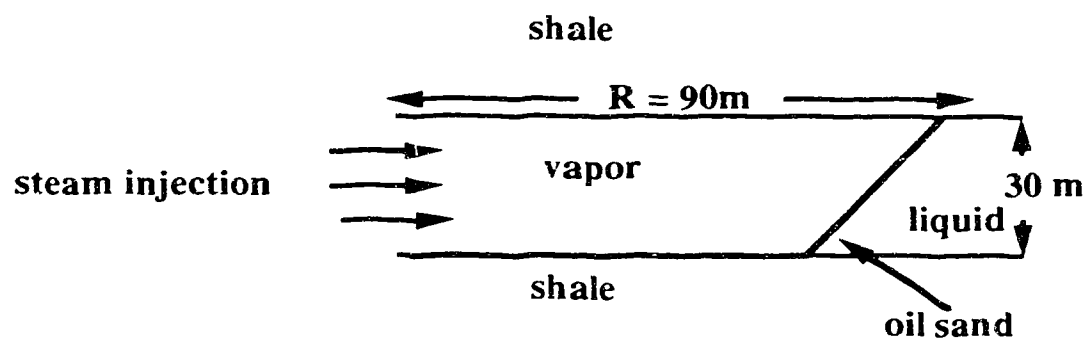


Figure E.1. Steam zone growth for the three and five years of steam injection periods.